Astronomy Reports, Vol. 44, No. 4, 2000, pp. 209–218. Translated from Astronomicheskiĭ Zhurnal, Vol. 77, No. 4, 2000, pp. 243–253.

A Model for the Spectrum of Sakurai's Object (V4334 Sgr)

Ya. V. Pavlenko and L. A. Yakovina

Main Astronomical Observatory, Goloseevo, Kiev-127, 03680 Ukraine

Received April 12, 1999

Abstract—Theoretical spectral energy distributions for Sakurai's object at 300–1000 nm are derived. A model-atmosphere grid with T_{eff} = 5000–6250 K and $\log g$ = 0.0–1.0 is computed for the chemical composition of Sakurai's object using opacity sampling including molecular and atomic absorption. Opacity due to absorption in 20 band systems of diatomic molecules is computed using the JOLA technique. The theoretical fluxes are compared with the observed energy distribution in a spectrum of Sakurai's object taken in April 1997. It is shown that (a) the theoretical energy distributions agree well qualitatively with the observed spectrum and depend strongly on the effective temperature; (b) C_2 and CN molecular bands are dominant in the visible and near-infrared spectrum, while atomic absorption is important at UV and blue wavelengths; and (c) comparison of the observed and computed spectra yields an effective temperature for Sakurai's object in April 1997 $T_{eff} \approx$ 5250–5500 K. The dependence of the computed spectra at 300–1000 nm on the input parameters and adopted approximations is also discussed. © *2000 MAIK "Nauka/Interperiodica".*

1. INTRODUCTION

Sakurai's object (V4334 Sgr) was discovered on February 20, 1996, and is the central star ($\approx 11^m$) of a low-surface-brightness planetary nebula [1]. The kinematic age of the planetary nebula is estimated to be 4600 years [2]. Subsequent studies showed that the brightness of Sakurai's object increased in 1995–1997 [3]. The corresponding outburst probably began in late 1994. The position of Sakurai's object coincides with a 21st magnitude star on a *J* plate taken in 1976 [4].

Multicolor photometry shows that, until recently, the short-wavelength (*U* and *B*) flux of this object declined continuously, while its *R* and *I* brightness increased [3]. This has been interpreted as the effect of continuous (slightly accelerated) radial photospheric expansion with a velocity of about 1 km/s [5]. The star cooled by more than 2000 K over two years, and its bolometric luminosity increased from $-4^m.20$ to $-5^m.33$ from March 1996 to October 1997 [3]. By June 1997, an optically thick dust shell condensed around the star at a distance of $\approx 80\ R_*$ [3].

The character of the observed processes provides evidence that Sakurai's object is in the final stage of helium-layer burning in the nucleus of the planetary nebula [4], as predicted theoretically [6]. This object has been the target of extensive photometric [4, 5, 7] and spectroscopic [8, 9] observations in recent years. Its spectra are very difficult to classify due to the peculiar chemical composition of the star. Its atmosphere is clearly hydrogen-deficient, carbon-rich, and enriched in light s-process elements [8–11]; i.e., the chemical composition of Sakurai's object resembles that of R CrB stars [8]. Since the spring of 1997, it has been classified as a carbon star [3, 5]. Unfortunately, progress in these studies has been limited by the incompleteness of our knowledge of the physical processes occurring in the atmosphere of this object.

We thus face the task of modeling the spectral energy distribution of Sakurai's object. The problem is that we must compute model atmospheres with anomalous (nonsolar) chemical compositions, as well as synthetic spectra over a wide wavelength interval, including the effect of atomic absorption lines and molecular bands. The results thus depend on a large number of physical parameters that are not accurately known. On the other hand, such computations can be used to refine estimates of the atmospheric parameters of Sakurai's object.

We used a spectrum at 300–1000 nm taken on April 29, 1997, after correction for interstellar reddening $E(B - V)$ = 0.54 [4]. The spectroscopic data were kindly provided by Dr. Hilmar Duerbeck.

2. COMPUTATION METHOD

We performed our numerical computations using classical approximations: LTE in a plane-parallel geometry, with only radiative and convective energy transport. We used the chemical composition[1] inferred by Asplund *et al.* [8] using the synthetic spectrum method (see Table 1). To analyze the dependence of the spectral energy distribution on chemical composition, we varied the abundances of some elements (see Section 3.4).

[1] We use an abundance scale where $\sum N_i = 1$.

1063-7729/00/4404-0209$20.00

Table 1. Chemical composition of the atmosphere of Sakurai's object adopted here

Z	Element	$\log N$ ($\Sigma N_i = 1$)	$\log N$ ($\log\Sigma(N_i\ \mu_i) = 12.15$) [8]	$\log N_\odot$ ($\Sigma N_i = 1$)
1	H	–1.727	9.7	–0.04
2	He	–0.027	11.4	–1.05
3	Li	–7.827	3.6	–10.88
6	C	–1.727	9.7	–3.48
7	N	–2.527	8.9	–3.99
8	O	–1.927	9.5	–3.11
10	Ne	–2.127	9.3	–3.95
11	Na	–4.727	6.7	–5.71
12	Mg	–4.827	6.6	–4.46
13	Al	–4.827	6.6	–5.57
14	Si	–4.327	7.1	–4.49
16	S	–4.827	6.6	–4.83
19	K	–6.627	4.8	–6.92
20	Ca	–5.827	5.6	–5.68
21	Sc	–8.327	3.1	–8.94
22	Ti	–7.327	4.1	–7.05
24	Cr	–6.927	4.5	–6.37
26	Fe	–5.127	6.3	–4.37
28	Ni	–5.327	6.1	–5.79
29	Cu	–6.527	4.9	–7.83
30	Zn	–6.727	4.7	–7.44
37	Rb	–7.727	3.7	–9.44
38	Sr	–6.527	4.9	–9.14
39	Y	–8.127	3.3	–9.80
40	Zr	–8.427	3.0	–9.44
56	Ba	–9.927	1.5	–9.91
57	La	–9.827	1.6	–10.82

We solved the ionization–dissociation equilibrium equations for 70 species including atoms, ions, and molecules. We adopted the chemical equilibrium constants from [12] and reduced them to the form suggested in [13]. Our ionization–dissociation equilibrium computations had certain specific features due to the low atmospheric hydrogen abundance of Sakurai's object and the relatively high temperatures (5000–7000 K) involved.

We computed the opacities at the frequencies of 20 diatomic-molecule band systems using the JOLA (just overlapping approximation) technique. In this approximation, the profiles of molecular bands are computed without taking into account their rotational profiles. This simplifying assumption makes it possible to substantially reduce the computation time and sidestep problems connected with the use of lists of rotational molecular lines. To compute the molecular opacities in this approximation, we used a modified version of the BIGF1 subroutine developed by A. Yaremchuk. See [14] for a description of the computational formulas used in the code. We adopted the data for the molecular terms, Franck–Condon factors, and oscillator strengths f_e of the electron systems of the spectral bands from [15], [16], and [17], respectively.

Our computations are based on the important simplifying assumption that all carbon is in the form of ^{12}C. At the same time, Asplund *et al.* [8] showed that the isotopic ratio in the atmosphere of Sakurai's object is $^{12}C/^{13}C = 5$, i.e., close to the equilibrium value (~2.5). We defer computations of model atmospheres and spectra for Sakurai's object with different $^{12}C/^{13}C$ ratios to subsequent papers.

2.1. Model Atmospheres for Sakurai's Object

We computed our model atmospheres using the SAM941 code [18], which is a modified version of the ATLAS9 code [19] designed for use in computing model atmospheres with anomalous chemical compo-

sitions. We used the opacity sampling technique suggested by Sneden *et al.* [20] to allow for blanketing due to atomic and ion absorption lines. Opacity sampling is based on the use of opacities at randomly sampled frequencies and requires more computations than, e.g., the opacity distribution function method implemented in the ATLAS9 code. However, opacity sampling is free of the most important drawback of the opacity distribution function method, in which opacity parameters such as the lists and relative intensities of spectral lines do not vary with depth in the stellar atmosphere (see [21] for a detailed discussion). This problem is especially relevant for the atmosphere of Sakurai's object, where the opacity is mostly due to free–free CI transitions and absorption by carbon-containing molecules in deep and outer layers, respectively.

We adopted the atomic and ion absorption line lists from the VALD database [22]. We used the data of Hoffsaess [23] to compute the opacity due to free–free absorption by neutral carbon and oxygen atoms. As noted above, we computed the molecular opacity using the JOLA technique, taking into account the 20 band systems of diatomic molecules listed in Table 2. Since carbon is the second most abundant element (after helium) in Sakurai's object [8], the opacity at low temperatures is due primarily to band systems of the molecules C_2 and CN.

We derived the relations $\tau_{ross} = f(T, P_g, \mu)$ (here μ is metallicity), which we then used in temperature corrections in the computed model atmospheres (see also [18]). Note that we computed our model atmospheres based on a detailed chemical composition of Sakurai's object, i.e., using a self-consistent approach, which is essential due to the peculiar chemical composition and set of opacity sources in the atmosphere of this object.

We computed the convective energy transport using a mixing-length technique. We assumed $l/H = 1.6$ and did not take into account convective overshooting. However, this last effect is not important for the model atmospheres of hydrogen-deficient stars [18].

We computed a grid of model atmospheres with T_{eff} = 5000–6250 K and $\log g$ = 0–1. We defer a detailed description of the technique and results of the model-atmosphere computations to a later paper. We only note here that, on the whole, the chemical composition of Sakurai's object is similar to those of R CrB stars [8]. Consequently, free–bound absorption by carbon atoms plays a major role at high temperatures ($T_{eff} \approx 7000$ K) over a wide range of wavelengths [24]. At lower effective temperatures, the radiation transfer processes should depend strongly on CN and C_2 molecular band absorption. Our computations showed that, already at $T_{eff} = 6250$ K, inclusion of molecular absorption "shifts" the temperature structure of the model atmosphere toward lower pressures (see Fig. 1). Note that this effect is qualitatively similar to what happens when the matter opacity is increased in model atmospheres for R CrB stars [8, 18].

Table 2. Band systems of diatomic molecules included in the computations

Molecule	System	λ_1, nm	λ_2, nm
C_2	$e^3\Pi_g$–$a^3\Pi_u$ Fox-Herzberg	237.0	328.5
C_2	$d^3\Pi_g$–$a^3\Pi_u$ Swan	340.0	785.0
C_2	$A^1\Pi_u$–$X^1\Sigma_g^+$ Phillips	672.0	1549.0
C_2	$b^3\Sigma_g^-$–$a^3\Pi_u$ Ballik-Ramsay	1100.0	2700.0
CN	$B^2\Sigma^+$–$X^2\Sigma^+$ Violet	240.0	600.0
CN	$A^2\Pi$–$X^2\Sigma^+$ Red	400.0	1500.0
CS	$A^1\Pi$–$X^1\Sigma^+$	240.0	330.0
CO	$A^1\Pi$–$X^1\Sigma^+$	114.0	280.0
CO	$C^1\Sigma^+$–$A^1\Pi$ Herzberg	368.0	571.0
CO	$B^1\Sigma^+$–$A^1\Pi$ Ångsröm	412.0	662.0
NO	$A^2\Sigma^+$–$X^2\Pi_r\,\gamma$	195.0	340.0
NO	$B^2\Pi_r$–$X^2\Pi_r$	200.0	380.0
NO	$C^2\Pi_r$–$X^2\Pi_r\,\delta$	207.0	275.0
MgO	$B^1\Sigma^+$–$X^1\Sigma^+$	454.0	544.0
AlO	$C^2\Pi_r$–$X^2\Sigma^+$	200.0	400.0
AlO	$B^2\Sigma^+$–$X^2\Sigma^+$	404.0	580.0
SiO	$E^1\Sigma^+$–$X^1\Sigma^+$	171.5	200.0
SiO	$A^1\Pi$–$X^1\Sigma^+$	207.0	330.0
SO	$A^3\Pi$–$X^3\Sigma^-$	246.0	380.0
CaO	$C^1\Sigma$–$X^1\Sigma$	730.0	923.0

λ_1, λ_2 are the observed boundaries of the band systems.

2.2. Theoretical Spectra of Sakurai's Object

We performed detailed computations of the spectral energy distribution of Sakurai's object using the WITA6 code, which is a version of the WITA31 code [25]. The main modifications consisted in the use of a more extensive list of opacity sources. Bound–free absorption by CI and OI was computed as in the SAM941 code, using the data of [23] and determining the C^- absorption based on the formulas given in [26]. In addition, the new version of the program uses an algorithm for "screening" spectral-line lists; i.e., absorption lines with intensities below a certain adopted threshold are not included in the synthetic spectra. This procedure reduced the time required to compute the synthetic spectra by more than an order of magnitude.

We computed our synthetic spectra over a wide range of wavelengths ($\lambda\lambda$ 300–1000 nm). We adopted a microturbulent velocity of v_t = 5 km/s and performed most of the computations with a wavelength step of 0.2 nm. Test computations with a smaller step (0.005 nm) indicated that reducing the wavelength step had virtually no effect on the final results. We then convolved the monochromatic fluxes with a Gaussian instrumental profile ($\Delta\lambda_g$ = 1 nm) and converted the resulting fluxes

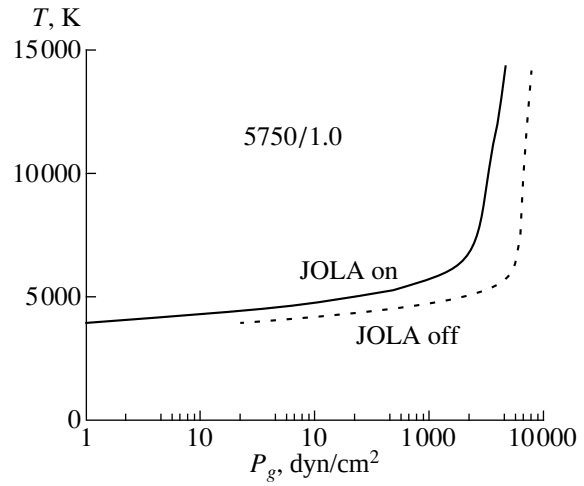

Fig. 1. Temperature structure of Sakurai's object model atmospheres 5750/1.0 computed with (solid curve) and without (dashed curve) molecular opacities.

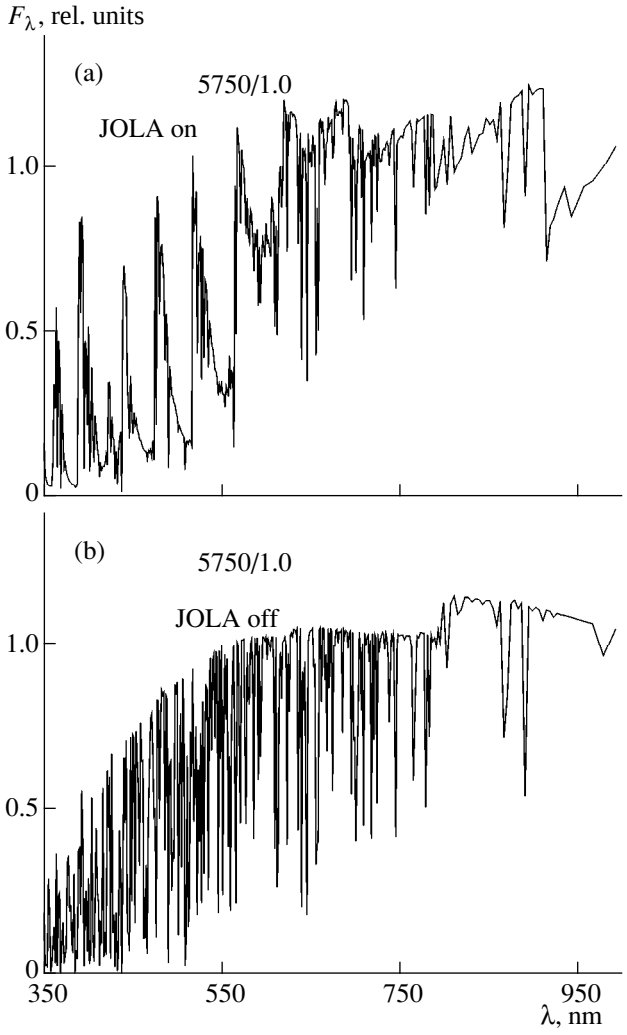

Fig. 2. Theoretical fluxes computed for Sakurai's object model atmospheres 5750/1.0 (a) with and (b) without molecular opacities.

F_ν to F_λ values. To compare the theoretical and observed fluxes, we normalized both to the same flux F_λ at λ 570 nm (near the edge of the C_2 band). We chose this wavelength because it lies in the region where CN molecular absorption is weakest—the bands of the violet system are already weak, and those of the red system are not yet strong. We checked that the choice of this "reference" wavelength does not qualitatively affect our conclusions.

3. RESULTS

3.1. Structure of the Spectra of Sakurai's Object

Figure 2 shows the theoretical emergent fluxes for the model atmosphere computed with $T_{eff}/\log g$ = 5750/1.0 using the opacity sampling technique. We computed two sets of model atmospheres: with and without taking into account molecular opacities in a self-consistent approach, when the temperature structure is determined for a given set of opacity sources. It is evident from the figure that the shape of the theoretical spectra depends critically on the adopted set of opacity sources. The spectrum computed without molecular opacities is similar to the spectra of R CrB stars: It has a large number of rather strong lines, as well as flux jumps near λ 720 and 800 nm due to the wavelength behavior of the CI bound–free absorption [18]. Including the molecular opacities results in the appearance of rather strong C_2 and CN bands in the spectrum beginning at T_{eff} = 6250 K. The molecular-band intensities increase with further decrease of the effective temperature. As a result, the molecular bands dominate in the spectrum of Sakurai's object at T_{eff} = 5750 K (Fig. 2).

Figure 3 shows identifications of the main absorption features in the spectrum. The dashed and thin solid curves show the flux distributions F_ν for individual molecular systems computed for the 5400/1.0 model atmosphere. The bold solid curve shows the observed spectrum of Sakurai's object for April 29, 1997. It is clear that the main absorption features in the observed spectrum can be identified with high confidence. We now note the following:

(1) The shape of the spectrum at 300–1000 nm is determined primarily by three molecular-band systems: the Swan bands of C_2 and the red and violet CN bands. There is a small contribution from the Fox–Hertzberg (in the UV) and Phillips (in the red) bands of C_2.

(2) Features appearing in the spectrum of Sakurai's object as broad bands are made up of sequences of bands with constant $\Delta v = v' - v''$. The molecular-band intensities decrease with v' and v''.

(3) The observed spectrum exhibits strong atoamic lines as well as molecular bands: the Ca^+ H and K (393.48 and 396.96 nm), Na D (589.16 and 589.75 nm), and Ca^+ infrared triplet (850.03, 854.44, and 866.45 nm) lines. Higher resolution spectra are required for a more detailed identification of the atomic lines.

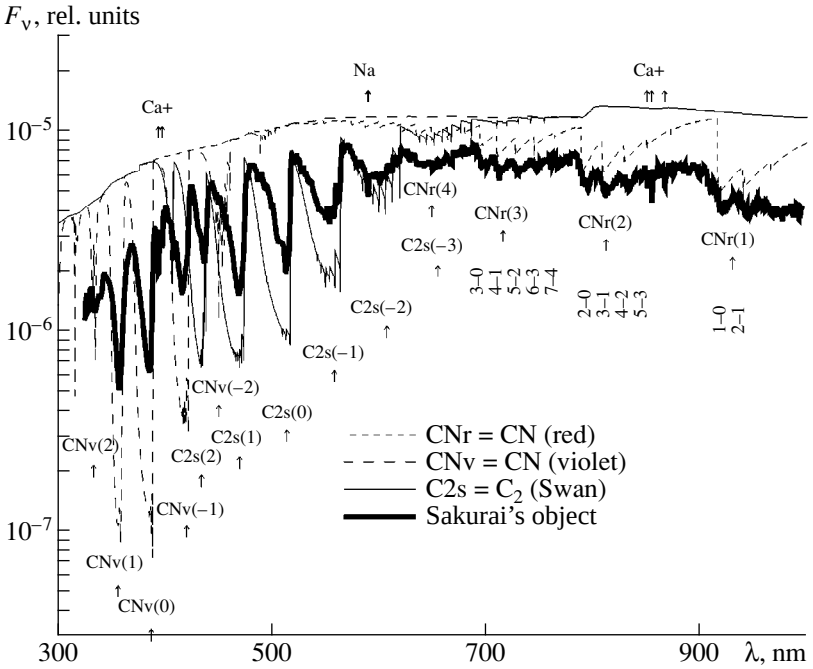

Fig. 3. Comparison of the computed violet and red band systems of CN molecules (dashed curve) and the Swan C_2 molecule system (thin solid curve) with the observed spectral energy distribution of Sakurai's object (heavy solid curve). The differences of the vibrational constants $v'–v''$ for the band that forms the blend in question are given in parentheses. Also given are the vibrational constants for the resolved red bands of CN. The strongest atomic lines in the observed spectrum of Sakurai's object are shown.

(4) In their analysis of the behavior of the observed spectrum of Sakurai's object over a long period, Duerbeck and Benetti [3] identified the heads of the bands of the isotopic molecules $^{12}C^{13}C$ and ^{13}CN in spectra taken in 1997. However, as noted above, analysis of these features lies beyond the scope of this paper.

3.2. Molecular and Atomic Absorption

Thus, the main features in the spectrum of Sakurai's object are produced by absorption due to diatomic-molecule band systems. Note that synthetic spectra should be computed taking into account bound–bound atomic and ion opacities in order to more realistically reproduce the observed spectrum. Indeed, including atomic-line opacities improves the agreement between the observed and computed UV spectra (Fig. 4) and, in particular, reduces the discrepancies in front of the molecular-band heads. The contribution of molecular-band absorption to the total opacity is minimum at these wavelengths, and, as follows from Fig. 4, the fluxes computed without allowance for atomic absorption are clearly overestimated.

This effect is most pronounced at short wavelengths, where most of the atomic and ion lines lie. However, in the red part of the spectrum, too, we can see that the energy distribution changes in response to changes in the temperature structure of the model atmosphere when atomic-line absorption is "turned off." Note that even models computed with allowance for atomic-line absorption overestimate the fluxes at short wavelengths. This could be due to several factors.

(1) We performed our computations for a plane-parallel geometry. Including the effects of sphericity could change the temperature gradient of the resulting model atmosphere and, consequently, affect the profiles of individual molecular bands.

(2) Clearly, our model does not include all continuum opacity sources [27, 28]. Unidentified opacity sources in the atmospheres of cool stars also pose a problem in the UV and blue parts of the spectrum.

(3) The adopted atomic line lists might be insufficiently complete, so that our model underestimates blanketing at short wavelengths.

(4) The list of molecular features contributing substantially to absorption could be insufficiently complete. For example, lack of data prevented us from including the Deslandres–d'Ambuja ($C^1\Pi_g–A^1\Pi_u$) and Messerle–Krauss ($C'^1\Pi_g–A^1\Pi_u$) bands of C_2, which could contribute to absorption at $\lambda < 400$ nm ($\lambda\lambda$ 339–378 nm), and bands of isotopic molecules containing ^{13}C. Inclusion of these features could, in principle, somewhat smooth the flux jumps in the theoretical spectrum.

(5) Our computations took into account only transitions between molecular vibrational states with quantum numbers v', $v'' < 10$. The rather high temperatures involved require models with more complete matrixes of Franck–Condon factors.

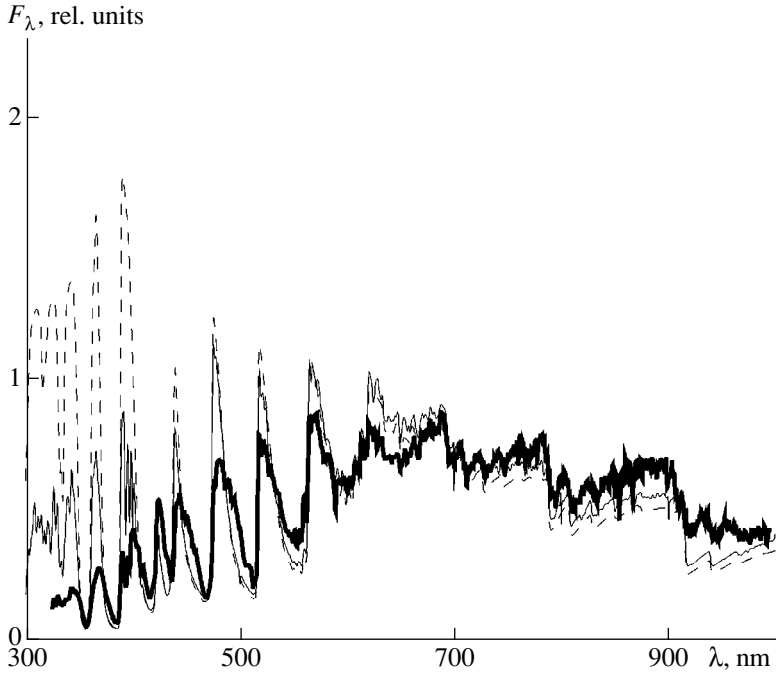

Fig. 4. The observed spectral flux distribution of Sakurai's object (heavy solid curve) and fluxes computed with (thin solid curve) and without (dashed curve) allowance for opacities for the corresponding model atmospheres with parameters 5400/1.0.

(6) Dust scattering ($\sigma \sim 1/\lambda^n$) can also increase the short-wavelength opacity. See the discussion of interpretations of observational data in terms of dust-shell models in [3].

(7) The fact that our computations systematically overestimate the depths of the C_2 bands in the visible spectrum can also be interpreted in terms of the well-known, but thus far only partially explained, phenomenon of "enhanced carbon lines" exhibited by R CrB stars [8, 29].

In any case, no definitive conclusions can be made without new complex analyses of the spectra of Sakurai's object.

3.3. Effective Temperature Dependence of the Spectral Energy Distribution

Since molecular bands are already important in the spectrum of Sakurai's object at $T_{eff} = 6200$ K, we expect the computed spectral energy distributions to depend appreciably on the effective temperature. The concentrations of C_2 and CN molecules, whose absorption determines the spectral energy distribution at temperatures as high as $T_{eff} = 6200$ K, increase with decreasing effective temperature. As a result, the intensity of the corresponding molecular bands decreases, which changes the shape of the spectral energy distribution. Our computations showed the overall spectral energy distribution of Sakurai's object to vary substantially as the effective temperature was decreased. This is primarily due to enhancement of bands of carbon-containing molecules. Our comparison of the observed fluxes with the fluxes computed for model atmospheres with $T_{eff} =$ 5000–6000 K indicated that the observed spectrum is best reproduced when $T_{eff} \sim$ 5250–5500 K (Fig. 5).

Note that the rather good *qualitative* agreement between the observed and computed spectral profiles and relative intensities over a wide range of wavelengths suggests that we have identified all the main molecular-opacity sources in the atmosphere of Sakurai's object (see, however, the following section).

3.4. Dependence on $\log g$

Problems connected with determining the gravity in the atmosphere of Sakurai's object are discussed in [5]. Here, we adopted $\log g = 1.0$, which can be considered an upper limit. The actual $\log g$ values must have been lower in April 1997. Note, however, that the effects of sphericity increase rather rapidly with decreasing gravity. As noted above, we performed our computations for a plane-parallel geometry. We preferred to remain within the domain of applicability of this approximation in our modeling but nevertheless investigated the influence of $\log g$ on the computed spectra.

Generally speaking, the $\log g$ dependence of the spectra stems from variations both in the temperature structure of the model atmosphere and in the ionization–dissociation equilibrium, due to increases or decreases of the gas pressure in the reversing layer where the atomic and molecular spectrum forms. Our

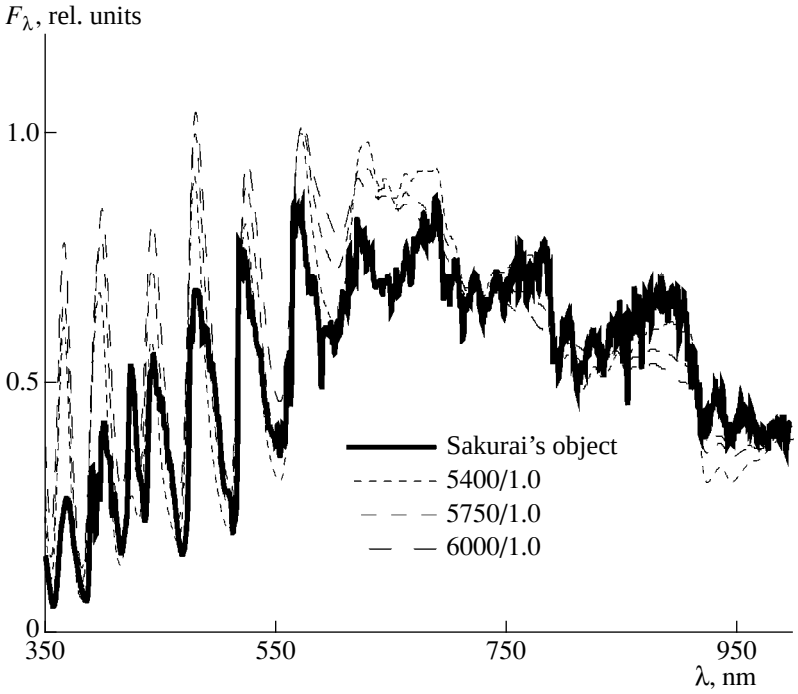

Fig. 5. Comparison of the observed spectral flux distributions of Sakurai's object and the spectral flux distributions computed for model atmospheres with various T_{eff}.

computations show that the temperature distribution $T = f(\tau)$ shifts towards higher P_g as $\log g$ decreases. On the whole, this effect is qualitatively similar to the result of an atmospheric opacity decrease (Fig. 1).

Figure 6 shows the energy distributions computed for model atmospheres 5500/1.0 and 5500/0.0. It is clear from the figure that an order of magnitude gravity change significantly affects the energy distribution. This becomes especially evident if we compare the relative fluxes in the red and blue regions of the spectrum. Note that the changes in the red part of the spectrum are more significant. Clearly, this can be explained by the fact that the bands of the red CN system are not saturated in our case. The saturated bands of the short-wavelength (violet) CN system respond rather weakly to changes in $\log g$.

Clearly, the approximations we have used prevent us from estimating the effects of sphericity on the $\log g$ dependence of the spectra. There is no doubt that the role of these effects should increase with luminosity, and enhanced atmospheric stratification, dust formation, etc., could become significant in more luminous stars.

3.5. Dependence on the Chemical Composition

Variations of the chemical composition always produce substantial changes in the chemical equilibrium, and, consequently, in the emergent flux, which are superimposed on effects due to structural changes of the stellar atmosphere resulting from enhanced or weakened blanketing. On the whole, the resulting pattern is rather complex; different spectral regions respond in different ways to changes in the H, C, N, and O abundances. Figure 7 compares the observed spectrum of Sakurai's object with two theoretical spectra computed using model atmospheres with the same T_{eff} and $\log g$ but different nitrogen abundances, $\log N\,(\mathrm{N}) = -2.53$ and -2.03. A 0.5 dex increase in the nitrogen abundance appreciably changes the spectrum near the CN bands, while leaving the spectrum near the Swan bands of C_2 virtually unaffected. The small changes in the emergent fluxes in this spectral region are due to variations in the temperature structure of the model atmosphere, which responds to changes in $\log N\,(\mathrm{N})$. It is difficult to say anything about the atmospheric nitrogen abundance of Sakurai's object based on such data; however, we can see that $\log N\,(\mathrm{N}) = -2.53$ [8] yields a better fit to the observed spectrum than $\log N\,(\mathrm{N}) = -2.03$.

With decreasing atmospheric hydrogen abundance, the outer part of the convective envelope located under the photosphere shifts toward higher P_g. According to our computations, a decrease in the hydrogen abundance by two orders of magnitude (down to the atmospheric abundance of R CrB, $\log N\,(\mathrm{H}) = -4.029$) has virtually no effect on the theoretical energy distribution. Thus, our conclusions are applicable to objects with lower atmospheric hydrogen abundances, which may be discovered in the future.

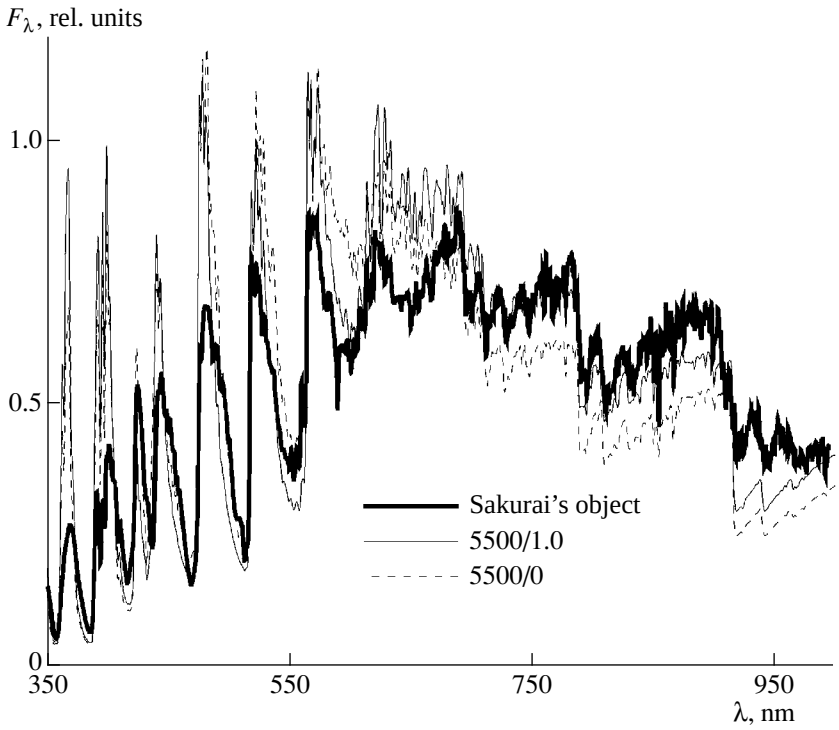

Fig. 6. Comparison of the observed spectral flux distributions of Sakurai's object and the spectral flux distributions computed for model atmospheres with T_{eff} = 5500 K and $\log g$ = 1.0 and 0.0.

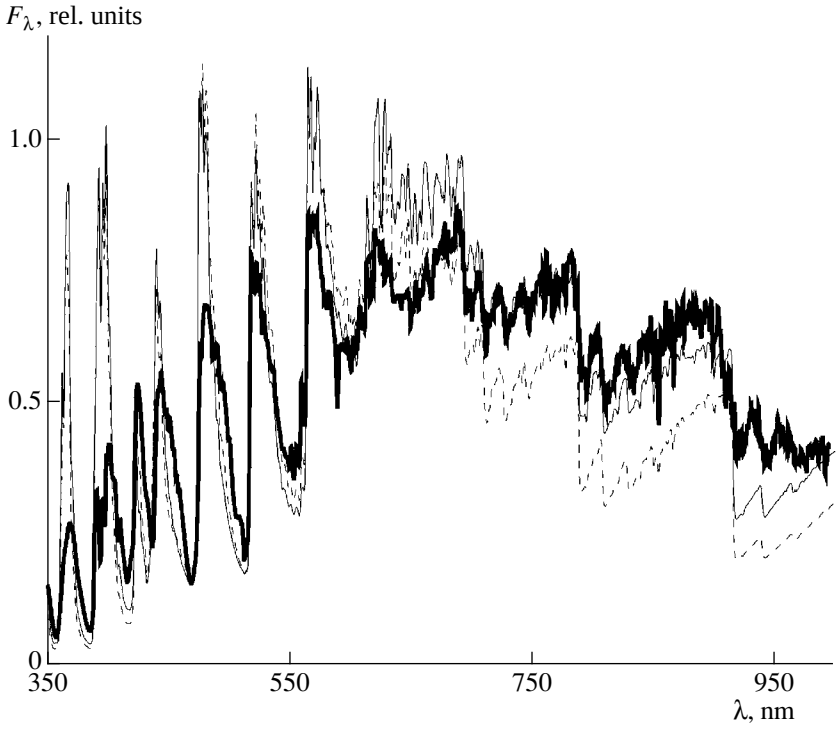

Fig. 7. Comparison of the observed spectral flux distribution of Sakurai's object (heavy solid curve) and the spectral flux distributions computed for model atmospheres 5400/1.0 with various nitrogen abundances: $\log N$ (N) = –2.53 (thin solid curve) and $\log N$ (N) = –2.03 (dashed curve).

4. DISCUSSION OF RESULTS

First and foremost, we note that our results are model dependent. We have modeled the spectra of Sakurai's object in a simplified treatment of the radiation transfer in the star's atmosphere. However, we consider our approach to be quite justified, since it is not yet possible to model the spectra of such complex objects in a fully self-consistent and rigorous way.

Note also that our use of the JOLA technique to derive the molecular-band profiles (see above) enabled us to compute the model atmospheres and theoretical spectra throughout the entire visible and IR spectrum taking into account the molecular opacities.

We have obtained the following main results:

(1) We computed a grid of model atmospheres in the framework of classical approximations covering the effective-temperature and gravity intervals T_{eff} = 5000–6250 K and $\log g = 0.0 \sim 1.0$ for the adopted atmospheric chemical composition of Sakurai's object [8, 11].

(2) We obtained a good qualitative agreement between the theoretical and observed spectral energy distributions of Sakurai's object. This enabled us to confidently identify the main absorption features in a spectrum taken in April 1997. These features are formed by the violet and red CN-band systems and also by the Swan C_2 bands. We have also established the main opacity sources in the atmosphere of Sakurai's object.

(3) Comparison of the theoretical and observed fluxes showed that the computations overestimated the short-wavelength fluxes. Certain discrepancies are also observed in the red. All this hinders accurate estimation of the atmospheric parameters for Sakurai's object.

(4) Our results suggest that the effective temperature of Sakurai's object did not differ substantially from 5400 K in April 1997. It is difficult to determine $\log g$ with confidence, since the model should include the effects of atmospheric sphericity in order to adequately estimate this quantity.

We should bear in mind the following points when assessing the reliability of the results obtained.

We computed our model atmospheres using classical approximations. The most controversial of these is the assumption of a plane-parallel geometry for the atmosphere. Clearly, with time, the atmosphere of Sakurai's object should expand and cool, enhancing sphericity effects, which are likely partially responsible for the discrepancies between the observed and computed spectra (Fig. 5). This makes the rather good agreement between the observed and theoretical spectra even more remarkable. However, we nevertheless consider an analysis of sphericity effects in the spectra of Sakurai's object to be of considerable importance. No definitive conclusions are possible without a self-consistent analysis of this problem. Such an analysis should involve simultaneous determination of the T_{eff}, $\log g$, v_t, and chemical composition for the corresponding (strictly speaking, inhomogeneous) model atmospheres that accurately reproduce the energy distribution in the spectrum.

The JOLA treatment of molecular opacities might be insufficiently accurate for computing the profiles of weak molecular bands [30]; however, such lines contribute only slightly to the total absorption. As noted above, molecular absorption in the atmosphere of Sakurai's object becomes important at effective temperatures as high as $T_{eff} \sim 6000$ K. However, when $T_{eff} > 5700$ K, blanketing at short wavelengths is determined primarily by rather strong atomic and free–bound CI absorption, so that the errors in the computed molecular opacities are not so critical in this case.

It is our opinion that the discrepancies between the observed molecular-band intensities in the blue region of the spectrum and our computed intensities are mainly due to the effect of the dust component of the atmosphere and/or shell on the photospheric radiation field. A detailed analysis of the effects of dust on the spectrum lies beyond the scope of this paper.

The computed model atmospheres and synthetic spectra could also be affected by uncertainties in estimates of the chemical composition of Sakurai's object.

Our estimate of the effective temperature (T_{eff} = 5400 K) is lower than the value T_{eff} = 7250 K inferred in [9] for July 1996. At the same time, using the photometric calibration for normal C giants, Arkhipova *et al.* [3] obtained T_{eff} = 5100 K and even T_{eff} = 4600 K in March and June 1997, respectively. Although these last three estimates differ slightly from those we have inferred, we should bear in mind the problems that can be encountered in the spectral classification (and, consequently, in the effective-temperature determination) for objects with anomalous chemical compositions. It is unquestionably encouraging that these T_{eff} estimates were derived using fundamentally different methods. On the whole, the results obtained fit quite well a picture in which Sakurai's object is gradual cooling. Note once again that we estimated the effective temperature in April 1997 in a self-consistent analysis, computing the spectral energy distribution using model atmospheres with known effective temperatures and chemical composition.

Although our results could be subject to the uncertainties indicated above, their reliability can nevertheless be tested directly via comparison with observations. Our computations of the spectral energy distribution of Sakurai's object demonstrate that it is fundamentally possible to theoretically interpret the observed spectra of Sakurai's object. We plan to continue this work and invite observers to take part in joint studies of this, thus far, absolutely unique object.

5. ACKNOWLEDGMENTS

We thank Dr. H. Duerbeck for providing us with observational data in electronic form, Prof. T. Kipper and Dr. M. Asplund for fruitful discussions of model-

atmosphere computations for hydrogen deficient stars, and the compilers of the VALD database for quality service. We are also grateful for the very useful comments made by the referee.

REFERENCES

1. S. Nakano, Y. Sakurai, M. Hazen, *et al.*, IAU Circ. No. 6322, 1 (1996).
2. S. Kimeswenger and F. Kerber, Astron. Astrophys. **330**, 41 (1998).
3. V. P. Arkhipova, V. F. Esipov, R. I. Noskova, *et al.*, Pis'ma Astron. Zh. **24**, 297 (1998).
4. H. W. Duerbeck and S. Benetti, J. Astron. **468**, 111 (1996).
5. H. W. Duerbeck, S. Benetti, A. Gautschy, *et al.*, J. Astron. **114**, 1657 (1997).
6. I. Iben, Astrophys. J. **277**, 333 (1984).
7. V. P. Arkhipova and R. I. Noskova, Pis'ma Astron. Zh. **22**, 709 (1996).
8. M. Asplund, B. Gustafsson, D. L. Lambert, *et al.*, Astron. Astrophys. **321**, 17 (1997).
9. T. Kipper and V. Klochkova, Astron. Astrophys. **324**, 65 (1997).
10. M. D. Shetrone and M. Keane, *Faint Blue Stars*, Ed. by A. G. Davis-Philip (Davis Press, Schnectady, 1997).
11. M. Asplund, B. Gustafsson, N. K. Rao, *et al.*, Astron. Astrophys. **343**, 507 (1999).
12. T. Tsuji, Astron. Astrophys. **23**, 411 (1973).
13. R. L.Kurucz, Spec. Rep. Smithsonian Astrophys. Obs. **309**, 1 (1970).
14. S. E. Nersisyan, A. V. Shavrina, and A. A. Yaremchuk, Astrofizika **30**, 249 (1989).
15. K. P. Huber and G. Herzberg, *Constants of Diatomic Molecules* (Van Nostrand Reinolds, New York, 1979).
16. N. E. Kuz'menko, L. A. Kuznetsova, and Yu. A. Kuzyakov, *Franck–Condon Factors for Diatom Molecules* (Moscow State University, Moscow, 1984), p. 342.
17. L. A. Kuznetsova, N. E. Kuz'menko, Yu. A. Kuzyakov, *et al.*, *Probabilities for Optical Transitions of Diatomic Molecules* (Nauka, Moscow, 1980), p. 315.
18. Ya. V. Pavlenko, Astron. Zh. **76**, 115 (1999).
19. R. L. Kurucz, CD ROM No. 13.
20. C. H. Sneden, H. Johnson, and B. Krupp, Astrophys. J. **204**, 281 (1976).
21. D. Mihalas, *Stellar Atmospheres* (Freeman, San Francisco, 1978; Mir, Moscow, 1982).
22. N. E. Piskunov, F. Kupka, and T. A. Ryabchikova, Astron. Astrophys., Suppl. Ser. **112**, 525 (1996).
23. D. Hoffsaess, Atom. Data Nucl. Data Tab. **24**, 285 (1979).
24. V. P. Myerscough, Astrophys. J. **153**, 421 (1968).
25. Ya. V. Pavlenko, Astrophys. Space Sci. **253**, 43 (1997).
26. V. P. Myerscough and M. R. C. McDowell, Astrophys. J. **132**, 457 (1996).
27. L. A. Yakovina and Ya. V. Pavlenko, Kinematika i Fizika Nebesnykh Tel **14**, 257 (1998).
28. S. C. Balachandran and R. A. Bell, Nature **392**, 791 (1998).
29. B. Gustafsson and B. Asplund, Astron. Soc. Pac. Conf. Ser. **96**, 27 (1996).
30. T. Tsuji, *Molecules in Stellar Environment*, Ed. by U. G. Jorgensen (Springer), p. 79.

Translated by A. Dambis

Astronomy Reports, Vol. 44, No. 4, 2000, pp. 219–226. Translated from Astronomicheskiĭ Zhurnal, Vol. 77, No. 4, 2000, pp. 254–263.

Lithium Lines in the Spectra of M Dwarfs: UX Tau C

Ya. V. Pavlenko

Main Astronomical Observatory, Goloseevo, Kiev-127, 03680 Ukraine

Received April 20, 1999

Abstract—The results of numerical modeling of lithium lines in the spectra of M dwarfs are discussed. The behavior of the lithium lines relative to the local pseudocontinuum formed by molecular bands is analyzed as a function of model atmosphere parameters: effective temperature $T_{\rm eff}$, gravity $\log g$, and metallicity μ. The molecular opacity was computed using the just overlapping line approximation (JOLA) and "line-by-line" methods. The pseudo-equivalent widths of lithium lines depend appreciably on metallicity μ and weakly on $T_{\rm eff}$. The lithium abundance in the atmosphere of UX Tau C is redetermined. Previous studies underestimated the lithium abundance in this star as a result of the use of insufficiently accurate molecular-line lists. The new lithium abundance $\log N\,({\rm Li}) = 3.2 \pm 0.3$ was derived by comparing the observed profiles of the 670.8 nm resonance doublet lines with profiles calculated using the new TiO line list of Plez.[1] The new abundance agrees with the atmospheric lithium abundances of the other two components in the stellar system, providing further evidence that the three stars in the UX Tau system have the same age. A comparison of the observed spectra of UX Tau C near the lithium resonance doublet (665–680 nm) with spectra computed using JOLA and line-by-line methods suggests that the list of Plez is the best currently available. © *2000 MAIK "Nauka/Interperiodica".*

1. INTRODUCTION

Studies of lithium depletion in the early stages of stellar evolution have progressed substantially in recent years due to the efforts of both observers and theorists. Stellar-evolution theory predicts [1] that low-mass, pre-main-sequence (T Tau) stars maintain their initial lithium abundances ($\log N\,({\rm Li}) \sim 3.2$[2] [2]) for several million years.

On the other hand, numerical modeling of lithium lines in the spectra of late-type dwarfs can be used to identify brown dwarfs—star-like objects in whose interiors lithium does not burn at all. Rebolo *et al.* [3] and Magazzu *et al.* [4] used this as the basis for a "lithium test." The boundary on the Hertzsprung–Russell diagram separating brown dwarfs and M dwarfs passes near spectral type M6.5, which corresponds to masses $M_* = 0.08$–$0.065 M_\odot$ [5]. According to our current understanding, brown dwarfs are most likely to be detected among M dwarfs in relatively young clusters: the Pleiades, Hyades, and α Per. The first lists of such low-mass objects [6, 7] have been recently compiled based on photometric monitoring of these clusters. Naturally, only young brown dwarfs in the stage of gravitational contraction, like M dwarfs, can be found in such clusters. Brown dwarfs have preserved their initial lithium, so that the spectra of these stars should exhibit strong lithium lines. Rather strong LiI λ 670.8 nm absorption doublets have, indeed, been detected in the spectra of Teide1 and Calar3—the first brown dwarfs found in the Pleiades [8]. The main problem with analyzing these features in the spectra of late dwarfs and young brown dwarfs is that they appear against a background of strong molecular bands. In the first part of this paper, we analyze how the strengths of lithium lines relative to the molecular-band background in the spectra of M dwarfs with various $T_{\rm eff}$, $\log g$, and metallicity μ depend on the lithium abundance.

Magazzu *et al.* [2] and Martin *et al.* [9] provided convincing evidence that, in contrast to brown dwarfs, young M dwarfs ($M_* < 0.2\,M_\odot$) have already decreased their lithium abundances in the early stages of their evolution. Garcia Lopez *et al.* [10] and Zapatero Osorio *et al.* [11] showed that the lithium in the atmospheres of M dwarfs in the Pleiades and α Per clusters (with ages ~120 and 50 million years, respectively) have been reduced by factors exceeding 1000. Moreover, the efficiency of lithium depletion depends on the star's evolutionary age and mass.

Generally speaking, studies of late M dwarfs are hindered by ambiguities in estimates of their masses and ages. Restricting consideration to cluster members can reduce these uncertainties. For example, using the results of Pavlenko *et al.* [13], Oppenheimer *et al.* [12] identified two lithium-rich M dwarfs (HHJ 339 and HHJ 430) in the Pleiades. The high lithium abundances of these stars ($\log N\,({\rm Li}) = 3.0$ and 2.6, respectively) suggest that they are young ($t < 20$ Myr).

Analyses of observations of M dwarfs in multiple systems should yield much more definitive results. This is of interest for assessing the results of Magazzu *et al.* [14], who studied the stars of the triple system UX Tau. This system consists of two intermediate-mass T Tau stars (UX Tau A and B, with masses of 1.0 and 0.6 $M_\odot$,

[1] See Astron. Astrophys. **337**, 495 (1998).

[2] Here, we use an abundance scale in which $\log N\,({\rm N}) = 12$.

respectively) and a third, fainter component UX Tau C ($M_* \leq 0.2\ M_\odot$, M6IV, $T_{\rm eff} \approx 3100$ K) about 2–3 arcsec from UX Tau A. Note that the mass of UX Tau C is close to the mass limit separating M stars from brown dwarfs.

The spectra of all the components exhibit strong LiI lines. However, Magazzu *et al.* [14] found the three components to have substantially different atmospheric lithium abundances: $\log N\,(\mathrm{Li}) = 3.2$, 3.1, and 2.3 for UX Tau A, B, and C, respectively. Later, Pavlenko *et al.* [13] inferred $\log N\,(\mathrm{Li}) \simeq 2.0$ for UX Tau C using the model-atmosphere grid of [15]. The only way to explain such a low $\log N\,(\mathrm{Li})$ in the atmosphere of UX Tau C is to assume that this component is older than the rest of the stellar system; the age of the UX Tau system is $t \approx 2.6$ million years [16]. Theory predicts that, at this evolutionary stage, UX Tau C should be in its deuterium burning phase, and there should be no lithium destruction occurring in the stellar interior. On the other hand, triple stars are very unlikely to form from components with different ages. It may be that the low lithium abundances in the atmosphere of UX Tau C inferred in previous studies reflect uncertainties (errors) in the input data (model atmospheres or line lists). We examine this issue in the second section of the paper.

As observational material, we use spectra of UX Tau C kindly provided by Dr. R. Rebolo. See [14] for a detailed description of these spectra and the data reduction procedure.

2. MODEL COMPUTATION TECHNIQUE

We now note a number of issues in connection with modeling lithium lines in the atmospheres of late M dwarfs (see also [13]):

(1) Only the cores of strong lithium lines can be observed in the spectra of late M dwarfs. Even these lines "penetrate" the background of strong molecular bands only in atmospheres with high lithium abundances.

(2) Of special interest is the atmospheric lithium abundance interval 2.0–3.5 occupied by M dwarfs that are brown dwarf candidates.

(3) In stellar atmospheres with $T_{\rm eff} < 3200$ K, lithium exists mainly in the form of neutral atoms. Therefore, in this case, decreasing $T_{\rm eff}$ does not efficiently increase the number of absorbing LiI atoms in the stellar atmosphere, as is the case in stars with higher $T_{\rm eff}$.

(4) In the atmospheres of late M dwarfs, the TiO dissociation equilibrium is saturated; i.e., the TiO molecular densities depend only slightly on temperature, since most of the titanium atoms are bound in TiO molecules [17].

We considered model atmospheres with 2500 K $< T_{\rm eff} <$ 3400 K; $\log g = 4.5$, 5.0; and metallicities $\mu = 0$, –1 from the grid of [18]. We computed our synthetic spectra using the WITA612 code [19]. When solving the system of equations for ionization–dissociation equilibrium, we took into account 98 species, including lithium molecules [13]. We took data for molecular constants from [17]. The shape of the spectrum near the λ 670.8 and 821.6 nm lithium lines modeled here is determined primarily by TiO absorption bands. We adopted a TiO dissociation potential of $D_0 = 6.92$ eV; however, our results depend only slightly on D_0 due to saturation effects. The molecular opacities were computed using both "line-by-line" and "just overlapping line approximation" (JOLA) methods. We used several different molecular-line lists in our line-by-line computations and used the molecular-band data from [13] for the JOLA computations. We used this JOLA model to analyze the spectra of the young Pleiades brown dwarfs Teide1 and Calar3 in [19]. The effective temperatures of these two M dwarfs ($T_{\rm eff} \approx 2700$ K) are lower than that of UX Tau C.

3. RESULTS

To test whether the JOLA technique can be used to synthesize the spectrum of UX Tau C, we reproduced the $\lambda\lambda$ 600–900 nm energy distribution in the spectrum of the M dwarf GJ51. The observed spectrum of GJ51 was kindly provided by Dr. M. R. Zapatero-Osorio. The spectral type of GJ51 (M5.5) is close to that of UX Tau C; however, GJ51 does not have lithium lines in its spectrum; i.e., this M dwarf is at a later evolutionary stage.

Figure 1 compares the observed flux distribution F_λ in the spectrum of GJ51 with the flux distribution computed using our model with parameters $T_{\rm eff}/\log g/[\mu] =$ 3100/4.5/0. The observed and computed spectra have been "normalized," i.e., reduced to the same F_λ at a selected wavelength λ_n ($\lambda_n = 800$ nm in Fig. 1 [19]). We will denote such normalized fluxes by F^*_λ.

3.1. Lithium Lines Against a Molecular-Band Background

Following [20], we define the "pseudoequivalent widths" W^J_λ of the lithium lines to be the equivalent widths measured relative to the local pseudocontinuum in the vicinity of the lithium lines, i.e., relative to the continuum formed by the computed JOLA molecular-band profile:

$$W^J_\lambda = \int (1 - F^{\rm JOLA\,+\,Li}_\lambda / F^{\rm JOLA}_\lambda)\, d\lambda.$$

Clearly, W^J_λ is a fundamentally different quantity than the "true" equivalent widths computed by Pavlenko *et al.* [13] using the model-atmosphere grid of [18]. In addition, W^J_λ differs from the equivalent widths computed relative to the pseudocontinua determined in wider spectral intervals. Figure 2 shows a portion of the observed spectrum of UX Tau C containing the 670.8 nm

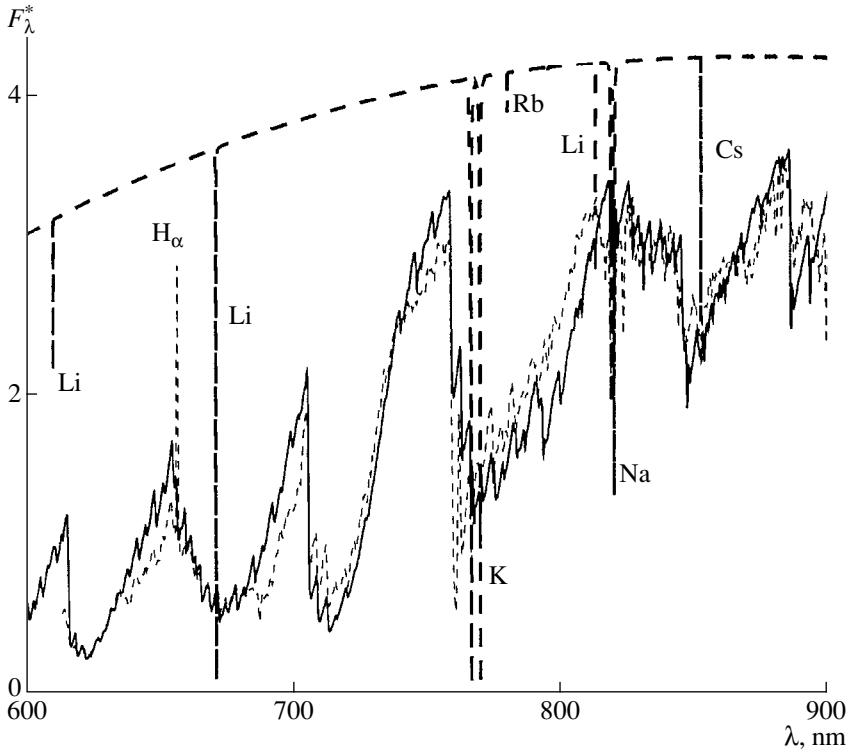

Fig. 1. Comparison of the observed and computed flux distributions in the spectrum of GJ51 (thin dashed and solid curves, respectively). The spectrum was computed using the JOLA molecular opacity model and our model atmosphere 3100/4.5/0. Also shown are the strongest atomic lines detectable in the visible spectra of M and L dwarfs [33] (heavy dashed curves).

LiI resonance doublet. In their analysis of this spectrum, Magazzu *et al.* [14] found the resonance doublet to have an equivalent width of about 80 nm; i.e., their pseudocontinuum lies at the level denoted F_m in Fig. 2.

In this connection, we emphasize the following points:

(1) The equivalent width of the Li doublet measured relative to the local pseudocontinuum near the lithium lines F_l (Fig. 2) is less than 63 pm. Basri *et al.* [21] inferred an equivalent width of 62 ± 1 pm for the lithium resonance doublet using much higher quality spectra of UX Tau C (0.01-nm resolution HIRES spectrograms obtained with the KECK telescope). Note that the pseudocontinuum level adopted by Basri *et al.* corresponds to F_l (see also Fig. 2 in [21]).

(2) This latter local pseudocontinuum agrees best with the fluxes near the resonance lithium doublet inferred using the JOLA method.

(3) The procedure for determining the local pseudocontinuum F_l seems much less ambiguous due to the very nature of the molecular absorption. Indeed, each element of the sawtooth pattern determining the shape of the dominating TiO band (with vibrational numbers $v' - v''$) in the vicinity of the absorption lines produces its own "pseudocontinuum" (Fig. 1).

Note that, to reproduce the observed profiles of the resonance lithium doublet in the spectrum of UX Tau C with the JOLA molecular-opacity model, we set $\log N(\mathrm{Li}) \approx 3.2$. This result is an order of magnitude higher than previous estimates of the atmospheric lithium abundance.

Figures 3 and 4 show "curves of growth" $W_\lambda^J = f(\log N(\mathrm{Li}))$ for the resonance (λ 670.8 nm) and subordinate (λ 812.6 nm) lithium doublets computed for a number of model atmospheres from [18]. The curves of growth in Fig. 3 yield lithium abundances of $\log N(\mathrm{Li}) = 3.5$ and 3.6 for $W_\lambda^J = 60$ and 63 pm, respectively. Clearly, these "curves of growth" can provide only qualitative estimates of the lithium abundances. However, these results suggest a high lithium abundance in the atmosphere of UX Tau C.

We now make note of a number of other results.

(1) W_λ^J depends only slightly on T_{eff} in the temperature interval $2500\ \mathrm{K} < T_{\mathrm{eff}} < 3100\ \mathrm{K}$ (see also [20]). This is of interest for determinations of lithium abundances in brown dwarf atmospheres, whose effective temperature are only rather poorly known.

(2) Decreasing $\log g$ from 5.0 to 4.5 increases W_λ^J for the resonance doublet [by 10% if $\log N(\mathrm{Li}) = 3.2$]. This effect can be explained in a natural way by the decrease of the TiO-band intensity as $\log g$ decreases: The subgiant and giant spectra are known to have stron-

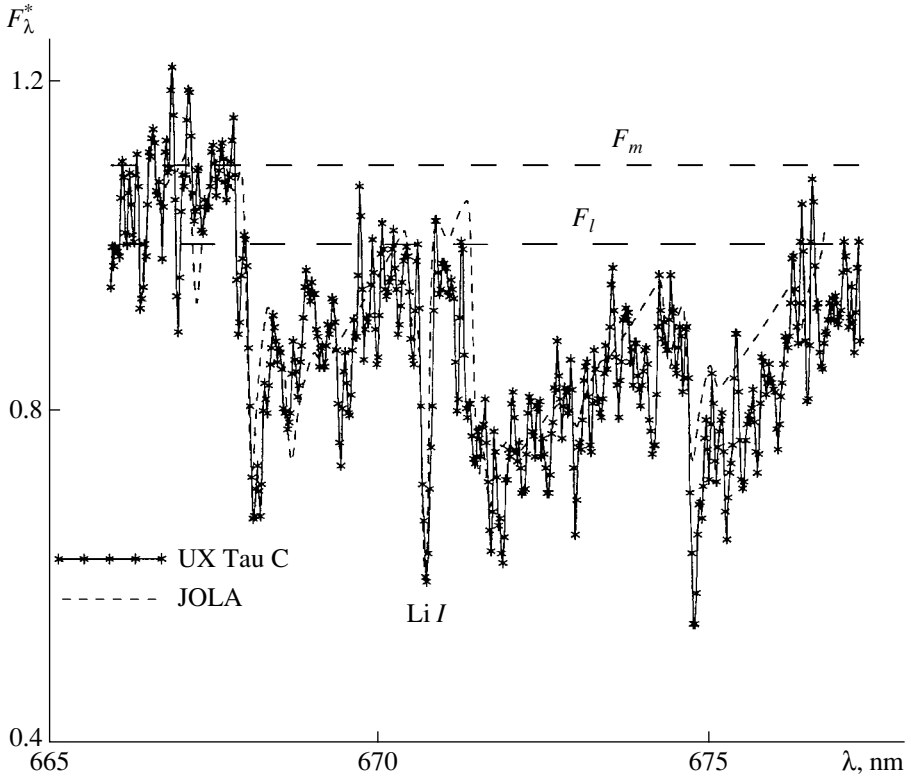

Fig. 2. Observed flux distribution in the spectrum of UX Tau C and fluxes computed using the JOLA molecular emission model (model atmosphere 3100/4.5/0). Also shown are the positions of the pseudocontinuum F_m [14] and local pseudocontinuum F_l.

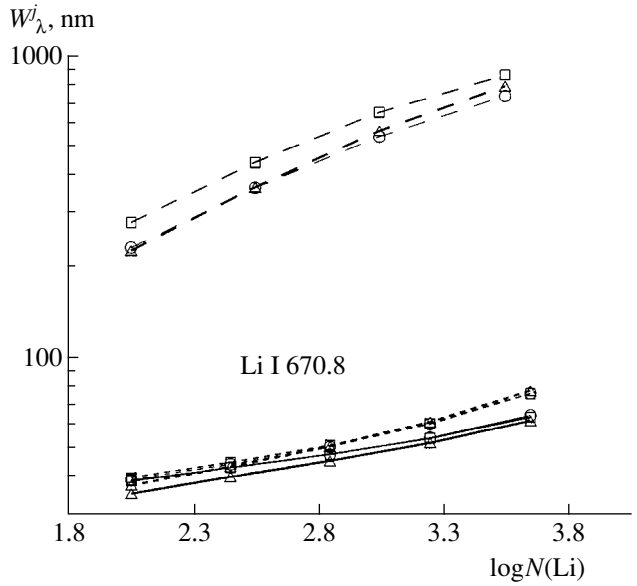

Fig. 3. Curves of growth for pseudoequivalent widths of the λ 670.8 nm lithium resonance lines computed using the model atmosphere grid [18] with (1) $T_{\rm eff}$ = 2500 K (circles), 2700 K (squares), and 3000 K (triangles) and (2) $\log g$ = 4.5 (solid curves), 5.0 (short-dashed curves) for [μ] = 0 and $\log g$ = 5.0 for [μ] = –1 (long-dashed curves).

ger TiO molecular bands than the dwarf spectra. The subordinate lithium doublet at 812.6 nm depends less on $\log g$, since the molecular opacity is weaker in this case. However, in the spectra of stars with high $\log g$ values, this spectral region could be blended with the strong wings of the subordinate sodium triplet (λλ 8194.79, 8194.82, and 8183.25 nm). Moreover, VO absorption becomes important at these wavelengths (the $B^4\Pi$–$X^4\Delta$ band system, see [19]).

(3) At the same time, the effect of metallicity on the equivalent widths of the lithium lines W^J_λ is rather strong and can be explained in a natural way by the dependence of the molecular opacity on μ. The densities of the absorbing molecules in the atmosphere decrease as the metallicity decreases. The weaker the blanketing effect in the vicinity of the lithium lines, the closer the pseudocontinuum is to the real continuum. As a result, the "pseudoequivalent widths" of the lithium lines increase compared to the case of normal chemical composition. For $T_{\rm eff}$ = 2500 K, an order-of-magnitude decrease of μ translates into an increase in the equivalent widths W^J_λ of the λ 670.8 and 812.6 nm features by factors of 10 and 3, respectively. This is due to both the metallicity decrease and to changes in the internal structure of the underlying model atmosphere. The

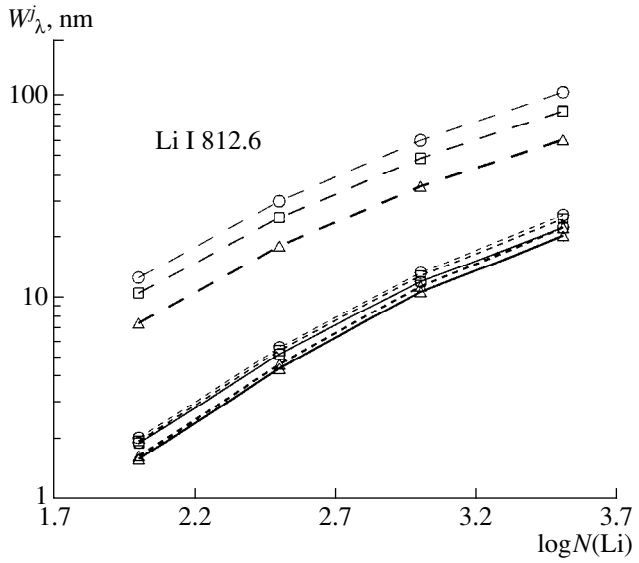

Fig. 4. Same as in Fig. 3 for the lines of the Li I λ 812.6 nm subordinate doublet.

effect is stronger when the λ 670.8 nm resonance lithium line is located in a more blended spectral region.

3.2. Atmospheric Li Abundance of UX Tau C

Since lithium absorption lines in the spectra of late M dwarfs are blended with numerous molecular features, the atmospheric abundances $\log N$ (Li) derived for such stars can, in principle, depend on the completeness of the adopted lists of (molecular) absorption lines. The atmospheric opacities of late M dwarfs near resonance lithium lines are primarily due to absorption by the TiO-band γ and γ' systems [19]. Until recently, the most complete list of TiO absorption lines was that computed by Kurucz [22]. However, Kurucz's data were intended to take into account blanketing in model atmospheres, not to be used for computing synthetic spectra for oxygen-sequence stars. Refined line lists have been published recently by Plez [23] and Schwenke [24].

To analyze the dependence of the inferred lithium abundance on the completeness of the line list used, we computed theoretical spectra using the line lists [13, 22, 23]. The list published in [13] is a modification of the CN and TiO line list [25]. Figure 5 shows the resulting synthetic spectra (in flux units) near the λ 670.8 nm lithium resonance doublet. This same figure shows the fluxes computed using the JOLA method. We note the following results:

(1) On the whole, the absorption-line intensities computed using the line lists of Plez [23] are somewhat higher than those based on the lists of Kurucz [22].

(2) The overall JOLA profile of the TiO molecular absorption bands is in better agreement with the line-by-line calculations based on Plez's list [23]. The local pseudocontinuum obtained using Plez's [23] lists is clearly defined and agrees fairly well with the JOLA pseudocontinuum (Fig. 5).

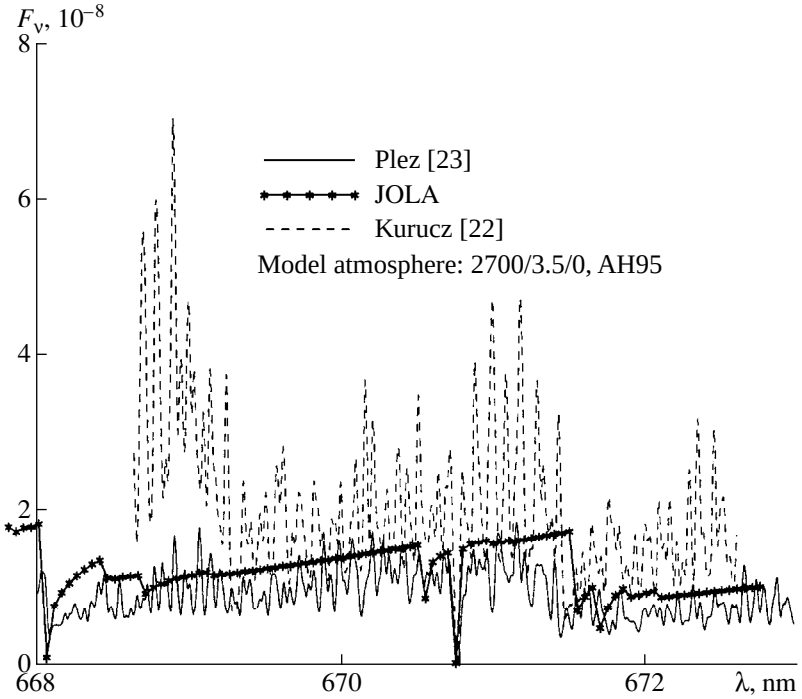

Fig. 5. Theoretical flux distributions near 670.8 nm computed using the line lists of [23], [22], and [25] with the JOLA opacity model, convolved with a Gaussian curve with Δ_g = 0.02 nm.

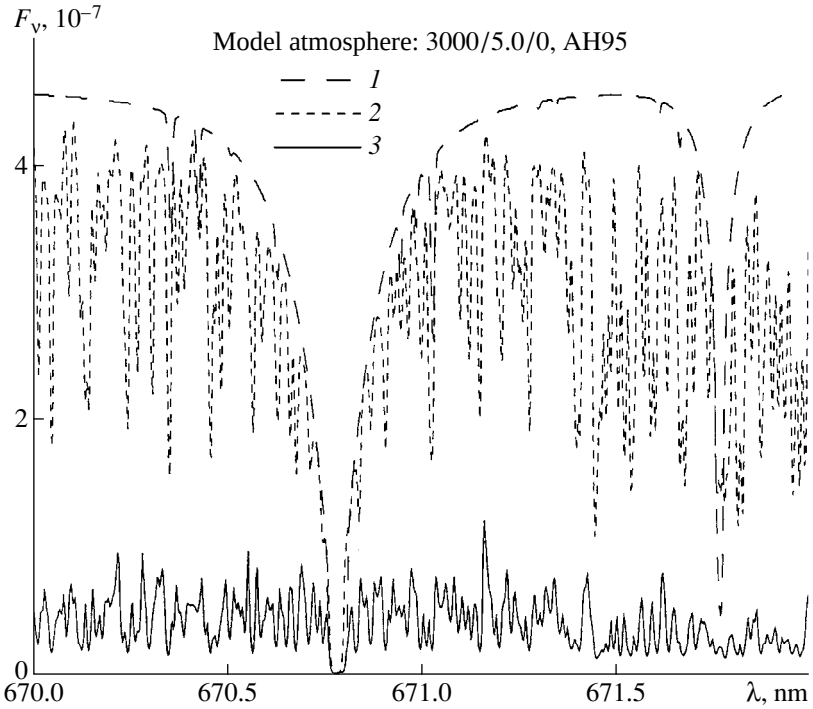

Fig. 6. Flux distributions near the λ 670.8 nm resonance doublet computed for model atmosphere 3000/5.0/0 using various line lists: (*1*) atomic lines only, (*2*) atomic + molecular lines from [25], and (*3*) atomic + molecular lines from [23].

(3) The line lists of [22] and [23] provide higher opacities near 670.8 nm than the line data used in [13] (see Fig. 6).

Figure 7 shows the result obtained in [13]. In this case, the observed lithium line intensities suggest $\log N(\mathrm{Li}) = 2.0$. At the same time, Plez's lists [23] imply a much higher lithium abundance: $\log N(\mathrm{Li}) = 3.2$. The LiI resonance lines in the spectrum of UX Tau C are saturated and are therefore only weakly sensitive to variations in the lithium abundance (Fig. 3). However, a 0.2-dex change of $\log N(\mathrm{Li})$ should be visible in the theoretical profile of the resonance doublet (Fig. 7). Taking into consideration all the factors influencing the inferred atmospheric lithium abundance for UX Tau C, we estimate the accuracy of the new $\log N(\mathrm{Li})$ value to be ±0.3 dex. Our analysis leads us to the following interesting conclusions:

(1) Both line lists [25] and [23] reproduce satisfactorily the profile of the (1–0) band of the TiO γ system in terms of the normalized fluxes. However, the two lists yield discrepant absolute fluxes at 670.8 nm.

(2) The "fine structure" of the spectra (determined by the strongest blends of molecular lines) is rather poorly reproduced. This could be a consequence of a number of factors: low signal-to-noise ratio, contamination of the spectrum by the spectra of other components of the triple system [14], and the effect of chromosphere-like features (see Section 4).

(3) The previous analysis [13] did not take into account the rotational broadening of the observed resonance doublet. It was assumed in that paper that the resonance-doublet lines were affected primarily by instrumental broadening with $\Delta_g = 0.06$ nm. Our new computations include the actual broadening due to the spectrograph ($\Delta_g = 0.03$ nm). The best fit to the observed doublet profile suggests a projected rotational velocity of $V^*\sin i = 35$ km/s for UX Tau C. This approach has allowed us to better reproduce the absorption profile of the Li I λ 670.8 nm doublet (Fig. 7). Note that, in their analysis of spectra obtained with the HIRES spectrograph on the KECK telescope, Basri and Marcy [26] found UX Tau C to have a rotation velocity of $V^*\sin i = 30 \pm 0.8$ km/s. However, we have reanalyzed the same observational data (kindly provided by G. Basri) using theoretical spectra computed using the lists of [23] and obtained a higher rotational velocity, $V^*\sin i = 35 \pm 1$ km/s, in agreement with the above results.

(4) Pavlenko *et al.* [13] computed synthetic spectra using the earlier model-atmosphere grid [15]. These model atmospheres were based on an incomplete set of opacity sources, and their outer layers are hotter than those of the model atmospheres [18]. However, our numerical computations indicate that this should have only a weak effect on the inferred atmospheric lithium abundance in UX Tau C. Our modeling of saturated lines of the λ 670.8 nm lithium doublet in the spectrum of UX Tau C using the model-atmosphere grids of [15]

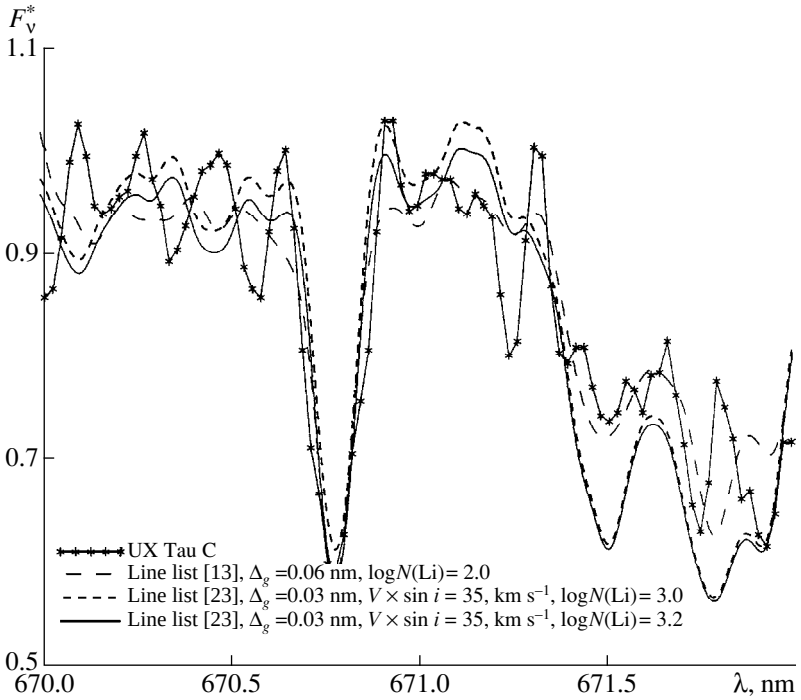

Fig. 7. Comparison of the observed profile of the lithium resonance doublet in the spectrum of UX Tau C with profiles computed using lists [13] and [23] with $\log N$ (Li) = 2.0 and $\log N$ (Li) = 3.0 and 3.2, respectively. Model atmosphere 3100/4.5/0.

and [18] gave virtually identical results, and the resulting $\log N$ (Li) values agree to within 0.1 dex.

4. RESULTS AND DISCUSSION

In this study, we have

(1) modeled the relative intensity variations of the lithium lines observed against a background of strong molecular bands in the spectra of late M dwarfs; and

(2) shown that the theoretical lithium line intensities depend on a number of parameters, including the model atmospheres adopted, their metallicities and gravities, and the completeness of the line lists used.

A number of factors reflect the importance of this work.

(1) Determining the effective temperatures and luminosities of late M dwarfs and brown-dwarf candidates is problematic. Uncertainties in $T_{\rm eff}$ and $\log g$ can reach several hundred degrees and ±0.5 dex [8]. Our conclusion that the lithium-line pseudoequivalent widths depend only weakly on $T_{\rm eff}$ (and somewhat more strongly on $\log g$) is of considerable interest for interpretions of the atmospheric lithium abundances of M dwarfs and brown-dwarf candidates. This is especially true in view of the fact that most Galactic brown dwarfs are evolving toward their "main sequence;" i.e., they are subgiants.

(2) Lithium lines in the spectra of M dwarfs with high atmospheric lithium abundances are saturated. Deriving lithium abundances from such lines is further complicated by the fact that only the cores of the lithium lines can be seen against a much stronger molecular-band background. Moreover, our computations showed that the "pseudoequivalent widths" w_λ^j of these lines depend strongly on the star's metallicity.

(3) The absolute theoretical fluxes depend appreciably on the completeness of the adopted molecular-line lists or systematic errors in the *gf* values for these lines. Inaccuracies in the line lists could be interpreted as opacity deficits in the vicinity of Li lines [27]. However, the use of refined—i.e., more exhaustive (with accurate λ and *gf*! values)—line lists provides a natural solution to this problem.

(4) We found UX Tau C, the low-mass component of the triple system, to have a lithium abundance $\log N$ (Li) = 3.2 ± 0.3; this result agrees rather well with the lithium abundances inferred for the other two components of the system. This supports the idea that components of the triple system have the same age. The underestimated atmospheric lithium abundances for UX Tau C obtained in previous studies were the result of the use of imperfect (incomplete) molecular-line lists.

(5) The new atmospheric lithium abundance for UX Tau C seems justified from a physical point of view but also (indirectly) testifies to the high quality of Plez's

[23] line lists. This is also evident from a comparison of the molecular-band strengths computed using the line-by-line and JOLA methods.

(6) Departures from LTE can play an important role in the formation of spectral lines in the atmospheres of late-type stars (see [2, 28]). At the same time, non-LTE effects are insignificant for saturated λ 670.8 nm lithium resonance doublet lines in the spectra of M dwarfs: Non-LTE corrections for these stars are comparatively small (≈0.1 dex) [13, 29].

(7) UX Tau is a young system. The powerful convective shells of young M dwarfs generate substantial energy fluxes in the form of various waves, which subsequently dissipate in the outermost atmospheric layers, producing temperature inversions. The active processes in pre-main-sequence stars show up in their spectra both in the form of H_α (Fig. 1) and other atomic line emission in the blue part of the spectrum and in the form of veiling effects [2]. Chromosphere-like structures (i.e., temperature inversions in the outer layers) can affect both lithium lines and the molecular lines making up the pseudocontinuum. However, it was shown in [13, 30, 31] that chromosphere-like structures in the atmospheres of late M dwarfs are more likely to appreciably affect molecular than lithium lines, although the cores of the lithium lines form in the outermost atmospheric layers. This should be borne in mind when comparing computed and observed molecular spectra near the lithium resonance doublet lines.

Recently, features in the spectra of late M dwarfs due to atmospheric dust condensation have been noted. As a result of the partial binding of Ti and V atoms in dust grains at low temperatures (T < 1500 K), the TiO and VO bands can weaken [32]m and even completely disappear [33, 34]. Note, however, that these effects begin to show up in the atmospheres of dwarf stars at temperatures $T_{\rm eff}$ < 2700 K [35] and are maximum at $T_{\rm eff}$ < 2000 K [36]. Therefore, we expect that such effects should not be important for the results discussed here. Unfortunately, our incomplete understanding of these effects makes it impossible to draw definite conclusions about their influence on our results.

5. ACKNOWLEDGMENTS

I am grateful to Drs. R. Rebolo, M. R. Zapatero-Osorio, and G. Basri for providing spectra and also to Drs. F. Allard and P. Houschildt for providing their model atmospheres.

REFERENCES

1. F. D'Antona and I. Mazitelli, Astrophys. J., Suppl. Ser. **90**, 467 (1994).
2. A. Magazzù, R. Rebolo, and Ya. V. Pavlenko, Astrophys. J. **392**, 159 (1992).
3. R. Rebolo, E. L. Martin, and A. Magazzù, Astrophys. J. Lett. **389**, L83 (1992).
4. A. Magazzù, E. L. Martin, and R. Rebolo, Astrophys. J. Lett. **404**, L17 (1993).
5. E. L. Martin, R. Rebolo, and M. R. Zapatero-Osorio, Astrophys. J. **469**, 706 (1996).
6. M. R. Zapatero-Osorio, R. Rebolo, E. L. Martin, *et al.*, Astrophys. J. **491**, L81 (1997).
7. R. Rebolo, E. L. Martin, and M. R. Zapatero-Osorio, *Low Mass Stars and Brown Dwarfs in Stellar Clusters and Associations* (in press).
8. R. Rebolo, G. Basri, G. Marcy, *et al.*, Astrophys. J. **469**, L53 (1996).
9. E. L. Martin, R. Rebolo, A. Magazzù, *et al.*, Astron. Astrophys. **282**, 503 (1994).
10. R. J. García López, R. Rebolo, and E. Martin, Astron. Astrophys. **282**, 518 (1994).
11. M. R. Zapatero-Osorio, E. L. Martin, and R. J. García López, Astron. Astrophys. **305**, 519 (1996).
12. B. R. Oppenheimer, G. Basri, T. Nakajima, *et al.*, Astron. J. **113**, 296 (1997).
13. Ya. V. Pavlenko, R. Rebolo, E. L. Martin, *et al.*, Astron. Astrophys. **308**, 807 (1995).
14. A. Magazzù, E. L. Martin, and R. Rebolo, Astron. Astrophys. **249**, 149 (1991).
15. F. Allard, Ph.D. Dissertation (Univ. Heidelberg, 1990).
16. F. Pozio, Mem. Soc. Astron. Ital. **62**, 171 (1991).
17. T. Tsuji, Astron. Astrophys. **23**, 411 (1973).
18. F. Allard and P. Hauschildt, Astrophys. J. **445**, 433 (1995).
19. Ya. V. Pavlenko, Astron. Astrophys. **253**, 43 (1997).
20. Ya. V. Pavlenko, Astron. Zh. **74**, 608 (1997).
21. G. W. Marcy, G. Basri, and J. R. Graham, Astrophys. J. Lett. **428**, L57 (1994).
22. R. L. Kurucz, CD ROM No. 15 (1993).
23. B. Plez, Astron. Astrophys. **337**, 495 (1998).
24. D. Schwenke, Faraday Discuss. **109**, 321 (1998).
25. C. Abia, H. M. J. Boffin, J. Isern, *et al.*, Astron. Astrophys. **272**, 455 (1993).
26. G. Basri and G. W. Marcy, Astron. J. **109**, 762 (1995).
27. B. Plez, V. V. Smith, and L. L. Lambert, Astrophys. J. **418**, 812 (1993).
28. H. Steenbock and H. Holweger, Astron. Astrophys. **130**, 319 (1984).
29. Ya. V. Pavlenko and A. Magazzù, Astron. Astrophys. **311**, 961 (1996).
30. E. R. Houdebine and J. G. Doyle, Astron. Astrophys. **302**, 861 (1995).
31. Ya. V. Pavlenko, Astron. Zh. **75**, 567 (1998).
32. H. R. A. Jones and T. Tsuji, Astrophys. J. Lett. **480**, L39 (1997).
33. Ya. V. Pavlenko, Astron. Zh. **75**, 888 (1998).
34. C. G. Tinney, X. Delfosse, T. Forveille, *et al.*, Astron. Astrophys. **338**, 1066 (1998).
35. T. Tsuji, K. Ohnaka, and W. Aoki, Astron. Astrophys. **305**, L1 (1996).
36. Ya. V. Pavlenko, M. R. Zapatero-Osorio, and R. Rebolo, *Low Mass Stars and Brown Dwarfs in Stellar Clusters and Associations* (in press).

Translated by A. Dambis

Astronomy Reports, Vol. 44, No. 4, 2000, pp. 227–234. Translated from Astronomicheskiĭ Zhurnal, Vol. 77, No. 4, 2000, pp. 264–272.

Abundances of C, N, O, and Other Elements in the Atmospheres of the δ Scuti Variables 14 Aur, δ Sct, and HD 127986

T. M. Rachkovskaya

Crimean Astrophysical Observatory, Nauchny, Crimea, 334413 Ukraine

Received December 25, 1998

Abstract—Using high-resolution spectra, we have determined the abundances of carbon ($\log\varepsilon$ (C)), nitrogen ($\log\varepsilon$ (N)), oxygen ($\log\varepsilon$ (O)), silicon ($\log\varepsilon$ (Si)), sulphur ($\log\varepsilon$ (S)), and some other elements for three δ Scuti stars. $\log\varepsilon$(C) for all three stars and $\log\varepsilon$ (N) for δ Sct and HD 127986 are close to the solar values, while there appears to be a slight (0.15 dex) nitrogen deficiency for 14 Aur. The $\log\varepsilon$ (O) values correspond to a 0.30-dex deficiency for 14 Aur and δ Sct and a 0.20-dex deficiency for HD 127986. The values of $\log\varepsilon$ (Si) for the three stars are close to solar, and the $\log\varepsilon$ (S) values indicate a slight deficiency (0.10 dex) for 14 Aur and HD 127986 and a 0.20-dex excess for δ Sct. Comparison of the elemental abundances for seven δ Scuti stars with those for Am stars shows that the mean deficiencies of C, N, and O are smaller for pulsating δ Scuti stars than for Am stars with similar effective temperatures. The sulphur abundances are virtually the same for both types of stars. © *2000 MAIK "Nauka/Interperiodica".*

1. INTRODUCTION

Observations accumulated over many years provide evidence that the physical processes occurring in stars strongly influence their chemical abundances. For example, it is now generally believed that the anomalous abundances in classical Am stars result from diffusion in their atmospheres. The atmospheres of δ Scuti variables, which undergo pulsational instability and have moderate metal abundance anomalies compared to classical Am stars, apparently possess some special physical conditions that make it possible for diffusion and pulsation to coexist. We are unaware of any plausible theory that can explain this. It is thus necessary to obtain homogeneous observations, in particular, measurements of elemental abundances in the atmospheres of δ Scuti stars. We have published a number of papers concerned with this problem.

Our determinations of the atmospheric abundances for eight pulsating δ Scuti stars are presented in [1]. This analysis was based on photographic spectra at 3800–6000 Å, with reciprocal dispersions of 4 and 6 Å/mm. All the studied objects had more or less anomalous abundances compared with the Sun. We used the abundance anomalies to tentatively subdivide the eight δ Scuti stars into two groups:

(1) Stars with enhanced abundances of some or all elements (we do not consider C, N, and O here): 14 Aur (T_{eff} = 8000 K, $\log g$ = 3.8), 28 And (T_{eff} = 7900 K, $\log g$ = 4.1), 20 CVn (T_{eff} = 7650 K, $\log g$ = 3.7), and δ Sct (T_{eff} = 7000 K, $\log g$ = 3.1). We especially note 20 CVn, which displayed 0.5–1.5 dex excesses (relative to solar values) for all observed elements from Na to Gd.

(2) Stars whose abundances depend on atomic number qualitatively in the same way as classical Am stars: δ Del (T_{eff} = 7400 K, $\log g$ = 3.7), 44 Tau (T_{eff} = 7100 K, $\log g$ = 3.8), V644 Her (T_{eff} = 7050 K, $\log g$ = 3.8), and HD 127986 (T_{eff} = 6150 K, $\log g$ = 3.3).

Three of these stars (14 Aur, V644 Her, and δ Del) are believed to be binaries; therefore, in both [1] and the observations described below, we paid special attention to searches for possible spectroscopic manifestations of a companion. However, as in earlier studies, we did not detect lines from companions in the spectra of 14 Aur or V644 Her. For the δ Del system, our CCD observations confirmed the detections of the companion's spectral lines reported by Duncan and Preston [2] and Smith [3]; the spectrum showed a very complex pattern that changed with the phase of the orbital period. For this reason, analysis of the δ Del binary system requires a special methodical approach. We do not adopt such an approach here, and the results obtained in [4] should be taken to reflect the mean characteristics of the system's two components.

Later, when we were able to obtain high-resolution, spectroscopic CCD observations, we continued observations of our program stars in order to determine the abundances of the elements most significant from the point of view of stellar evolution, namely, carbon, nitrogen, and oxygen (C, N, O), which we did not study

1063-7729/00/4404-0227$20.00 © 2000 MAIK "Nauka/Interperiodica"

Table 1. Data on the program stars

Star	HD	HR	$v\sin i$, km/s	m_v	Δm_v	Pulsation period	Pulsation type
14 Aur	33959	1706	20	5.1	0.08	$0^d.088$	Nonradial
δ Sct	172748	7020	32	4.9	0.29	0.194	Radial + nonradial
	127986	5451	5	6.4	0.02	0.140	Radial

earlier due to either strong blending or the absence of lines in the observed spectral range. We have published results of CCD studies of the C, N, and O abundances for four stars in [5–8]: 28 And, 44 Tau, V644 Her, and 20 CVn. Here, we present results for three more stars: 14 Aur, δ Sct, and HD 127986. Some parameters of these stars are summarized in Table 1. The rotation velocities are from the catalog of Uesugi and Fukuda [9], and the other parameters are taken from [10].

Due to our special interest in C, N, and O, we centered the observed spectral ranges on lines of these elements: CI λ 5052, NI λ 8683, and OI λ 6156. These ranges also contained lines of other elements, whose abundances we also analyzed. In particular, we have obtained the first determinations of the silicon and sulphur abundances for the program stars.

2. OBSERVATIONAL MATERIAL

Our observations were obtained on the 2.6 m reflector of the Crimean Astrophysical Observatory, in 1991–1993 equipped with a St. Petersburg-made 580×520 CCD, in 1994 with a British-made 600×380 GEC CCD, and in 1996 with an American-made 1024×256 EEV15–11 CCD. The detectors were mounted at the Coudé focus. The second order of the diffraction grating was used. The reciprocal dispersion was 3 Å/mm, and the spectral resolution was 30 000. In 1991–1994 and 1996, the simultaneously recorded spectra covered 30 and 60 Å, respectively. As a rule, we took several exposures of the same spectral region in a night and then added them. An individual exposure was 40–60 minutes, depending on the spectral region and weather. The signal-to-noise ratios were usually S/N = 80–150, with rare exceptions.

We reduced the spectra using standard techniques: subtraction of the dark current, flat-fielding, removal of cosmic-rays from the spectra, correction for the sky background, and normalization to the continuum. This resulted in the line profiles and equivalent widths used in the subsequent analysis.

3. EQUIVALENT WIDTHS. OSCILLATOR STRENGTHS

The first three columns of Table 2 contain the wavelengths of the studied lines, excitation potentials of the lower levels, and oscillator strengths $\log gf$. To ensure accurate comparisons of our results for the three stars studied here with those investigated earlier, we used the same $\log gf$ values as in [5–8], though new $\log gf$ values for the lines of some elements have appeared since then. The three next columns of the Table give the equivalent widths W_λ for each of the program stars. It is apparent from Table 3 that, due to the lower rotational velocity of HD 127986 compared to 14 Aur and δ Sct (Table 1), we were able to observe a much larger number of unblended lines for this star.

4. CHEMICAL ABUNDANCES

We estimated the elemental abundances $\log\varepsilon$ (El) in the atmospheres of 14 Aur, δ Sct, and HD 127986 using the models (Table 3) computed by us earlier [1]. All our calculations assumed LTE. We used equivalent widths to estimate $\log\varepsilon$ (El) if they could be reliably calculated; if not, we used synthetic spectra. It follows from [5, 6] that the computed synthetic spectra are in good agreement with the observations in the spectral intervals under consideration. This is illustrated by Fig. 1, which shows the most blended of the spectral intervals, 6153.5–6158.5 Å, for δ Sct and HD 127986, which have different rotational velocities (the spectra are offset along the intensity axis, r_λ). The three last columns of Table 2 contain our $\log\varepsilon$ (El) values determined from individual lines; the asterisks mark $\log\varepsilon$ values based on synthetic spectra. For the final calculations of the synthetic spectra, we adopted $v\sin i$ = 20 km/s for 14 Aur, 25 km/s for δ Sct, and 5 km/s for HD 127986; thus, we have refined the rotational velocity for δ Sct and confirmed the previously known estimates for 14 Aur and HD 127986 (Table 1). The mean abundances are presented in Table 4. The errors of a single $\log\varepsilon$ determination are 0.05–0.25. Table 4 also contains the solar abundances in our system of oscillator strengths according to Lyubimkov and Savanov [11] and, for comparison, the most recent data from Grevesse and Noels [12]. There are slight discrepancies between [11] and [12] for some elements. Note that, in our estimates of the C, N, and O abundances, we have used the same lines here and in [5–8]. This is also the case for the other elements, with rare exceptions.

Let us now consider our results for individual elements, first and foremost, C, N, and O.

Carbon. We derived the carbon abundance $\log\varepsilon$ (C) from the CI λ 5052.12 lines, which are blended with the

Table 2. List of spectral lines studied

Element λ, Å	χ, eV	log*gf*	W_λ, mÅ			logε		
			14 Aur	δ Sct	HD 127986	14 Aur	δ Sct	HD 127986
C I								
5052.17	7.68	−1.40			72	8.60*	8.58*	8.67
N I								
8680.28	10.34	+0.40				7.80*	7.95*	7.70*
8683.40	10.33	+0.14	80	59	13	7.85	7.94	7.65
8686.15	10.33	−0.27		43	15	7.90*	8.10*	8.50*
O I								
6155.98	10.74	−0.66			9	8.70*	8.70*	8.91
6156.76	10.74	−0.41			9	8.40*	8.50*	8.69
6158.18	10.69	−0.26			10	8.55*	8.50*	8.61
7771.94	9.15	+0.35	300	255	132	9.00	8.80	8.64
7774.17	9.15	+0.21			106	8.70*	8.90*	8.56
7775.40	9.15	−0.02			92			8.58
Na I								
6154.23	2.10	−1.57	7	10	27	6.10	6.05	6.17
6160.75	2.10	−1.26			38			6.13
Si I								
6142.50	5.62	−1.56	10		31	7.39		7.51
6145.02	5.61	−1.48	14	26	32	7.46	7.60	7.45
6155.13	5.62	−0.84	63		76	7.55*		7.34
8686.35	6.21	−1.20				7.35*	7.40*	7.80
Si II								
5055.98	10.07	+0.52	81		49	7.58	7.48*	7.91
S I								
8670.18	7.87	−0.89			16			7.20
8670.59	7.87	−0.53			16			6.85
8671.28	7.87	−0.64			11			6.77
8678.93	7.87	−1.00						
8679.62	7.87	−0.41			40	7.10*	7.30*	7.35
8680.41	7.87	−0.27						7.00*
8693.14	7.87	−1.37			8			7.43
8693.93	7.87	−0.52			18	7.10*	7.30*	6.88
8694.63	7.87	+0.05			57			7.07
Ca I								
6161.30	2.52	−1.27			48			6.27
6162.17	1.90	−0.09	146	202	167	5.87	6.06	5.76
6166.44	2.52	−1.14	17	38	59	6.10	6.24	6.20
6169.05	2.52	−0.80			86	6.05*	6.15*	6.03
6169.56	2.53	−0.27			93			5.93
Ti I								
5039.96	0.02	−1.13			64			4.81
5043.59	0.89	−1.73			18			5.32
8675.37	1.07	−1.67			8			5.33

Table 2. (Contd.)

Element λ, Å	χ, eV	log*gf*	W_λ, mÅ			logε		
			14 Aur	δ Sct	HD 127986	14 Aur	δ Sct	HD 127986
FeI								
5044.21	2.85	–2.31			68			7.38
5049.82	2.28	–1.46			133			6.84
5051.63	0.92	–2.80			136	7.55*	7.30*	6.88
5054.64	3.64	–2.20			23			7.36
6151.62	2.18	–3.30	8	8	28	7.58	7.23	7.18
6157.73	4.08	–1.25	8		46	7.50*	7.50*	7.17
6165.36	4.14	–1.32	9	19	31	7.16	7.23	7.06
6170.50	4.80	–0.65			60			7.42
7780.58	4.45	–0.27	65	86	95	7.29	7.26	7.00
8671.85	5.02				11			7.20
FeII								
6147.74	3.87	–3.00	80	113	83	7.53	7.53	7.51
6149.26	3.87	–2.88	73	111	66	7.34	7.40	7.20

* Element abundance derived using the synthetic spectrum.

FeI λ 5051.64 lines for 14 Aur and δ Sct, so that we had to use synthetic spectra to determine $\log\varepsilon$(C) for these stars. Keeping in mind that the accuracy of our estimates is 0.2 dex, all three stars have carbon abundances close to the solar value: $\log\varepsilon$(C) = 8.60, 8.58, and 8.67 for 14 Aur, δ Sct, and HD 127986 (Table 4).

Nitrogen. We used three lines to estimate the nitrogen abundances $\log\varepsilon$(N): NI λ 8680.28, λ 8686.15, and λ 8683.40. The λ 8680.28 and λ 8686.15 lines were blended with lines of sulphur, SI λ 8680.41, and of silicon, SiI λ 8686.35; in these cases, we determined the nitrogen, sulphur, and silicon abundances using synthetic spectra (Table 3). The equivalent widths of the λ 8683.40 line were calculated reliably for all three stars and then used to derive $\log\varepsilon$(N) (Table 2). Table 2 shows that the $\log\varepsilon$(N) values for 14 Aur and δ Sct were nearly the same for all three lines, whereas, for HD 127986, the λ 8686.15 line yields a nitrogen abundance that is too high. The reason for this is not clear. Our final nitrogen-abundance determinations for 14 Aur, δ Sct, and HD 127986 were $\log\varepsilon$(N) = 7.85, 8.0, and 7.95, respectively. All these are close to the solar nitrogen abundance.

Table 3. Atmospheric parameters

Star	$T_{\rm eff}$, K	log*g*	ξ_t, km/s
14 Aur	8000	3.8	5.4
δ Sct	7000	3.1	5.4
HD 127986	6150	3.3	3.8

Oxygen. To determine the oxygen abundances $\log\varepsilon$(O), we observed the λ 6156 (6155.96, 6155.97, 6155.99), λ 6157 (6156.74, 6156.76, 6156.78) and λ 6158 (6158.15, 6158.17) OI triplets, as well as λ 7771.94, λ 7774.17, and λ 7775.39. For all three program stars, we computed synthetic spectra for the wavelength range 6153.5–6159 Å and compared them with the observed spectra (Fig. 1) in order to estimate the abundances of oxygen and of other elements in this spectral interval (Table 2). For HD 127986, we also calculated $\log\varepsilon$(O) using the line equivalents widths; the results were in good agreement with the values derived from the synthetic spectra.

The λ 7771–7775 infrared triplet requires a separate treatment. In A stars, these lines show considerable deviations from LTE. Recall that, in Table 2, the $\log\varepsilon$(OI 7771–7775) values, like all the $\log\varepsilon$(El) values, were derived assuming LTE. However, all the other $\log\varepsilon$(El) determinations are based on relatively weak lines (the equivalent widths slightly exceed 100 mÅ only for the FeII lines and one CaI line), which are not very sensitive to possible uncertainties in the microturbulence velocities adopted in the calculations. Baschek *et al.* [13] showed that the proportionality coefficient relating the line equivalent widths calculated in LTE and non-LTE assumptions increases drastically when the star's temperature or the line's equivalent width increases. Using calculations presented in [13], we interpolated corrections to $\log\varepsilon$(O) as functions of the effective temperature T_{eff}, gravity log*g*, and microturbulence velocity ξ_t. In this way, we obtained the correc-

tions for the infrared triplet lines of –0.30 dex for 14 Aur and δ Sct and –0.15 dex for HD 127986. The corresponding corrections for the λ 6156–6158 lines do not exceed –0.1 dex for any of the three stars. Introducing these corrections brings the oxygen abundances for 14 Aur and δ Sct derived from the infrared triplet closer to the values calculated using the λ 6156–6158 lines. This correction procedure is obviously only approximate, and we did not use the λ 7771–7775 lines when deriving the mean abundances for 14 Aur ($\log\varepsilon(O) = 8.55$) and δ Sct ($\log\varepsilon(O) = 8.57$). We included the infrared triplet when deriving our final value for HD 127986, $\log\varepsilon(O) = 8.66$, because use of a non-LTE analysis for the λ 7771–7775 lines does not introduce significant errors for stars with effective temperatures around 6000 K. Table 4 shows that, for each of the three stars, there is evidence for a slight oxygen deficiency (0.2 dex).

Let us now consider several other elements.

Silicon. We could not find any data on silicon abundances in the atmospheres of 14 Aur, δ Sct, and HD 127986 in the literature. To estimate $\log\varepsilon(Si)$, we used the four SiI lines λ 6142.53 (not observed for δ Sct), λ 6145.08, λ 6155.22, and λ 8686.35 and one SiII line, λ 5055.98. We can see from Table 3 that the agreement between the $\log\varepsilon(Si)$ values derived from individual SiI and SiII lines (except SiI λ 8686.35 and SiII for HD 127986) is fairly good; on average, the values derived from the SiI lines suggest a slight abundance deficiency for each of the three stars: $\log\varepsilon(Si) = 7.14$ (14 Aur), $\log\varepsilon(Si) = 7.50$ (δ Sct), and $\log\varepsilon(Si) = 7.52$ (HD 127986). However, the SiII line gives close to solar $\log\varepsilon(Si)$ values for 14 Aur and δ Sct and a somewhat higher value for HD 127986. Generally speaking, this line should be used with caution, since it is blended with the λ 5055.99 FeI line.

Sulphur. As noted above, we derived the sulphur abundances for these three stars for the first time. Our observed spectral ranges contain nine neutral sulphur (SI) lines (Table 2). For HD 127986, the sulphur abundance calculated using the equivalent widths of seven unblended lines, $\log\varepsilon(S) = 7.07$, is 0.13 dex lower than the solar value (Table 4). For the other two stars, the synthetic-spectrum calculations yield abundances $\log\varepsilon(S) = 7.10$ (14 Aur) and $\log\varepsilon(S) = 7.30$ (δ Sct), which are 0.10 and 0.20 dex lower than the solar value (Table 4). Note that the sulphur abundances for the four δ Scuti stars we studied earlier were in the range $\log\varepsilon(S) = 7.02$–$7.33$. Studies of Am stars (e.g., by Smith [14, 15], Adelman [16], Savanov [17]) have shown that both sulphur deficiencies and excesses can be present in these stars. Thus, we see that the sulphur abundances for our program δ Sct stars do not differ from those for Am stars as a whole.

We also estimated the abundances of sodium, calcium, iron, and titanium for the program stars using the CCD observations (titanium lines were observed only for HD 127986). Our final $\log\varepsilon$ values for these elements are collected in Table 4, which also contains abundances derived from our photographic observations [1]. The number of lines used for each $\log\varepsilon$ determination is indicated in parentheses. It is apparent from Table 4 that our new values for some elements disagree with earlier estimates. Let us discuss some (probably not the only) reasons for this disagreement. One possibility is that, along with fairly weak lines, some lines stronger than those considered by us (100 mÅ < W_λ < 200 mÅ) were used for the abundance determinations in [18–20] (this applies to all the elements listed above). A second reason could be the unequal numbers of lines used in the different studies. Finally, some of the disagreement could be due to uncertainties in the adopted oscillator strengths.

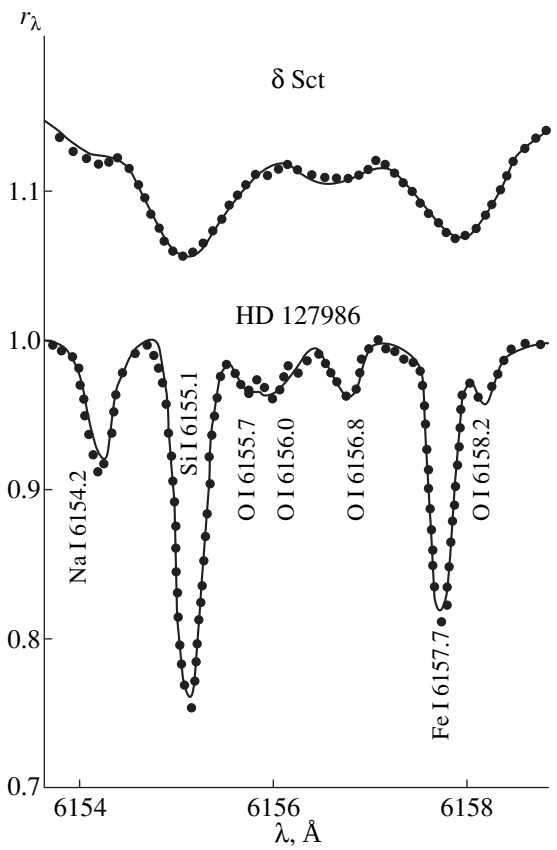

Fig. 1. Comparison of observed (dots) and synthetic (solid curves) spectra at 6153.5–6158.5 Å for δ Sct ($v\sin i = 25$ km/s) and HD 127986 ($v\sin i = 5$ km/s).

With these factors in mind, let us briefly discuss Na, Ca, and Fe.

Sodium. If we give preference to the CCD observations (for 14 Aur, we have only CCD observations of sodium lines), there is evidence for slight sodium deficiencies $\log\varepsilon(Na)$ in each of the three program stars. However, the photographic observations sug-

Table 4. Atmospheric element abundances

Element	$\log\varepsilon$						$\log\varepsilon_\odot$	
	14 Aur		δ Sct		HD 127986		[11]	[12]
	this paper	[1]	this paper	[1]	this paper	[1]		
C I	8.60(1)		8.58(1)		8.67(1)		8.60	8.55
N I	7.85(3)		8.00(3)		7.95(3)		8.00	7.97
O I	8.55(3)		8.57(3)		8.66(6)		8.86	8.87
Na I	6.10(1)		6.05(1)	6.84(2)	6.15(2)	6.49(2)	6.28	6.33
Si I	7.44(4)		7.50(2)		7.52(4)		7.65	7.55
Si II	7.58(1)		7.48(1)		7.91(1)		7.55	
S I	7.10(6)		7.30(5)		7.07(8)		7.20	7.33
Ca I	6.00(4)	6.48(6)	6.15(4)	6.43(4)	6.04(5)	6.04(6)	6.36	6.36
Ti I					5.15(3)	4.38(1)	4.86	5.02
Fe I	7.35(5)	7.58(35)	7.30(5)	7.59(30)	7.15(10)	7.32(24)	7.55	7.50
Fe II	7.30(2)	7.51(13)	7.46(2)	7.54(9)	7.36(2)	7.28(9)	7.56	

gest small excesses of this element in δ Sct and HD 127986 (Table 4). New studies of sodium lines are required to resolve this contradiction.

Calcium. It is apparent from Table 4 that the calcium abundances for HD 127986 derived from CCD and photographic observations are the same, whereas, in the case of 14 Aur and δ Sct, the deficiencies of $\log\varepsilon$ (Ca) indicated by the CCD observations are smaller (for these two stars, we adopted the average $\log\varepsilon$ (Ca) values derived from the CCD and photographic observations).

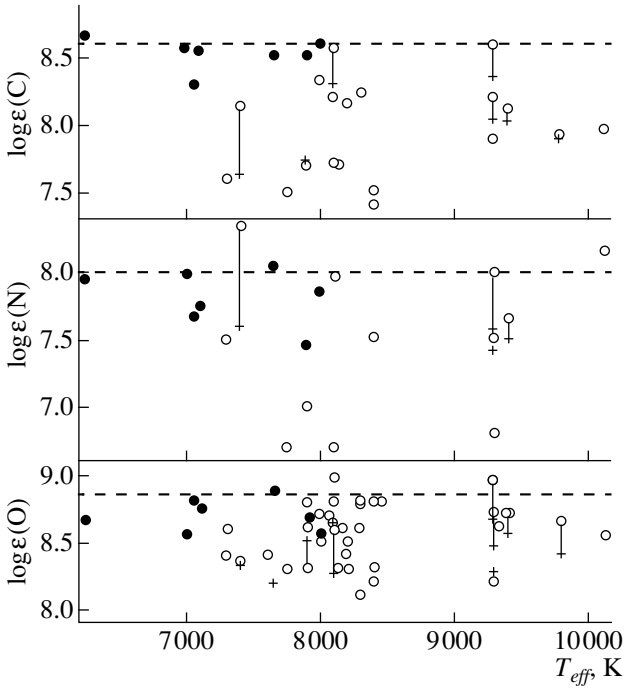

Fig. 2. Comparison of the carbon, nitrogen, and oxygen abundances of δ Scuti stars (present paper and [5–8]—solid circles) and Am stars ([17]—open circles; [21]—crosses) as functions of the effective temperature. The thin vertical lines connect data points for the same star. The dashed horizontal lines represent solar element abundances according to [11].

Iron. We adopted the mean iron abundances from the CCD and photographic observations: for 14 Aur, $\log\varepsilon$ (Fe) = 7.55 from neutral iron (FeI) lines and $\log\varepsilon$ (Fe) = 7.48 from ionized iron (FeII) lines; for δ Sct, $\log\varepsilon$ (Fe) = 7.55 (FeI) and $\log\varepsilon$ (Fe) = 7.52 (FeII); for HD 127986, $\log\varepsilon$ (Fe) = 7.27 (FeI) and $\log\varepsilon$ (Fe) = 7.29 (FeII). The iron abundances in the atmospheres of 14 Aur and δ Sct are close to the solar value, while the iron abundance for HD 127986 is approximately 0.27 dex lower.

5. DISCUSSION

Figures 2 and 3 compare the abundances of CNO and of Si and S for the seven δ Sct objects studied by us in the present paper and in [5–8] with the abundances of these same elements for Am stars [17, 21] as functions of the effective temperature. Note that our results and the results of Savanov [17, 21] are based on observations obtained on the same instruments analyzed using the same techniques. In addition, the estimates of the CNO and Si, S abundances were obtained using the same system of oscillator strengths in the present paper and in [21]. In [17], Savanov used more recent values of the oscillator strengths $\log gf$. Analysis of Figs. 2 and 3 leads to the following conclusions.

The carbon abundances $\log\varepsilon$ (C) for six of the δ Scuti stars are close to solar, and only for V644 Her is there a

slight deficiency of $\log\varepsilon$(C) (T_{eff} = 7050 K). Figure 2 shows that all the δ Scuti stars are located towards the upper envelope of the $\log\varepsilon$(C) values for Am stars with similar temperatures.

Figure 2 also shows that HD 127986 (T_{eff} = 6150 K), δ Sct (T_{eff} = 7000 K), 20 CVn (T_{eff} =7650 K), and 14 And (T_{eff} = 8000 K) have close to solar nitrogen abundances $\log\varepsilon$(N), whereas the remaining stars—V644 Her (T_{eff} = 7050 K), 44 Tau (T_{eff} = 7100 K), and 28 And (T_{eff} = 7900 K)—exhibit nitrogen deficiencies. Despite the large scatter in the abundances, Fig. 2 suggests that, on average, the nitrogen deficiencies for the seven δ Scuti stars are smaller than for the Am stars.

The oxygen abundances $\log\varepsilon$(O) for V644 Her, 44 Tau, and 20 CVn probably do not differ from the solar value, whereas HD 127986, δ Sct, 28 And, and 14 Aur exhibit small oxygen deficiencies of 0.25 dex, on average. As in the case of carbon and nitrogen, the oxygen deficiencies for δ Scuti stars are, on average, smaller than those for Am stars. Note that our conclusions about the carbon abundances are more certain due to the better statistics for the Am-star observations.

Let us consider separately 20 CVn, which was most intensely observed. The results of our CNO studies for this star are published in [8]. In the most recent study we are aware of, Takeda and Sadakane [22] estimated the CNO abundances in a non-LTE approximation, and obtained $\log\varepsilon$(C) = 8.7, $\log\varepsilon$(N) = 8.0, $\log\varepsilon$(O) = 9.0; our determinations [8], assuming LTE, yielded 8.5, 8.05, and 8.9—i.e., very similar values for nitrogen and oxygen. We find the largest deviation, 0.2 dex, for carbon, possibly because we studied the CI λ 5052 line, while Takeda and Sadakane [22] considered infrared CI lines in the range 9061–9111 Å. Thus, overall, our results on the CNO abundances in 20 CVn confirm those from [22].

Figure 3 compares the silicon and sulphur abundances $\log\varepsilon$(Si) and $\log\varepsilon$(S) for δ Scuti stars with those for Am stars [17]. It is apparent that these stars can show either deficiencies or excesses of these elements relative to the solar values. Our sulphur abundance for 20 CVn, $\log\varepsilon$(S) = 7.30, is 0.2 dex below that from [22], though the same lines were analyzed in both studies. Finally, numerous studies of normal, mercury–manganese, and Am stars and δ Scuti variables ([5–8, 14–17, 23–24] and the present paper) indicate that none of these groups of stars differs from the others in its characteristic silicon abundance in a statistically significant sense.

6. CONCLUSION

Let us summarize the main results of our study of the δ Scuti stars 14 Aur, δ Sct, and HD 127986.

The carbon abundances $\log\varepsilon$(C) for all three stars and the nitrogen abundances $\log\varepsilon$(N) for δ Sct and HD 127986 are close to the solar values: There is evidence for a slight (0.15 dex) nitrogen deficiency for 14 Aur.

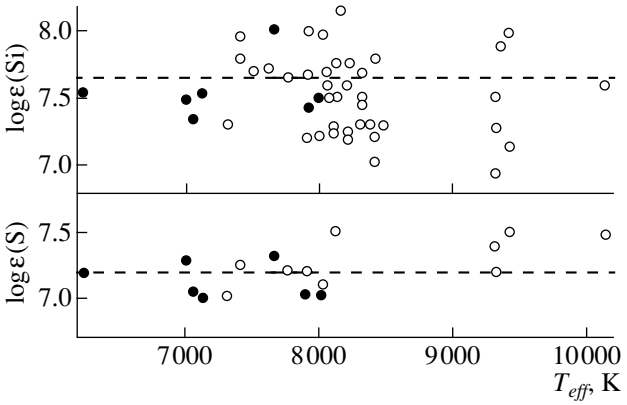

Fig. 3. Silicon and sulphur abundances for δ Scuti stars (present paper and [5–8]—filled circles) and for Am stars ([17]—open circles) as functions of the effective temperature. Solar abundances are shown as in Fig. 2.

The $\log\varepsilon$(O) values indicate oxygen deficiencies of 0.3 dex for 14 Aur and δ Sct and 0.20 dex for HD 127986.

The silicon abundances $\log\varepsilon$(Si) for the three stars are close to solar, and the sulphur abundances $\log\varepsilon$(S) indicate a slight deficiency (0.10 dex) for 14 Aur and HD 127986 and an excess (0.20 dex) for δ Sct.

A comparison of the abundances for the seven δ Scuti stars studied in this paper and in [5–8] with those for Am stars studied in [17, 21] shows that the observed mean deficiencies of carbon, nitrogen, and oxygen for the δ Scuti stars are significantly smaller than those for Am stars with similar effective temperatures T_{eff}. The silicon and sulphur abundances are virtually the same for both types of stars.

REFERENCES

1. T. M. Rachkovskaya, Izv. Krym. Astrofiz. Obs. **80**, 3 (1988).
2. D. K. Duncan and G. W. Preston, Bull. Am. Astron. Soc. **11**, 728 (1979).
3. M. A. Smith, Astrophys. J. **254**, 242 (1982).
4. L. S. Lyubimkov and T. M. Rachkovskaya, Izv. Krym. Astrofiz. Obs. **71**, 127 (1985).
5. T. M. Rachkovskaya, Izv. Krym. Astrofiz. Obs. **87**, 68 (1993).
6. T. M. Rachkovskaya, Izv. Krym. Astrofiz. Obs. **88**, 3 (1993).
7. T. M. Rachkovskaya, Izv. Krym. Astrofiz. Obs. **90**, 162 (1995).
8. T. M. Rachkovskaya, Astron. Zh. **71**, 638 (1994).
9. A. Uesugi and J. Fukuda, *Revised Catalogue of Stellar Rotational Velocities* (Department of Astronomy, Kyoto Univ., Kyoto, 1982).
10. M. Breger, Publ. Astron. Soc. Pac. **91**, 5 (1979).

11. L. S. Lyubimkov and I. S. Savanov, Izv. Krym. Astrofiz. Obs. **69**, 50 (1984).
12. N. Grevesse and A. Noels, ASP Conf. Ser. **99**, 118 (1996).
13. B. Baschek, M. Sholz, and E. Sedlmayr, Astron. Astrophys. **55**, 375 (1977).
14. M. A. Smith, Astron. Astrophys. **11**, 325 (1971).
15. M. A. Smith, Astron. Astrophys. **189**, 101 (1974).
16. S. J. Adelman, Mon. Not. R. Astron. Soc. **266**, 97 (1994).
17. I. S. Savanov, Doctoral Dissertation in Mathematical Physics (S.-Peterburg, 1998).
18. T. M. Rachkovskaya, Izv. Krym. Astrofiz. Obs. **78**, 22 (1988).
19. T. M. Rachkovskaya, Izv. Krym. Astrofiz. Obs. **75**, 149 (1986).
20. T. M. Rachkovskaya, Izv. Krym. Astrofiz. Obs. **76**, 3 (1987).
21. I. S. Savanov, *Proceedings of International Meeting on the Physics and Evolution of Stars* (Nauka, Leningrad, 1988).
22. Y. Takeda and K. Sadakane, Publ. Astron. Soc. Jpn. **49**, 367 (1977).
23. S. J. Adelman, Mon. Not. R. Astron. Soc. **230**, 671 (1988).
24. S. J. Adelman, Mon. Not. R. Astron. Soc. **252**, 116 (1991).

Translated by N. Samus'

Astronomy Reports, Vol. 44, No. 4, 2000, pp. 235–245. Translated from Astronomicheskiĭ Zhurnal, Vol. 77, No. 4, 2000, pp. 273–284.

Quantitative Analysis of the Spectrum of the Magnetic roAp Star HD 83368 with "Lithium" Spots

A. V. Shavrina[1], N. S. Polosukhina[2], V. Tsymbal[3], and V. Khalak[1]

[1]*Main Astronomical Observatory of the Ukrainian National Academy of Sciences, Kiev, Ukraine*

[2]*Crimean Astrophysical Observatory, Nauchny, Crimea, Ukraine*

[3]*Simferopol' State University, Simferopol', Ukraine*

Received April 9, 1999

Abstract—Preliminary results of a synthetic-spectrum analysis of the elemental abundances in the atmosphere of the "spotted" roAp star HD 83368 are presented. The positions of two lithium spots on the star's surface are determined using an imaging technique based on the Doppler shifts for various rotation phases. © *2000 MAIK "Nauka/Interperiodica".*

1. INTRODUCTION

Any information about the abundances of lithium in stellar atmospheres is very important for theories of the internal structure and evolution of stars. A normal star that initially possesses an appreciable amount of lithium loses it in the course of its evolution due to various mixing mechanisms, since lithium is easily destroyed at the high temperatures characteristic of stellar interiors. The presence of lithium features in a stellar spectrum provides evidence that there is little or no circulation of material between the cool, outer layers and hot, inner layers of the star's atmosphere. Interpreting the observed lithium abundances in stellar atmospheres is one of the puzzles of modern astrophysics: The physical processes giving rise to the large range of this element's abundance in stars with similar physical parameters are not clear. Accumulating spectroscopic observations of Li lines is a prerequisite for a deeper understanding of this problem. With the advent of new technical possibilities for observing Li lines in stellar spectra, interest in the lithium problem has grown considerably. High-resolution échelle spectrographs, CCD cameras with high signal-to-noise ratios, and modern techniques for the analysis of spectroscopic material (model-atmosphere and synthetic-spectra methods and use of improved atomic data, especially for rare earth elements) enable detailed investigations of spectral intervals containing Li lines, bringing us closer to a solution of this problem.

Most studies dealing with observations of lithium lines use the 6708 Å resonance doublet line, and more rarely, the 6103 Å line, which is located in the wing of a strong FeI line. It is difficult to observe lines of neutral lithium: Its abundance is usually low, since LiI is easy to ionize (its ionization potential is $\chi_{ion} = 5.39$ eV). It is possible to observe lithium only in the outermost layers of stellar atmospheres. In addition, the 6708 Å resonance doublet corresponds to a mixture of the ^{6}Li and ^{7}Li isotopes. For most stars, the ratio $R = {}^6\text{Li}/{}^7\text{Li}$ is low; $R < 0.10$ [1].

A large scatter in lithium abundance, up to several orders of magnitude, is observed for evolved stars (red giants), providing evidence for mechanisms that slow lithium depletion. Various suggestions about mechanisms for lithium synthesis in objects showing high lithium abundances have been put forward [2]. One possible factor that could inhibit mixing of stellar material and convective motions is the stellar magnetic field. For example, Wallerstein, Lambert, and coauthors [2–5] have suggested that, during their evolution, lithium-rich giants pass through a stage in which they are chemically peculiar stars with strong magnetic fields and that lithium is synthesized in "spallation reactions" on the stellar surfaces, with the strong magnetic fields accelerating protons and α particles. ^{6}Li can be accumulated in this process.

The available information on lithium abundances in chemically peculiar stars is very contradictory [6, 7]. Such stars have a number of unusual features, first and foremost, chemical anomalies, such as high abundances of heavy elements (especially rare-earth elements), rather strong magnetic fields, and nonuniform distributions of elements over the stellar surface. Application of Doppler imaging techniques to several stars has revealed the presence of spots or rings of anomalous elemental abundances, which are probably related to the magnetic-field structure [8]. Some of these stars—roAp stars—undergo nonradial pulsations on time scales from several minutes to several tens of minutes [9].

The wide range of variations of the lithium line intensity in CP stars [6, 7] suggests that they have a

1063-7729/00/4404-0235$20.00

complicated physical nature. At present, there is still no theory to explain this phenomenon. If lithium is produced in spallation reactions in local flares at the stellar surface, then, for late stars—red giants—this process is stimulated by the excess nitrogen produced in the CNO cycle. In the case of unevolved Ap stars, it is difficult to explain enrichment of products of the CNO cycle, but enhanced lithium abundances could be due to the absence of mixing between outer and inner layers due to the inhibiting action of the stellar magnetic field. If there is no surface mixing, the ^{6}Li/^{7}Li ratio also changes and should be much higher than the solar ratio.

The first results of observations of the pulsating roAp star HD 83368 in the spectral interval around the LiI 6708 Å line (obtained as part of the international project "Lithium in Chemically Peculiar Stars") were presented in [10]. This paper contains a detailed description of observations obtained using the ESO CAT telescope in 1996, together with an interpretation of the LiI 6708 Å line profile variations. In the present study, we continue our analysis of this star's spectrum. Our explanation of variations in the LiI 6708 Å line profile using a spotted-star model is presented in [11]; there, we emphasize the exact synchronism of variations of the magnetic field $H_{\rm eff}$ and of the pulsation amplitude and phase with the position of spots on the star's visible hemisphere.

In this paper, we attempt for the first time to deduce the star's physical nature using a synthetic-spectrum approach based on model atmospheres. HD 83368 is a classical pulsating Ap star and has been very thoroughly studied photometrically. It exhibits SrCrEu peculiarities and has $T_{\rm eff}$ = 7760 K and a radius $R = 2.13 \pm 0.1 R_\odot$. Its effective magnetic field varies with the pulsation amplitude, $H_{\rm eff} = \pm 737$ G. A very large value for the quadratic magnetic field, 11 kG, was found in [12, 13]. The star exhibits a single pulsation mode, whose maxima correspond to orientation of each of the magnetic poles along the line of sight; the interval between two pulsation maxima is half the star's rotation period, $P_{\rm rot} = 2^{\rm d}.851976 \pm 0^{\rm d}.000003$. The multiplet components of the observed pulsation are determined by the rotation frequency [14].

HD 83368 is a very special Ap star and is important for our understanding of both roAp stars in general and models of oblique spotted rotators. The unusual nature of the variability of its frequency spectrum led Kurtz *et al.* [14] to initiate monitoring of this star. In [14], they report the results of photometric observations carried out over the last 15 years.

HD 83368 is a binary, with the primary's brightness $m_V = 6^m.168$. Hauck [15] found that the difference in the magnitudes of the components was $\Delta m = 2^m.78$. Hurly and Warner [16] obtained *UBV* photometric measurements of the two components separately: $V(\mathrm{A}) = 6^m.25$, $B - V = 0^m.25$, $U - B = 0^m.12$; and $V(\mathrm{B}) = 9^m.09$, $B - V = 0^m.64$, $U - B = 0^m.15$. The linear separation between the components is Δr = 217 a.u. and the angular separation is $3''.29$ [17], so that the distance to the system is 66 pc. The masses of the components are $M(\mathrm{A}) = 2.0 M_\odot$ and $M(\mathrm{B}) = 0.9 M_\odot$. The orbital period of the system is at least $P_{\rm orb}$ = 657 yr, and the radial velocity variations corresponding to the orbital period are less than 0.01 km/s per year. Kurtz *et al.* [14] showed that variations of the Doppler shifts due to the orbital motion could be about 10^{-7} Å; this must be borne in mind when analyzing spectroscopic observations corresponding to different phases of the star's rotation.

Quantitative analyses of Ap stellar spectra are usually complicated by the nonuniform distributions of a number of elements over the star's surface, due to the influence of the stellar magnetic field. As far as we are aware, our analysis for HD 83368 in the wavelength intervals 6675–6735 Å, 6120–6170 Å, and 6615–6675 Å is the first. Spectra of HD 83368 in these intervals were obtained by P. North using the CAT telescope of the European Southern Observatory [10]; we analyze these spectra in the present paper.

One problem encountered in this work was taking into account and separating out the effects of Doppler line shifts resulting from nonuniform distributions of elements across the stellar surface, as well as the effects of magnetic intensification of spectral lines. We especially took care in dealing with the 6708 Å lithium line and to lines of other elements with fairly large Lande factors.

2. SPECTRAL ANALYSIS

Figure 1 shows a part of the spectrum near the 6708 Å lithium blend normalized to the continuum. The vertical lines mark the positions of the Li^7 and Li^6 lines. We can also see variable spectral lines whose positions (shifts of the lines as a whole) and profile shapes change. The strongest and most prominent changes occur for the 6708 Å lithium blend itself. Variations are also exhibited by other lines, in particular, those at 6690.8, 6706.7, and 6727.7 Å. It appears that the abundances not only of lithium, but also of other elements, undergo variability associated with differences in the geometrical and physical conditions in spots and the spot-free photosphere.

In our quantitative analysis of the spectra of HD 83368 using the synthetic-spectrum method, we employed the STARSP routine written by Tsymbal [18] and Kurucz model atmospheres [19]. We used the line lists compiled by Kurucz [19, 20] and the VALD data base [21]. We took data on doubly ionized rare-earth elements from the list of Reader and Corliss [22] in the NASA ADC Astrophysical Data Base. Data for some rare-earth lines (NdIII, PrIII, CeII, and CeIII) were provided by Profs. Cowley and Bord of Michigan University and Dr. Sugar of the National Institute of Standards

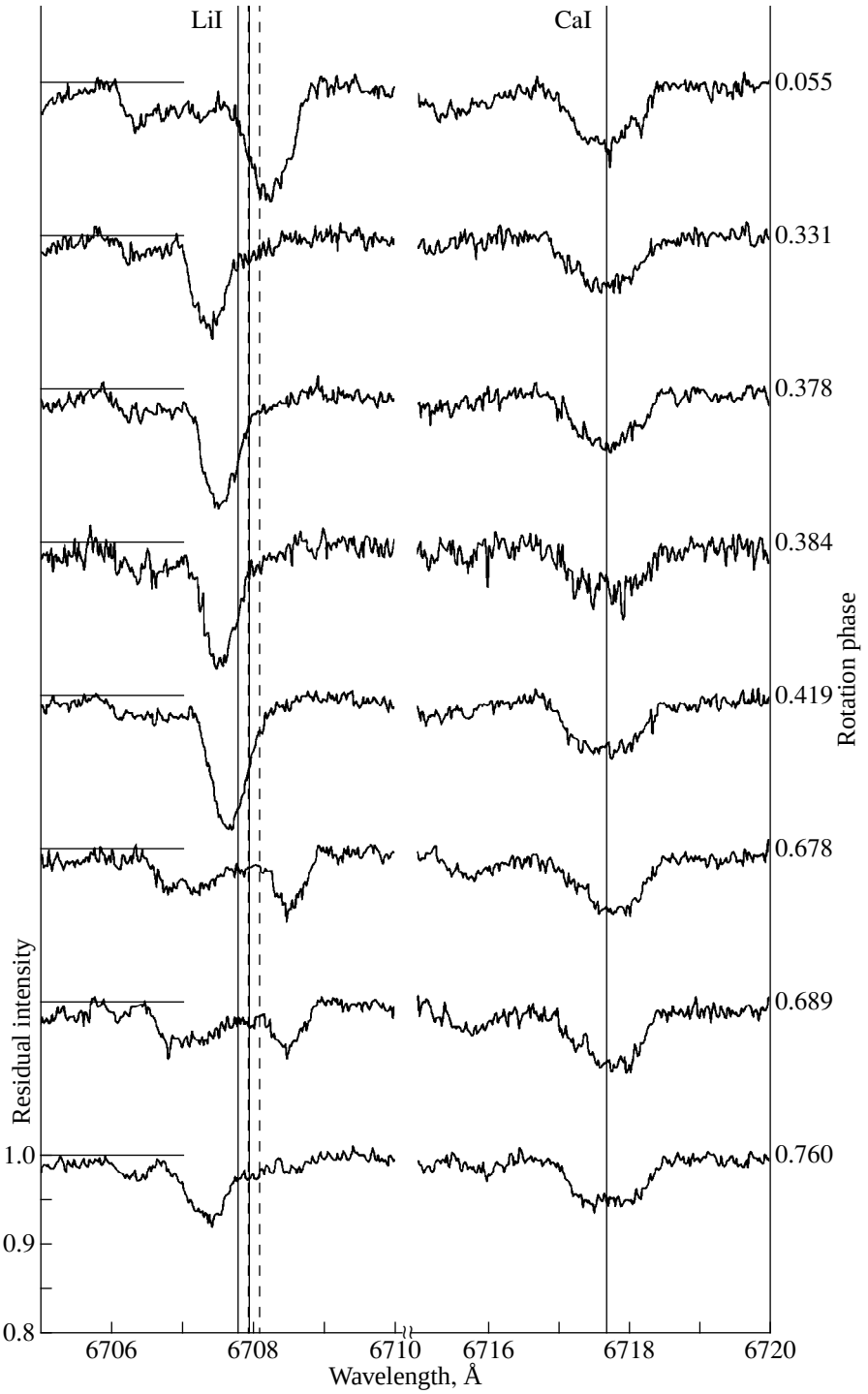

Fig. 1. Spectrum of HD 83368 normalized to the continuum near the lithium 6708 Å blend at various phases. The vertical lines mark the positions of the ^{6}Li and ^{7}Li lines.

and Technology (NIST). When calculating line positions for identifications, we also used NIST data on energy levels; we took the energy levels for DyIII from Spector *et al.* [23].

In our preliminary spectral analysis, we attempted to determine the mean chemical compositions for each rotation phase observed using the single model from the grid of Kurucz with $T_{\rm eff}$ = 7750 K, $\log g$ = 4.0 (in accordance with the data of [10]), and metal abundance [M/H] = 0.0 that best described the behavior of the iron lines in the spectrum. The computed spectra were convolved with the rotation profile for the velocity $v\sin i$ = 34 km/s determined by us from the CaI 6717.68 Å line profiles. Mathys [12] gives $v\sin i$ = 32.6 = ±2.6 km/s.

Table 1. Abundances of elements at various rotation phases

Element	HD 83368									Δlog*N*	Sun	HD 24712	
	Phase and spectrogram No.											min	max
	0.055 Li 48 max	0.320 Li 57	0.331 Li 23	0.378 Li 61	0.384 Li 65	0.419 Li 71 max	0.678 Li 77	0.689 Li 38	0.760 Li 83				
	log*N*												
C I	–3.8		–4.0	–4.5	–4.2	–4.0	–4.2	–3.9	–4.4	0.3	–3.48	–4.5	
N I	–3.1		–4.0	–3.8	–3.6	–3.0	–3.3	–3.2	–3.5	0.3	–3.99	–4.4	
O I		–3.4	–4.3		–3.7	–4.0			–4.4	0.3	–3.11	–3.8	
Na I		–6.1								0.3	–5.71		
Al I	–6.6		–6.5	–6.6	–6.0	–6.3	–6.3	–6.4	–6.1	0.2	–5.57	–5.53	
Si I	–4.0	–4.9	–4.1	–4.4	–4.0	–3.9	–4.1	–4.2	–4.2	0.2	–4.49	–4.43	
S I		–5.2								0.3	–4.83		
Ca I	–5.2	–5.6	–5.5	–5.5	–5.5	–5.3	–5.2	–5.1	–5.6	0.1	–5.68	–5.69	
Ca II		–5.3					–5.8	–5.8		0.3		–5.22	–4.88
Ti II	–7.2		–6.8	–7.3	–6.9	–6.9	–7.1	–7.4	–7.3	0.2	–7.05	–7.22	–7.29
Cr I	–4.1	–5.0	–4.9	–4.4	–4.5	–4.4	–4.4	–4.3	–4.6	0.2	–6.37	–5.93	–5.80
Cr II	–4.4			–4.3	–4.2	–4.6				0.3		–5.58	–5.33
Fe I	–4.6	–4.9	–4.8	–4.7	–4.8	–4.7	–4.7	–4.8	–4.8	0.1	–4.37	–4.77	–4.88
Fe II	–4.5	–4.7	–4.6	–4.4	–4.3	–4.7	–4.4	–4.5	–4.6	0.2		–4.80	–5.11
Co I	–6.3	–5.5				–5.6	–6.0		–6.2	0.3	–7.12	–5.88	–5.57
Y I	–6.4	–6.4	–7.0	–6.6	–6.7	–6.6	–6.4	–6.6	–7.0	0.2	–9.80	–7.80	–7.80
Ba II		–9.1								0.2	–9.91	–9.12	–8.98
La II	–8.5		–9.0	–8.7	–8.6	–8.8	–8.6	–8.4	–9.2	0.4	–10.82	–9.40	–8.75
Ce II	–8.1	–8.8	–8.6	–8.4	–8.2	–8.6	–8.6	–8.3	–8.7	0.2	–10.49	–9.18	–8.90
Pr II		–9.3								0.2	–11.33	–10.15	–9.60
Pr III	–8.5	–8.8	–9.1	–8.9	–8.6	–8.9	–8.5	–8.6	–8.9	0.2			
Nd II	–8.5	–9.3	–9.0	–8.8	–8.6	–8.6	–8.2	–8.4	–8.8	0.3	–10.54	–9.13	–8.64
Nd III	–7.4	–7.8	–8.0	–7.8	–7.8	–7.6	–7.3	–7.4	–7.8	0.2			
Sm II	–8.5		–9.1	–8.6	–8.4	–8.7	–8.7	–8.7	–8.6	0.2	–11.04	–9.75	–9.16
Eu II		–9.8							–9.8*	0.2	–10.53	–9.50	–9.00
Gd II	–8.9			–8.5	–8.4	–8.6	–8.9	–8.9	–8.6	0.3	–10.92	–9.11	–8.70
Lu II		–9.2								0.2	–11.28		

* Estimate obtained for phase 0.768 from the EuII 6645.06 Å line taking into account magnetic splitting

In our comparison of the synthetic and observed spectra, we noted abundance variations that depended on the rotation phase for a number of elements. Such changes were insignificant for iron: The iron abundances derived from FeI lines varied within the range $\log N = -4.6$ to $\log N = -4.9$, while those derived from FeII varied from –4.3 to –4.7. We were able to obtain a fairly reliable estimate of the iron abundance from FeII lines, taking into account Zeeman splitting, for only one phase (0.320) in the interval 6120–6178 Å, using the 6147 Å and 6149 Å lines: $\log N = -4.6$. More substantial variations of abundances with rotation phase were found for lines of CaI (–5.1 to –5.6), CrI (–4.1 to –5.0), and CoI (–5.5 to –6.3).

We also noted variations in the intensities of lines of the light elements C (–3.8 to –4.5), N (–3.0 to –4.0), and O (–3.4 to –4.4), with the nitrogen abundances varying in phase with the stellar magnetic field. Our most trustworthy abundance estimate is that for oxygen, derived from several fairly strong lines near ~6156 Å at phase 0.320. Oxygen abundance determinations based on the weak OI 6726.28 and 6726.54 Å lines encounter difficulties due to blending with the CaII 6726.06 Å line, whose intensity also varies with phase.

Slight variability of the AlI abundance (–6.0 to –6.6) and appreciable variability of the YI abundance (–6.4 to –7.0) were also detected. Table 1 contains $\Delta \log N$ relative to hydrogen and its error $\log N$ for each element.

For comparison, the last columns of this table present the solar abundances and the abundances determined by Ryabchikova *et al.* [24] for a similar roAp star, HD 24712, which also shows variations of its chemical composition that depend on rotation phase (but with no evident LiI 6708 Å line in its spectrum). The abundances of many elements (Fe, Ca, the rare earths) and their behavior are quite similar for the two stars. We took data on the light elements (C, N, O) for HD 24712 from Roby and Lambert [25].

At phases 0.055 and 0.419, which correspond to the passage of the two opposite lithium spots through the central meridian (at these two phases, a spot is nearly in the center of the star's visible hemisphere), we found the highest abundances of N (–3.0), Cr (–4.1), and Fe (–4.6). Note the somewhat different iron abundances derived from lines of FeII ions and FeI atoms at the phase of magnetic minimum. The FeI and FeII abundances are fairly similar at the phase of magnetic maximum. For the remaining elements observed in two ionization states, we will be able to draw conclusions about abundance differences only after a careful analysis of the lines of the rare earth elements, for which no reliable *gf* values are available for the spectral interval considered. For the rare earths themselves, we note differences of the phase distributions (over the surface of the star) of some singly and doubly ionized atoms (NdII and NdIII, PrII and PrIII); however, their maximum abundances primarily correspond to phase 0.055, close to the maximum of the magnetic field.

We found appreciable abundance excesses in the atmosphere of this CrSrEu star relative to the solar abundances for CrI (2.3 dex at magnetic field maximum and 1.4 dex at minimum), YI (3.4 dex and 2.8 dex for maximum and minimum field, respectively), and BaII (0.9 dex; from the 6141.71 Å line only, for a single spectrum taken at phase 0.320). On average, the abundance excesses for the rare earths are 2.3 at phase 0.055, near the magnetic maximum, and 1.8 at phases 0.689 and 0.760, near the magnetic minimum [11]. Table 2 presents these values for each element, together with data for phase 0.320 (6120–6180 Å) and a nearby phase, 0.331, for the lithium interval. For comparison, Table 2 also contains the excesses of these elements for HD 24712 from [24].

We attempted to estimate the magnetic field from the FeII 6147 and 6149 Å line profiles (phase 0.320). We calculated the profiles of these lines taking into account magnetic splitting for two values of the surface magnetic field: ~2 kG (Zeeman splitting, accounted for as described in [11]) and 11 kG (the Paschen–Back effect [12, 13]). Comparison of the computed and observed profiles suggests that $H_s \sim 2$ kG (Fig. 3).

3. RARE EARTHS

We took special care in identifying optical lines of rare earth elements and taking them into account in the synthetic spectrum, especially near the LiI 6708 Å line. Note the NdIII 6690.9 Å, PrIII 6706.70 Å, and PrIII 6727.67 Å lines, whose intensities change in a similar way to that of the lithium line, but with a phase shift relative to it, i.e., relative to the central position of the lithium star spot. For example, Fig. 2 shows two spectra for phases close to magnetic maxima, with the maximum intensities of the lithium line (0.055) and rare-earth lines (0.419). The widths of the rare-earth profiles correspond to $v\sin i$ = 20–21 km/s, providing evidence that the size of their formation region is relatively large compared to that of the lithium spot ($v\sin i$ = 17–18 km/s). The rare-earth lines could be formed in annular structures with nonuniform distributions of these elements encircling the polar regions where the lithium spots are located. Further evidence for such formations follows from the two-component structures of the PrIII and NdIII line profiles, and also of the profiles of some other lines (EuII, BaII, FeII, CrII, SiII) that appear in the spectra at phases 0.6–0.7 (Figs. 3–5). In the available spectra, the two components are of unequal intensity at these phases, suggesting that there are two regions containing Nd and Pr at the limb of the apparent disk of the star. The 6690.9 Å line is probably a complex blend (given $v\sin i$ = 34 km/s and the "spotted" distribution of the rare earth elements) of NdIII 6690.96 Å, ErII 6690.00 Å, and CaI 6691.02 Å. For example, at phase 0.689, the short-wavelength component of NdIII is blended with the ErII line and the long-wavelength component with the CaI line (Fig. 3). Therefore, this line does not show a clear structure, as in the case of NdIII 6145.07 and EuII 6645.06 Å.

Note that the model computations give the maximum intensity of the PrIII 6706.7 Å line for a temperature of 7500 K, whereas the intensities of the NdIII 6145.07 and 6690.96 Å lines are nearly constant for temperatures from 6000 to 7500 K.

In our computations of the synthetic spectrum, we used the PrIII line intensity ratios from the list compiled by Sugar [26]. We determined the *gf* absolute values from the condition that the PrIII and PrII abundances be equal, based on the data from Kurucz [19] for PrII. Choosing the Pr abundance based on the interval 6120–6180 Å at phase 0.320, we were able to reproduce well the PrII and PrIII lines in the lithium-line interval at the nearby phase 0.331.

For two lines of the same multiplet, NdIII 6145.07 and 6690.96 Å, we calculated the relative line intensities assuming LS coupling. Using the value $\log gf = -1.328$ for the 6145.07 Å line [27], we derived $\log gf = -2.50$ for the 6690.96 Å line. Later, we received additional data on NdIII from Bord [28], which yielded the value –2.291, higher by 0.2 dex. Note that Bord [28] claims that the accuracy of his $\log gf$ values is 0.2 dex. Select the Nd abundance based on the 6145.07 Å line (phase 0.320) led to a good agreement between the calculated and the observed intensities of the 6690.96 Å line for the nearby phase 0.331. However, the intensities of the NdII lines from Kurucz's data [19] were too high for this Nd abundance (Fig. 4). The discrepancy in the NdII and NdIII abundances is 0.8–1.5 dex. A similar excess

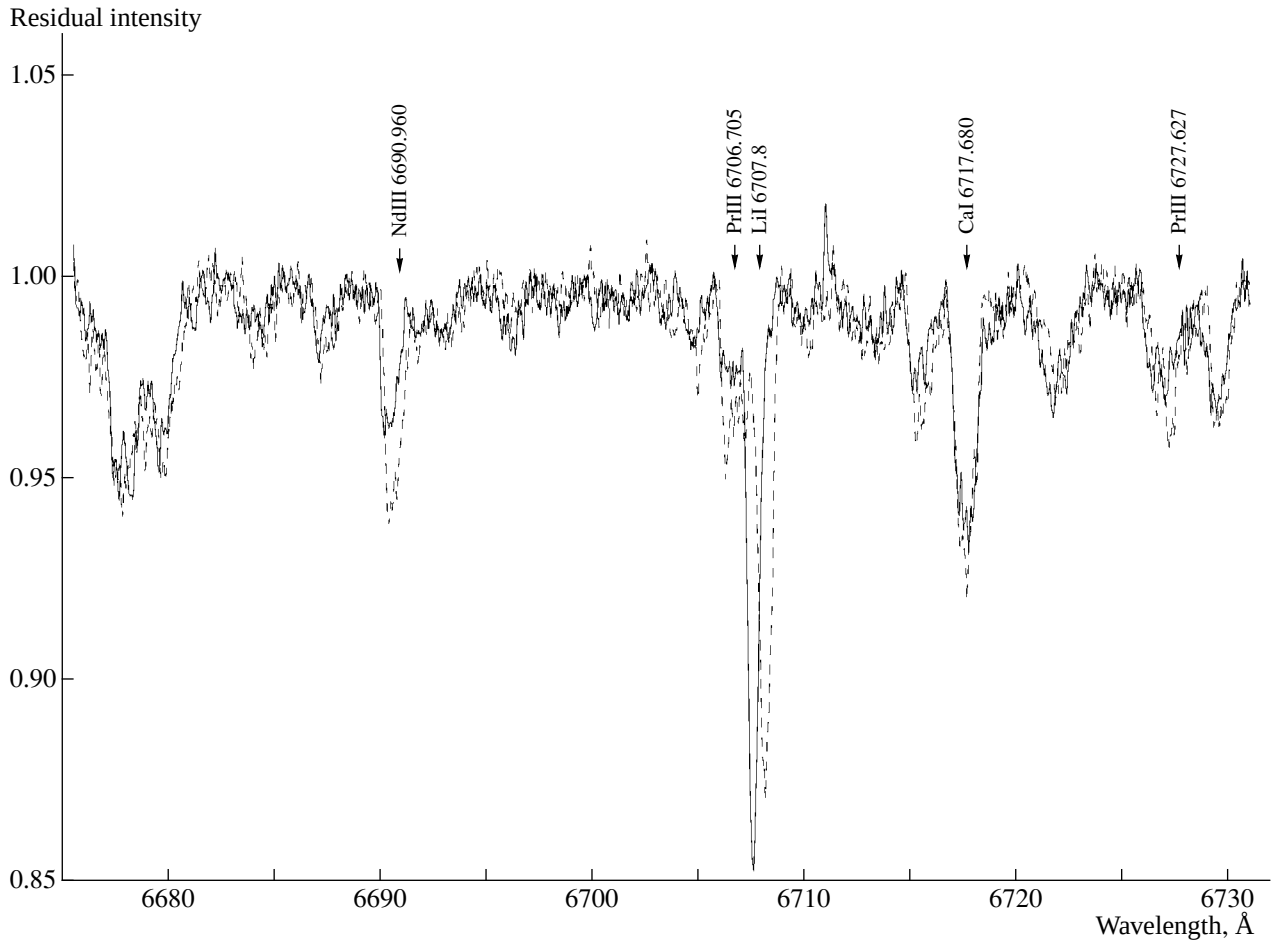

Fig. 2. Comparison between two spectra of HD 83368 for phases closest to the maximum magnetic field. The solid and dashed curves are the spectra for phases 0.419 and 0.055. The NdIII and PrIII lines are obviously enhanced in the latter spectrum.

abundance of PrIII compared to PrII (which has observable lines only at 6120–6180 Å at phase 0.320) is implied by the new $\log gf$ values of Bord [28] for four PrIII lines in the wavelength interval studied: 6160.24 Å (–0.827), 6161.22 Å (–0.728), 6706.70 Å (–1.285), and 6727.63 Å (–3.289). This difference in the abundances of singly ionized and doubly ionized rare-earth elements probably indicates that the spots containing these elements are close to the poles of the stellar dipole magnetic field and that different ions have different distributions over the surface. It could also result from the presence of asymmetrical rings containing rare-earth elements encircling the polar lithium spots. The ambipolar diffusion suggested by Babel [29] provides another mechanism capable of creating anomalies in elemental abundances in circumpolar regions.

4. LITHIUM LINE PROFILES FOR VARIOUS ROTATION PHASES

Our numerous attempts to reproduce the lithium line profiles led to two possible approaches to modeling the spectrum. In the first, we can select a temperature for the circumpolar lithium spot for a given lithium abundance. Our computations indicate that a substantial temperature decrease (to 6000 K) is needed, even for a maximum (initial) lithium abundance of –8.8 (3.2 on the scale $N(\mathrm{H}) = 12.0$). However, such a large temperature difference between the photosphere and the spot is inconsistent with the star's minor photometric variability, though it is possible that a cool layer of enhanced lithium abundance in the presence of a magnetic field is located at the surface of the spot itself. We have no observations near the hydrogen Balmer lines; only one spectrum at phase 0.768 (6615–6675 Å) includes the red wing of the H_α line. The agreement between the theoretical and observed spectra was poor: The H_α wing in the synthetic spectrum is too deep (though the iron lines are reproduced well, using an iron abundance based on two other spectral intervals). This probably testifies to a complex temperature structure in the star's atmosphere.

We attempted to identify molecular bands (TiO, CN, etc.), supposing the existence of cool regions (spots) in the surface atmospheric layers of the star. In the computed spectra, weak TiO and CN lines appear for models with $T_{\mathrm{eff}} = 5000$–5500 K. We could not find even the

most intense and prominent lines of these molecules in the observed spectrum. Another possibility is that there is stratification of the lithium in the stellar atmosphere, so that it is concentrated in the surface layers of the spots; this is possible in the absence of convection, under the stabilizing influence of the magnetic field at the poles.

Let us now consider the physical conditions in the spots. Assuming that the star's brightness variations are synchronous with its rotation, we can impose certain restrictions on possible differences in the physical conditions in the spots and the stellar photosphere. For HD 83368, the structure of the spots must lead to the *B* and *V* light curves having opposite phases [11]. We know of three possible explanations for brightness variability when a spot appears on the visible part of its surface.

(1) The spot and surrounding photosphere have different temperatures.

(2) The spot and photosphere have different metallicities, a hypothesis most frequently invoked for Ap stars.

(3) Similar to case (2), there is a metallicity excess, but for the rare-earth rather than the iron-peak elements.

In contrast to cases (1) and (2), this last hypothesis is very difficult to verify, since no calculations of model atmospheres and theoretical colors are currently available for such chemical compositions. A nonuniform (spotted) distribution of rare-earth elements over the stellar surface could also explain the observed variation of the oscillation amplitude with the rotation phase [31].

Analysis of the variations of the theoretical *B* and *V* colors with $T_{\rm eff}$ and metallicity [19] shows that different effective temperatures for the spot and photosphere cannot simultaneously explain the brightness variations in these two filters, since the observed *B* and *V* light curves are out of phase, whereas the theoretical curves are in phase. A metallicity gradient could lead to the curves' opposite phases only if the metal abundances in the star's photosphere and spot are 0.5 and 1.0 dex in excess of the solar value, respectively. However, such high metal abundances are inconsistent with the spectroscopic observations: On the contrary, the iron lines in the spectrum of HD 83368 are somewhat weaker than expected for a solar iron abundance. Thus, we are forced to adopt the third hypothesis and to suppose that the opposite phases of the *B* and *V* light curves are the result of strong ultraviolet absorption by rare-earth lines and that the abundances of these elements in spots considerably exceed those in the stellar photosphere.

Table 2. Excesses of some elements for rotation phases close to the maximum and minimum surface magnetic field

Element	HD 83368					HD 24712	
	phase						
	0.055 max	0.320	0.331	0.687	0.760	min	max
	$\log(N/N_0)$						
N I	0.9		0.0	0.8	0.5		−0.4
Ca I	0.6			0.6	0.2		0.0
Cr I	2.3	1.4	1.5	2.1	1.8	0.6	0.4
Cr II	2.0					1.0	0.8
Fe I	−0.2	−0.5	−0.4	−0.4	−0.4	−0.4	−0.5
Fe II	0.1	−0.3	−0.2	−0.2	−0.2	−0.4	−0.7
Y I	3.4	3.4	2.8	3.2	2.8	2.0	2.0
Y II						1.5	1.5
Ba II		0.9				0.9	0.8
REE							
La II	2.3		1.8	2.4	1.6	2.1	1.4
Ce II	2.4	1.7	1.9	2.2	1.9	1.6	1.3
Pr II		1.8				1.7	1.2
Pr III	2.8	2.5	2.2	2.7	2.4		
Nd II	2.0	1.2	1.5	2.1	1.7	1.9	1.4
Nd III	3.1	2.7	2.5	3.1	2.7		
Sm II	2.5		1.9	2.3	2.4	1.9	1.3
Eu II		0.7			0.7*	1.5	1.0
Gd II	2.5		2.0	2.0	2.3	2.2	1.8

* Estimate obtained for phase 0.768 from the EuII 6645.06 Å line.

5. CALCULATION OF A LINE PROFILE FOR A ROTATING, SPOTTED STAR

For a rotating star, the observed radiation arriving from the receding side of the stellar disk is redshifted in accordance with the Doppler effect, while the radiation from the approaching side is blueshifted. Therefore, the rotation broadens all the star's lines. For a single rotating star, the amount of broadening depends on the equatorial rotation velocity v_e and the inclination *i* of the rotation axis to the line of sight, since we measure the projection of v_e onto the line of sight, $v_e \sin i$.

We will subdivide the stellar surface into 32×32 points with rectangular coordinates (x_i, y_i), each point being a Gaussian quadrature node. Let $I(x, y, \lambda - \lambda_c)$ be the radiation intensity from the point (x, y) on the surface of the nonrotating star in a spectral line at a wavelength separated from the central wavelength λ_c by $\lambda - \lambda_c$ [32]. If the star rotates, we have $\lambda_c - (\lambda_c v_z/c)$ in place of λ_c, where v_z is the radial velocity at the point (x, y) and *c* is the speed of light. Since $v_z = -x v_e \sin i$, the intensity emerging from the point (x, y) on the surface of a uniformly rotating star can be written $I(x, y, \lambda - \lambda_c - \lambda_c x(v_e/c)\sin i)$, and the line profile can be calculated using the formula from [32]:

$$\bar{r}(\lambda - \lambda_c) = \frac{\int_{-1}^{1} dx \int_{0}^{\sqrt{1-x^2}} I[x, y, \lambda - \lambda_c - \lambda_c x(v_e/c)\sin i]dy}{\int_{-1}^{1} dx \int_{0}^{\sqrt{1-x^2}} I_0(x, y)dy},$$

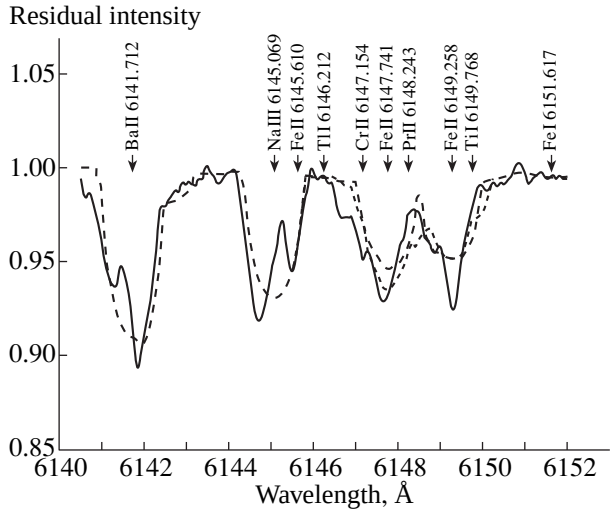

Fig. 3. Calculated profiles of the FeII 6147.7 and 6149.26 Å lines taking into account magnetic splitting. The solid curve is the observed spectrum for phase 0.320; the dashed curve, the spectrum calculated for a 2-kG field; and the dotted curve, the spectrum calculated for a 11-kG field. $v\sin i$ = 34 km/s was used for both calculated spectra.

where $I_0(x, y)$ is the intensity of the continuum radiation emitted by the point (x, y) on the disk and $I(x, y)$ is the specific intensity calculated for each point of the star's visible surface, taking into account the presence of spots with different chemical compositions. Note that this approach enables us to take into account most accurately the effect of limb darkening, which additionally weakens the line emission at rotation phases when a spot with enhanced abundance of the given element is located at the edge of the star's visible disk.

We assume the presence of spherically symmetrical spots, with a uniform abundance of a given element within each spot. The coordinates and radius of the spot are given in the spherical coordinate system of the observer (φ, l), which is related to the Cartesian coordinates (x, y, z) via the intermediate spherical coordinates (r, θ, ψ) describing the visible hemisphere of the star:

$$x = r\sin\theta\cos\psi,$$

$$y = z\sin\theta\sin\psi,$$

$$\sin\varphi = -\cos\theta\cos i + \sin\theta\sin i\sin\psi,$$

$$\cos\varphi\cos(l - \omega t) = \cos\theta\sin i + \sin\theta\cos i\sin\psi,$$

where i is the angle between the star's rotation axis and the line of sight and ωt is the rotation phase.

Of course, the best way to reveal the spotted structure of the stellar surface would be to solve the inverse problem. However, this requires higher quality observational material and, most importantly, distribution of the data over a larger number of rotation phases. Therefore, we used direct modeling of the spectra, which imposes known limitations on the accuracy of the results.

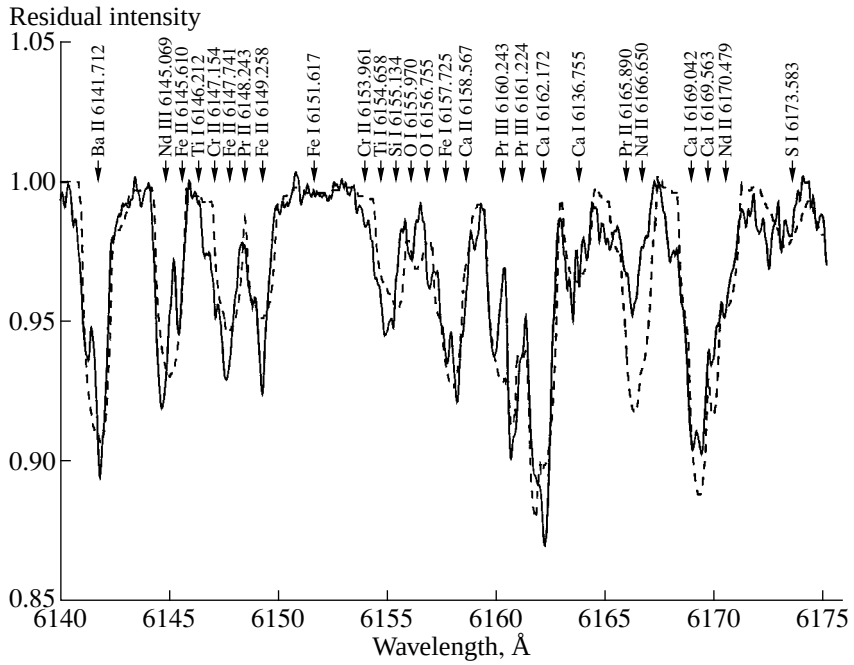

Fig. 4. Spectrum of HD 83368 at 6140–6175 Å. The solid curve is the observed spectrum for phase 0.320, and the dashed curve is the spectrum calculated for a Kurucz model with $T_{\rm eff}$ = 7750 K, $\log g$ = 4.0, and [M/H] = 0.0 convolved with the rotation profile for $v\sin i$ = 34 km/s. The two-component structure of the BaII 6141.71 Å and NdIII 6145.07 Å lines can clearly be seen. When choosing the Nd and Pr abundances, we tried to reproduce the NdIII and PrIII line intensities. The NdII and Pr lines with *gf* values from Kurucz's list (and the new VALD list, 1999) proved to be overly enhanced in the computed spectrum.

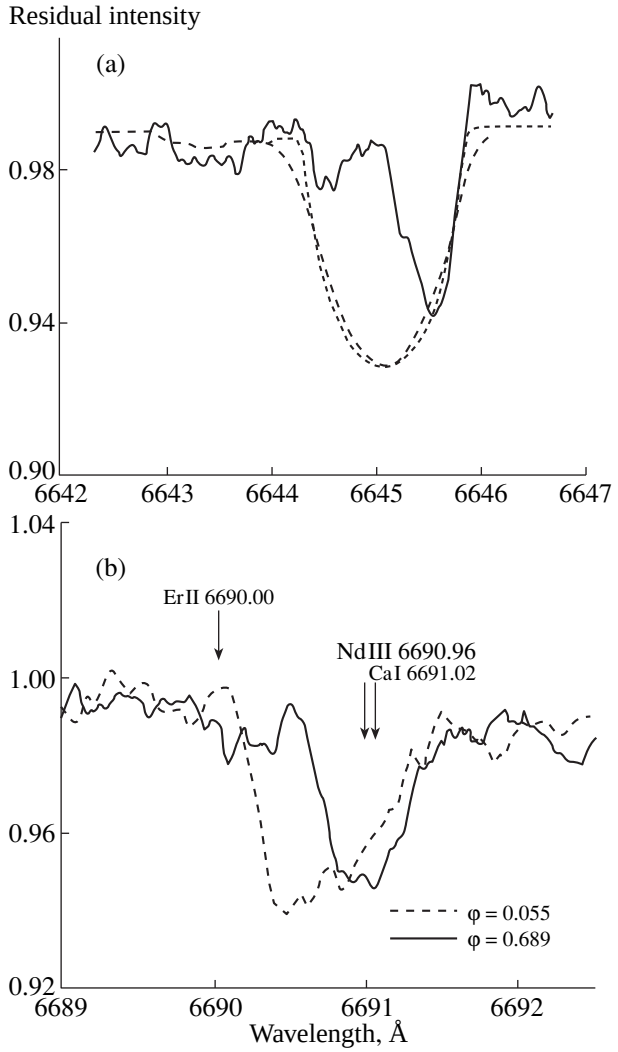

Fig. 5. (a) Profile of the EuII 6645.06 Å line. The solid curve is the observed spectrum for phase 0.768, and the dashed and dotted curves are the calculated spectra for 11 and 2-kG fields with $v\sin i$ = 34 km/s. In the model spectra, we used an obviously high EuII abundance ($\log N = -9.5$) in order to demonstrate that the two components should be identified with the EuII 6645.06 Å line. (b) Profile of the NdIII 6690.97 Å line for phase 0.055, close to the magnetic maximum (dashed curve), and for phase 0.689, close to the magnetic minimum (solid curve).

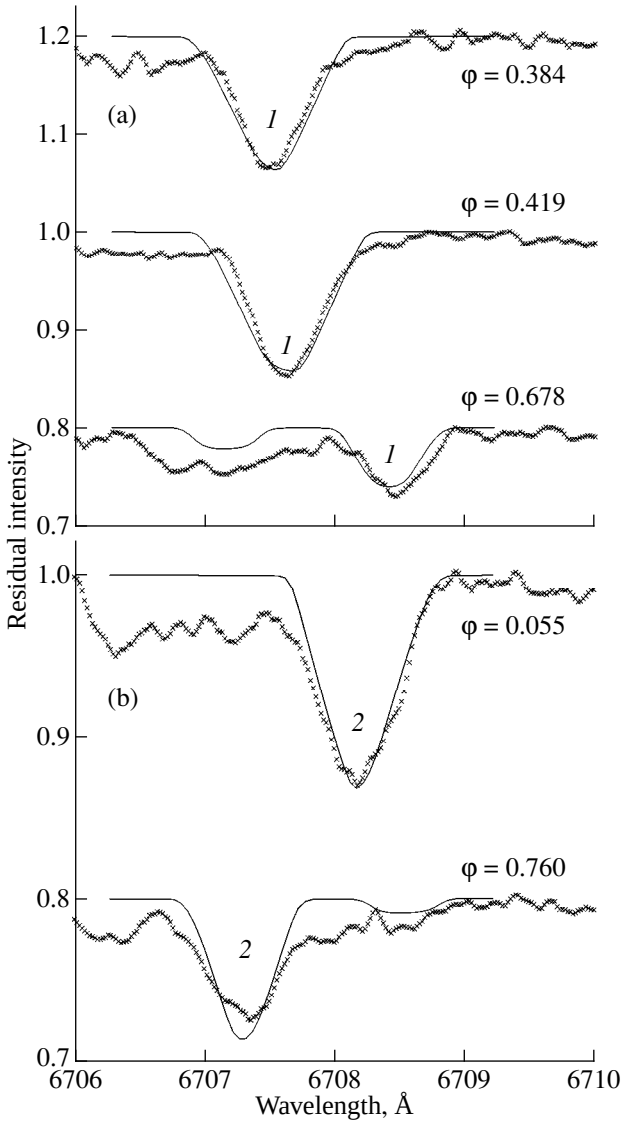

Fig. 6. Theoretical and observed spectra for five rotation phases using the best-fit parameters for "lithium" spots (a) 1 and (b) 2.

After elucidating questions connected with the different physical conditions in the spots and surrounding photosphere (discussion above), the parameters of the problem are

(1) the angle between the star's rotation axis and the line of sight (i),

(2) the equatorial rotation velocity of the star (v_e),

(3) the number of spots,

(4) the coordinates and sizes of each spot,

(5) the Li abundance in each spot.

We selected the parameters yielding the best agreement between the observed and theoretical spectra. Note that, if we vary the parameters over the entire range of possible values, we can draw conclusions about the uniqueness of the results: Only one combination of parameters leads to agreement of the theory and observations for all phases.

We derived the following spot positions, sizes, and lithium abundances from our calculations of the LiI 6708 Å line profiles for a model atmosphere with $T_{\rm eff}$ = 7750 K, $\log g$ = 4.0, $i = 90°$, and v_e = 35 km/s:

Spot 1 : l = 173°, φ = 0°, $R = 33°.5$, $\varepsilon_{\rm Li} = -7.13$,

Spot 2 : l = 337°, φ = 0°, $R = 35°$, $\varepsilon_{\rm Li} = -7.23$.

(Fig. 6). In the calculations, we took into account 10 fine-structure components of the Li line corresponding to the inferred magnetic field. Figure 7 shows the posi-

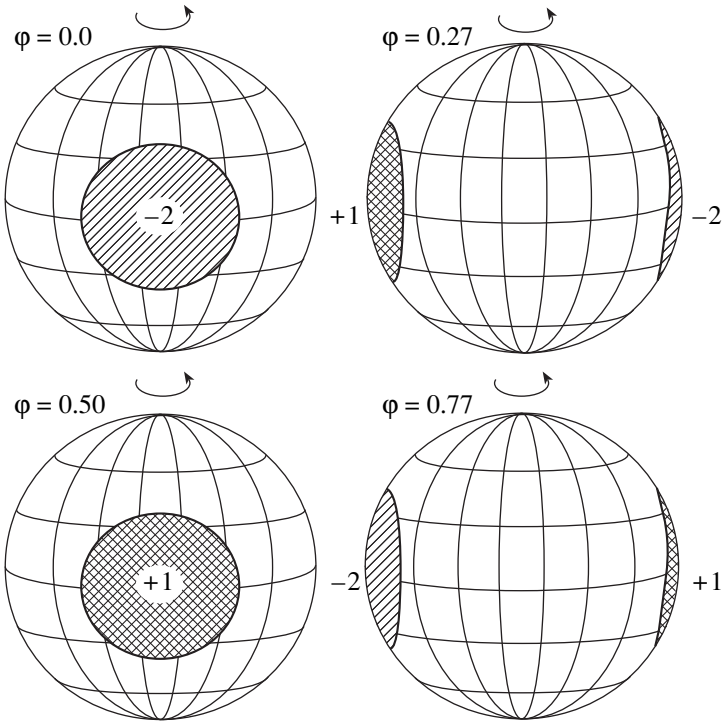

Fig. 7. Spherical model of the surface of HD 83368 with "lithium" spots 1 and 2 [11].

tions of the spots on the stellar surface. Note that they coincide with the positions of the magnetic poles of the dipole field.

It is interesting that, from the onset, the main question was whether the phase-dependent spectral feature should be identified precisely with the Li line. Our analysis shows that even a small change of the laboratory wavelength for the theoretical line makes it impossible to reproduce the observed Doppler shift due to the stellar rotation at all phases.

Note that we calculated the magnetic splitting of the LiI line for each rotation phase based on the appropriate value of the variable magnetic field and the position of the dipole axis relative to the line of sight. However, the fairly high rotation velocity of the star ($v \sin i$ = 34 km/s) "washes out" the effect of the magnetic splitting so that, in order to obtain a good description of the behavior of the LiI line with rotation phase, it is sufficient to take into account only components of the multiplet splitting.

Another problem encountered in describing the LiI 6708 Å line profile is its redward shift at phase 0.678 (Fig. 6b). A search for blending lines, especially of rare earth elements, suggested the CeII 6708.10 Å line. We calculated the position of this line using the NIST energy levels. Unfortunately, no *gf* value is available, and the line is not included in the lists of Kurucz [20] or Reader and Corliss [22]. However, judging from eyeball estimates of the CeII line intensities [30] near the lithium line, the CeII 6708.10 Å line seems to make only a minor contribution to the lithium blend, suggesting the presence of a substantial amount of ^{6}Li in the spot. To describe the red wing of the lithium doublet at phase 0.678, it is necessary to assume ^{6}Li/^{7}Li = 0.5 in the calculations. However, the remaining deviations between the theoretical and the observed spectra are most probably due to a more complicated structure of the lithium spots than assumed in our model with two symmetrical spots.

The question of the lithium abundance is still open to discussion. It is likely that a high lithium abundance is preserved by the action of the magnetic field only in the outmost surface layers of the spot.

ACKNOWLEDGMENTS

We thank P. North, who provided observational data, M. Hack for a discussion and valuable advice, S. Sergeev for his permission to use the SPE routine for spectral reduction, to Prof. Cowley for numerous suggestions and for providing data on rare-earth elements, to M.Ya. Orlov for useful discussions, to D. Bord and J. Sugar for assistance and providing data, and to L.S. Lyubimkov for reading the paper and providing useful criticism. One of the authors (V. Ts.) wishes to thank A. Yakushechkin, the president of "Master Games," for sponsoring the development of the software used in this study.

REFERENCES

1. J. Andersen, B. Gustafsson, and D. L. Lambert, Astron. Astrophys. **136**, 65 (1984).

2. G. Wallerstein and P. Conti, Ann. Rev. Astron. Astrophys. **7**, 99 (1969).
3. G. Wallerstein and C. Sneden, Astrophys. J. **255**, 577 (1982).
4. D. Lambert and L. Ries, Astrophys. J. **248**, 228 (1981).
5. D. Lambert and S. Sawyer, Astrophys. J. **283**, 192 (1984).
6. R. Faraggiana, M. Gerbaldi, and F. Delmas, Astrophys. Space Sci. **238**, 169 (1996).
7. M. Hack, N. S. Polosukhina, V. Malanushenko, *et al.*, Astron. Astrophys. **319**, 637 (1997).
8. A. P. Hatzes, Mon. Not. R. Astron. Soc. **253**, 89 (1991).
9. D. W. Kurtz, Ann. Rev. Astron. Astrophys. **28**, 607 (1990).
10. P. North, N. Polosukhina, V. Malanushenko, *et al.*, Astron. Astrophys. **333**, 644 (1998).
11. N. Polosukhina, V. Khalak, A. Shavrina, *et al.*, Pis'ma Astron. Zh. (in press).
12. G. Mathys, Astron. Astrophys. **293**, 746 (1995).
13. G. Mathys and S. Hubrig, Astron. Astrophys., Suppl. Ser. **124**, 475 (1997).
14. D. W. Kurtz, F. van Wyk, G. Goberts, *et al.*, Mon. Not. R. Astron. Soc. **287**, 69 (1997).
15. B. Hauck, Astron. Astrophys. **69**, 285 (1978).
16. P. Hurly and B. Warner, Mon. Not. R. Astron. Soc. **202**, 761 (1983).
17. D. Hoffleit and C. Jaschek, *The Bright Star Catalogue, 4th Ed.* (Yale Univ. Observ., New Haven, 1982), p. 472.
18. V. V. Tsymbal, Odessa Astron. Publ. **7**, 146 (1994).
19. R. L. Kurucz, CDROM-13, CDROM-23 (1993).
20. R. L. Kurucz, Preprint No. 4080, Harvard-Smithsonian Center for Astrophysics (1995).
21. N. E. Piskunov, F. Kupka, T. A. Ryabchikova, *et al.*, Astron. Astrophys., Suppl. Ser. **112**, 525 (1995).
22. J. Reader and C. H. Corliss, *Line Spectra of the Elements* (ADC NASA, CDROM 3, 1980–81).
23. N. Spector, J. Sugar, and J.-F. Wyart, J. Opt. Soc. Am. B: Opt. Phys. **14**, 511 (1997).
24. T. A. Ryabchikova, J. D. Landstreet, M. J. Gelbmann, *et al.*, Astron. Astrophys. **327**, 1137 (1997).
25. S. N. Roby and D. L. Lambert, Astrophys. J., Suppl. Ser. **73**, 67 (1990).
26. J. Sugar, J. Res. Natl. Bur. Stand. **78**, 555 (1974).
27. C. R. Cowley and D. J. Bord, ASP Conf. Proc. **143** (1988).
28. D. Bord, private communication, 1998.
29. J. Babel, *Peculiar Versus Normal Phenomena in A-Type and Related Stars*, Ed. by M. M. Dworetsky, F. Castelli, and R. Faraggiana; ASP Conf. Ser. **44**, 458 (1993).
30. C. Corliss, J. Res. Natl. Bur. Stand. **77**, 419 (1973).
31. D. E. Mkrtichian, private communication, 1998.
32. J.-L. Tassoul, *Theory of Rotating Stars* (Princeton Univ., Princeton, 1978), p. 472.

Translated by N. Samus'

Astronomy Reports, Vol. 44, No. 4, 2000, pp. 246–254. Translated from Astronomicheskiĭ Zhurnal, Vol. 77, No. 4, 2000, pp. 285–294.

Solar Analogs: Spectral Energy Distributions and Physical Parameters of Their Atmospheres

I. N. Glushneva, V. I. Shenavrin, and I. A. Roshchina

Sternberg Astronomical Institute,
Universitetskiĭ pr. 13, Moscow, 119899 Russia

Received April 12, 1999

Abstract—The angular diameters, radii, and effective temperatures of 16 G0–G5 main-sequence stars with color excesses $0.60 \le B–V \le 0.68$ and parallaxes derived from Hipparcos data have been determined using their infrared fluxes, obtained from *JHKLM* photometric observations. For all the stars except BS 483, these effective temperatures differ from the spectroscopic temperatures by no more than 1–2%. Such differences are within the uncertainties expected for the IR-flux method. The effective temperatures of BS 483 derived from its infrared fluxes are 3% higher than those indicated by spectroscopic observations; this may be due to the specific atmospheric structure of this star. Spectroscopic observations at 3400–7500 Å and *JHKLM* photometric observations are compared with analogous solar data and Kurucz models. The best agreement with the model with $T_{eff} = 5750$ K and $\log g = 4.5$ in the interval 4400–7500 Å was obtained for BS 7503 and BS 7504 (16 Cyg A and 16 Cyg B). The infrared color indices $H – K$, $K – L$, and $K – M$ for these stars differ from the corresponding solar indices, and their angular diameters grow with wavelength, which is not the case for the Sun. $H – K$ for BS 6060, currently considered to be the closest analog to the Sun, is near the solar value. The vast majority of the stars studied (13 of 16) have higher luminosities than the Sun. These include 16 Cyg A, 16 Cyg B, and 51 Peg, which thus cannot be considered full "twins" of the Sun. © *2000 MAIK "Nauka/Interperiodica"*.

1. INTRODUCTION

Successful searches for solar "twins"—stars with the same effective temperature, mass, age, luminosity, gravitational acceleration, chemical composition, velocity field, magnetic field, and chromospheric activity as the Sun—are viable only if they include comprehensive investigations of solar-type stars (so-called solar analogs) with very similar photometric characteristics. Since various studies present $B–V$ values for the Sun that vary over rather wide limits, we must consider stars with $B–V$ from 0.62 (or even somewhat smaller values) to 0.68. For example, Cayrel de Strobel [1] proposed a list of 109 stars with $B–V$ from 0.59 to 0.69. It is very relevant that these stars now have high-accuracy parallaxes from Hipparcos measurements [2], making it possible to determine their bolometric magnitudes very accurately.

We began our investigations of solar-type stars with the determination of the physical parameters of the atmospheres of 12 G0–G8 stars from the spectrophotometric catalog of the Sternberg Astronomical Institute [3]. Glushneva *et al.* [4] obtained the total fluxes, angular diameters, radii, and effective temperatures of these stars. Due to uncertainties in the stellar parallaxes, the luminosities and radii could vary over rather wide intervals. It was also noted in [4] that the luminosities of nearly all of the stars studied (9 of 11) were higher than the luminosity of the Sun, possibly indicating that the parallaxes of these stars were underestimated.

A comparison of the observed *WBVR* color indices for the stars obtained at the Tian-Shan High Mountain Observatory [5] with synthetic color indices for the Sun demonstrated that $(W–B)_\odot$ corresponded to the mean value of this color index for stars of spectral class G1.5. This result was confirmed by a direct comparison of the energy distributions for the studied stars and the Sun at 3200–5500 Å [6]. At the same time, $(B–V)_\odot$ corresponded to the mean value for G3–G5 stars [4, 6].

Glushneva *et al.* [7] analyzed the 3400–7500 Å energy distributions and infrared color indices $J–H$, $J–K$, $J–L$, and $J–M$ for eight G1.5–G3 main-sequence stars. Among these, the characteristics of 16 Cyg A, 16 Cyg B, and 18 Sco are considered closest to those of the Sun [8].

The aims of the present paper are to enhance the list of studied stars by considering stars for which there are high-accuracy Hipparcos parallaxes [2], derive the main physical characteristics of these stars—effective temperature, angular diameter, and radii—from their infrared fluxes, and compare the observed visible and IR energy distributions with theoretical Kurucz models.

2. *JHKLM* PHOTOMETRY

Table 1 presents a list of the stars studied and their characteristics. The columns give the stars' HD and BS numbers, spectral types, V magnitudes and $B–V$ color indices from [5], effective temperatures T_{eff}, bolometric magnitudes, gravitational accelerations $\log g$ derived

1063-7729/00/4404-0246$20.00

Table 1. Photometric and spectroscopic parameter for the program stars

HD	BS	Sp	V	$B–V$	T_{eff}, K	M_{bol}	log$g$	F, 10^{-7} erg cm^{-2} s^{-1}	π
1835	88	G2V	6.402	0.660	5781	4.775	4.50	0.717	0.049
10307	483	G1.5V	4.965	0.623	5538	4.394	4.40	2.61	0.079
11131		dG1	6.752	0.625	5820	4.71*	4.37	0.596	0.435
20630	996	G5V	4.843	0.674	5631	4.916	4.83	3.12	0.109
25680	1262	G5V	5.910	0.626	5794	4.63*	4.30	1.21	0.60
28099		G2V	8.105	0.662	5775	4.695	4.50	0.164	0.0214
76151	3538	G3V	6.013	0.671	5727	4.773	4.50	1.01	0.058
86728	3951	G1.5V	5.385	0.676	5727	4.423	4.28	1.85	0.067
89010	4030	G1.5IV–V	5.968	0.668	5598	3.457	4.00	1.09	0.033
146233	6060	G2Va	5.499	0.650	5789	4.693	4.18	1.61	0.071
186408	7503	G1.5V	5.986	0.659	5780	4.234	4.29	1.03	0.046
186427	7504	G2.5V	6.244	0.671	5765	4.518	4.30	0.823	0.047
187923	7569	G0V	6.164	0.664	5727	3.872		0.885	0.036
193664	7783	G3V	5.932	0.601	5998	4.640		1.10	0.057
213575		G2V	6.951	0.677	–	3.983		0.482	0.028
217014	8729	G2.5IVa	5.459	0.676	5755	4.458	4.18	1.68	0.065

from spectroscopic measurements [1, 9], total fluxes F calculated by us using spectroscopic data, and Hipparcos parallaxes. Values of M_{bol} derived from ground-based observations are marked with an asterisk.

It is important to note that the bolometric magnitudes of most of the stars (13 of 16) are lower than the solar value ($M_\odot = 4.75$). We carried out infrared photometric observations on the 125-cm reflector of the Crimean Laboratory of the Sternberg Astronomical Institute using a *JHKLM* photometer [10]. Each of the program stars were observed over 2–3 nights. We did not try to account for atmospheric absorption, since the observing schedule was constructed such that the differences in the air masses for the program and standard stars were minimum. As a rule, this difference was several thousandths of an air mass, and only rarely reached values as high as 0.05.

We used BS 334, BS 458, BS 539, BS 1101, BS 1256, BS 1411, BS 3748, BS 3905, BS 4031, BS 6075, BS 7328, BS 7557, BS 7957, BS 8499, and BS 8684 as standard stars. All these stars are in the catalog of Johnson *et al.* [11]. Since the H magnitudes for all the stars and the L and M magnitudes for many of them are not given in this catalog, we calculated them using the formulas presented by Korneef [12]. The accuracy of the observations was $0\overset{m}{.}02$ in the J, H, and K bands; $0\overset{m}{.}03$ in the L band; and $0\overset{m}{.}05$ in the M band. Table 2 presents the infrared magnitudes for the program and standard stars.

3. EFFECTIVE TEMPERATURES AND ANGULAR DIAMETERS OF THE STARS

We determined the effective temperatures and angular diameters of the program stars using their IR fluxes (the method of Blackwell and Shallis [13]); these two quantities are found jointly using the total flux and monochromatic flux in the infrared. The resulting accuracies in the temperatures and angular diameters are 1% and 2%, respectively, if the input data are sufficiently accurate. The effective temperature and angular diameter are calculated using the formulas

$$T_{eff}^4 = \frac{4F}{\sigma\theta^2}, \quad \theta = 2\sqrt{\frac{F_\nu}{f_\nu}}, \tag{1}$$

where T_{eff} is the effective temperature, θ the angular diameter, F the total flux, F_ν the monochromatic flux measured on the Earth, and f_ν the flux emitted at the surface of the star.

As noted above, we calculated the total fluxes in Table 1 based on spectroscopic determinations of the effective temperatures and bolometric magnitudes. We determined the total fluxes for four of the stars using integrated spectroscopic data in the ultraviolet, visible, and infrared [4].

Below, we present a comparison of the F values in units of 10^{-7} erg cm^{-2} s^{-1} obtained using the two methods:

	F (Table 1)	F [4]
BS 483	2.61	2.81
BS 996	3.12	3.16
BS 7503	1.03	1.04
BS 7504	0.823	0.836

With the exception of BS 483, the differences in the two total fluxes are no more than 1.6%. We used the calibration relation of Korneef [12] to convert the infrared

Table 2. Infrared magnitudes

HD	*J*	*H*	*K*	*L*	*M*
1835	5.29	4.91	4.84	4.88	4.88
10307	3.90	3.58	3.54	3.44	3.52
11131	5.56	5.22	5.15	5.14	
20630	3.70	3.40	3.31	3.26	3.32
25680	4.78	4.48	4.40	4.38	4.43
28099	6.91	6.61	6.53	6.51	
76151	4.85	4.54	4.47	4.37	
86728	4.21	3.88	3.81	3.81	3.83
89010	4.78	4.48	4.42	4.40	4.46
146233	4.39	4.05	4.00	4.02	4.11
186408	4.89	4.57	4.47	4.39	4.53
186427	5.11	4.77	4.69	4.61	4.75
187923	5.01	4.67	4.60	4.56	
193664	4.94	4.61	4.53	4.46	4.64
213575	5.74	5.38	5.32	5.29	
217014	4.38	4.07	3.98	3.95	4.12

Standard stars

HD	Standard	*V*	*J*	*H*	*K*	*L*	*M*
1835	BS 334	3.45	1.58	0.98	0.83	0.77	0.89
10307	BS 458	4.10	3.17	2.91	2.85	2.79	2.85
11131	BS 539	3.72	1.92	1.37	1.23	1.17	–
20630	BS 1101	4.28	3.28	3.01	2.94	2.90	2.98
25680	BS 1256	4.37	2.63	2.10	1.97	1.91	2.05
28099	BS 1411	3.83	2.29	1.84	1.73	1.67	–
76151	BS 3748	1.97	–0.33	–1.02	–1.19	–1.37	–1.12
86728	BS 3905	3.88	1.93	1.36	1.22	1.15	0.30
89010	BS 4031	3.44	2.81	2.66	2.62	2.59	2.64
146233	BS 6075	3.23	1.60	1.11	0.99	0.96	1.05
186408	BS 7328	3.76	2.25	1.79	1.67	1.58	1.70
186427	BS 7328	3.76	2.25	1.79	1.67	1.58	1.70
187923	BS 7557	0.76	0.39	0.29	0.26	0.21	0.26
193664	BS 7957	3.43	1.90	1.40	1.28	1.19	1.31
213575	BS 8499	4.15	2.58	2.12	2.01	1.95	2.05
217014	BS 8684	3.48	2.01	1.55	1.43	1.38	1.50

JHKLM magnitudes to the monochromatic fluxes F_ν. We determined the emitted flux f_ν using the models of Kurucz [14], choosing the model with solar chemical composition with T_{eff} and $\log g$ that were closest to the values in Table 1.

Table 3 presents our results for the effective temperatures and angular diameters of the stars in the *JHKLM* bands. Analysis of this table shows that, for many of the stars, the T_{eff} and θ values derived from observations in different IR bands are very similar. In many cases, the divergences between T_{eff} values are less than 1%. At the same time, earlier determinations of T_{eff} using the IR-flux method (see, for example, [15]) indicated a clear dependence of the effective temperature on the observing band; the smallest differences between T_{eff} and the effective temperatures derived from direct interferometric measurements were obtained for the *K* band. The good agreement between the T_{eff} values in different IR bands obtained here is apparently due to both the more realistic models of Kurucz (1992) compared to those used earlier (1979) and our use of uniform, high-accuracy *JHK* photometric observations.

One important feature of the data in Table 3 is the increase in the angular diameters (and corresponding decrease in effective temperatures) with increasing wavelength observed for several stars (16 Cyg A, 16 Cyg B, BS 7783, and BS 8729). It is interesting that three of these stars (16 Cyg A, 16 Cyg B, and BS 8729) have at various times been considered among the closest analogs of the Sun [9]. This dependence is not displayed by the Sun. In these four stars, the angular diameters in the *L* band are, on average, 5% larger than in the *J* band; in the remaining stars, the mean difference in the diameters in these two bands is only 1.5%. This increase in angular diameter with IR wavelength could be associated with the presence of additional absorption in gas or dust envelopes around these stars. In all four stars, the angular diameter in the *M* band decreases; however, the accuracy of the monochromatic fluxes in this band is, on average, 5%, while it is 2% in the *J*, *H*, and *K* bands. Variation of the monochromatic flux in the *M* band by 5% corresponds to variation of the stellar angular diameter by 2.5%. In the four stars, the *M*-band angular diameter is 4–6% smaller than the *L*-band diameter.

When calculating the effective temperatures and angular diameters for the Sun, we took the monochromatic IR-band fluxes from [16] and took the solar constant to be 1.36×10^6 erg cm^{-2} s^{-1}. Table 4 presents the mean effective temperatures, angular diameters, and radii of the stars. We obtained these effective temperatures by averaging the T_{eff} values for all the IR bands; the angular diameter corresponds to the average T_{eff}, and we calculated the radius from the bolometric magnitude and effective temperature of the star.

Comparison of the mean effective temperatures from Table 4 and the temperatures in Table 1 (determined spectroscopically from the profiles of H_α line wings) shows that the effective temperatures determined using the IR-flux method are, on average, 1.3% lower than the spectroscopic values. However, this discrepancy is no more than 1–2% for all stars except HD 10307, for which it is 3%, with our effective temperature higher than the spectroscopic value. Note that the spectroscopic temperature for this star, which has spectral type G1.5V (5538 K), is anomalously low.

For half the stars, the temperature difference is less than 1%. For the Sun, this difference is 54 K; i.e., less than 1%. Since the accuracies of the IR-flux and spec-

Table 3. Angular diameters (mas) and effective temperatures (K) for the program stars and Sun

HD	θ_J	T_J	θ_H	T_H	θ_K	T_K	θ_L	T_L	θ_M	T_M
1835	0.447	5723	0.462	5630	0.463	5624	0.454	5698		
10307	0.890	5707	0.875	5756	0.866	5785	0.899	5678	0.897	5685
11131	0.394	5821	0.401	5770	0.402	5763	0.400	5777		
20630	0.976	5612	0.951	5685	0.963	5650	0.976	5612	0.983	5597
25680	0.565	5802	0.564	5807	0.568	5788	0.568	5788	0.570	5777
28099	0.212	5747	0.211	5761	0.212	5747	0.213	5734		
76151	0.546	5642	0.549	5626	0.548	5631	0.570	5522		
86728	0.735	5657	0.744	5622	0.744	5622	0.738	5645	0.751	5596
89010	0.594	5513	0.580	5579	0.577	5594	0.576	5598	0.583	5565
146233	0.676	5697	0.689	5643	0.683	5668	0.670	5723	0.660	5766
186408	0.536	5722	0.541	5695	0.548	5659	0.565	5573	0.544	5680
186427	0.485	5710	0.494	5657	0.496	5646	0.511	5562	0.491	5675
187923	0.507	5664	0.517	5609	0.517	5609	0.522	5582		
193664	0.501	6017	0.518	5916	0.522	5894	0.534	5828	0.500	6023
213575	0.363	5751	0.373	5673	0.371	5688	0.373	5673		
217014	0.679	5745	0.684	5724	0.689	5703	0.692	5691	0.657	5841
Sun	1923″	5759	1957″	5708	1932″	5745	1949″	5720	1975″	5682

troscopic effective temperatures are 1–2 and 0.5%, respectively, the agreement between the temperatures in Tables 1 and 4 can be considered good.

4. ENERGY DISTRIBUTION AT 3400–7500 Å

We conducted observations at 3400–7500 Å using a spectrophotometer installed on the 60-cm Zeiss-2 reflector of the Crimean Laboratory of the SAI. The spectral resolution was 48.5 Å. We used a diffraction grid with discrete scanning and a photomultiplier operating in a photon-count regime. Studies of the linearity of the amplifier demonstrated its high stability. Deviations from linearity were no greater than 0.5% for a counting rate of 3×10^5 pulses/s.

During the observations, the spectral width of the exit slit was 50 Å; a 27.″5 entrance diaphragm was used. The spectra were recorded in accordance with the following sequence: standard star, program star, background, program star, standard star. The program and standard stars were compared using the equal-altitude method. We accounted for differential extinction using a transparency coefficient determined on each observing night. For this purpose, the spectra of two standard stars with an air-mass difference of no less than 0.5 were recorded several times per night. The observational data were downloaded onto a computer, and the continuous spectra of the standard stars near hydrogen absorption features were constructed in a graphical regime. We calculated the spectral energy distributions using the distributions for the standard stars and the spectral absorption coefficient for the given night. We derived the mean energy distribution for each star using measurements obtained over 2–5 nights, i.e., using 4–10 individual scans, since spectra of the program stars were obtained twice each night.

Due to the inconvenience of considering the energy distribution in the instrumental wavelength system, we recalculated the energy distributions with a 50 Å step, beginning at 3425 Å. We used eight bright stars distributed more or less uniformly over the sky as standard stars: βAri, γOri, βTau, αLeo, ηUMa, αLyr, αAql, and αPeg. These stars served as standards during the compilation of the spectrophotometric catalog [3]. The spectral energy distributions of these stars with a step of 100 Å are presented in [17]; these were obtained via comparison with αLyr, which served as the primary

Table 4. Mean angular diameters, radii, and effective temperature for the program stars and Sun

HD	$\bar{\theta}$, mas	$R/R_\odot$	$\bar{T}_{eff}$, K	HD	$\bar{\theta}$, mas	$R/R_\odot$	$\bar{T}_{eff}$, K
1835	0.456	0.99	5669	89010	0.582	1.89	5570
10307	0.885	1.16	5722	146233	0.676	1.02	5699
11131	0.399	0.99	5783	186408	0.547	1.28	5666
20630	0.970	0.95	5631	186427	0.495	1.13	5650
25680	0.567	1.02	5792	187923	0.516	1.54	5616
28099	0.212	1.00	5747	193664	0.515	0.97	5936
76151	0.553	1.01	5630	213575	0.370	1.42	5696
86728	0.742	1.19	5628	217014	0.680	1.12	5741
Sun	1947″		5723				

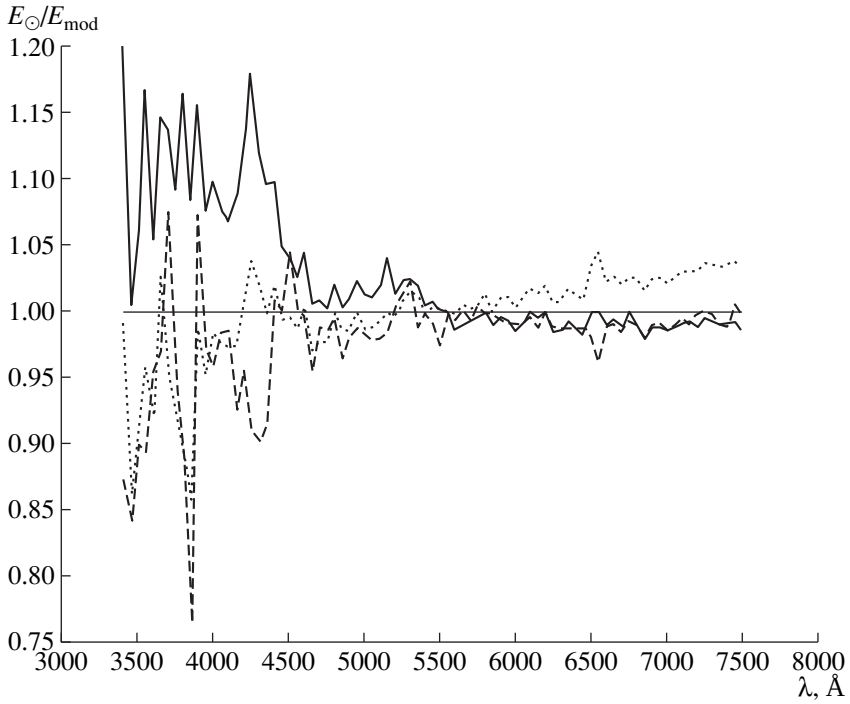

Fig. 1. Ratio of the monochromatic fluxes for the Sun and various models. Solid curve—model T_{eff} = 5750 K, $\log g$ = 4.5; dashed curve—model T_{eff} = 6000 K, $\log g$ = 4.5; dot–dashed curve—solar model T_{eff} = 5770 K, $\log g$ = 4.44.

spectrophotometric standard, using the calibration of Hayes [18]. The spectral energy distributions of the program stars in the interval 3425–7525 Å with step 50 Å are presented in [7].

5. COMPARISON WITH SOLAR AND THEORETICAL MODELS

We carried out a comparison with the theoretical models of Kurucz [14] in the interval 3425–7525 Å and in the infrared at the effective wavelengths for the *JHKLM* photometric system. In the interval 3425–7525 Å, the emitted fluxes for the model grid of Kurucz are calculated with a step of 2 nm. Since the observations had a spectral resolution of 50 Å, the investigated spectral interval was divided into 50 Å subintervals (3400–3450 Å, etc.), and the emitted fluxes for the model were summed with steps of 10 Å within each subinterval and then averaged. The resulting values for the emitted flux were assigned to the middle of the subinterval (3425 Å, 3475 Å, etc.).

We normalized both the observed energy distributions E_* and $E_\odot$ and the emitted fluxes for the Kurucz models to a wavelength of 5575 Å. The minimum mean deviations from the solar spectral energy distribution did not exceed 1.5% for BS 483, BS 88, BS 6060, BS 7783, and HD 213575. However, for BS 88 and BS 6060, the deviations at wavelengths shorter than 4000 Å were more substantial and reached 6–10%.

The best agreement with the theoretical model T_{eff} = 5750 K, $\log g$ = 4.5 in the wavelength interval 4400–7500 Å was obtained for BS 7503 and BS 7504 (16 Cyg A and 16 Cyg B). The mean deviations of the monochromatic fluxes of these stars from the model spectra do not exceed 1.01, although they reach 10% in some sections of the ultraviolet. For BS 6060, the mean deviation is 1.02, and 3600 Å E_*/E_{mod} reaches 1.2 near 3600 Å.

Figure 1 presents the ratios $E_\odot/E_{mod}$ for models with $\log g$ = 4.5 and T_{eff} = 5750 K (solid curve) and 6000 K (dotted curve), and with $\log g$ = 4.44 and T_{eff} = 5770 (dot–dashed curve). We took the solar spectral energy distribution from [16].

Figures 2 and 3 present the ratios $E_*/E_\odot$ and E_*/E_{mod} for BS 7504 (16 Cyg B) and BS 6060 (18 Sco). This latter star is currently considered to be the closest analog to the Sun. Figures 1–3 show the ratios for models with T_{eff} = 5750 K, $\log g$ = 4.5, T_{eff} = 6000K, $\log g$ = 4.5, and T_{eff} = 5770 K, $\log g$ = 4.44. The model grid of Kurucz is calculated with steps of 250 K in effective temperature and 0.5 in $\log g$; a T_{eff} = 5770 K, $\log g$ = 4.44 model was calculated for the Sun.

We can see that the theoretical model T_{eff} = 5750 K, $\log g$ lies below the observational data for both stars in the ultraviolet, since $E_*/E_{mod} > 1$. For T_{eff} = 6000 K and $\log g$ = 4.5, the theoretical models exceed the observed

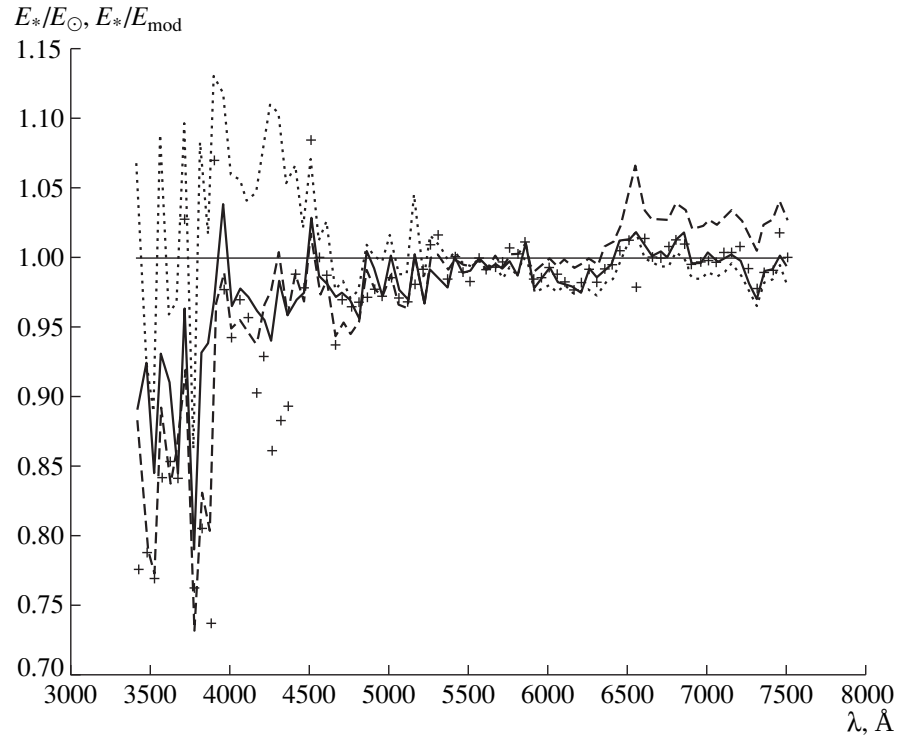

Fig. 2. Ratio of the monochromatic fluxes for BS 7504 (16 Cyg B) and the Sun (solid curve); 16 Cyg B and the model T_{eff} = 5750 K, $\log g$ = 4.5 (dotted curve); 16 Cyg B and the model T_{eff} = 6000 K, $\log g$ = 4.5 (dash–dot curve); and 16 Cyg B and the solar model 5770 K, $\log g$ = 4.44 (crosses).

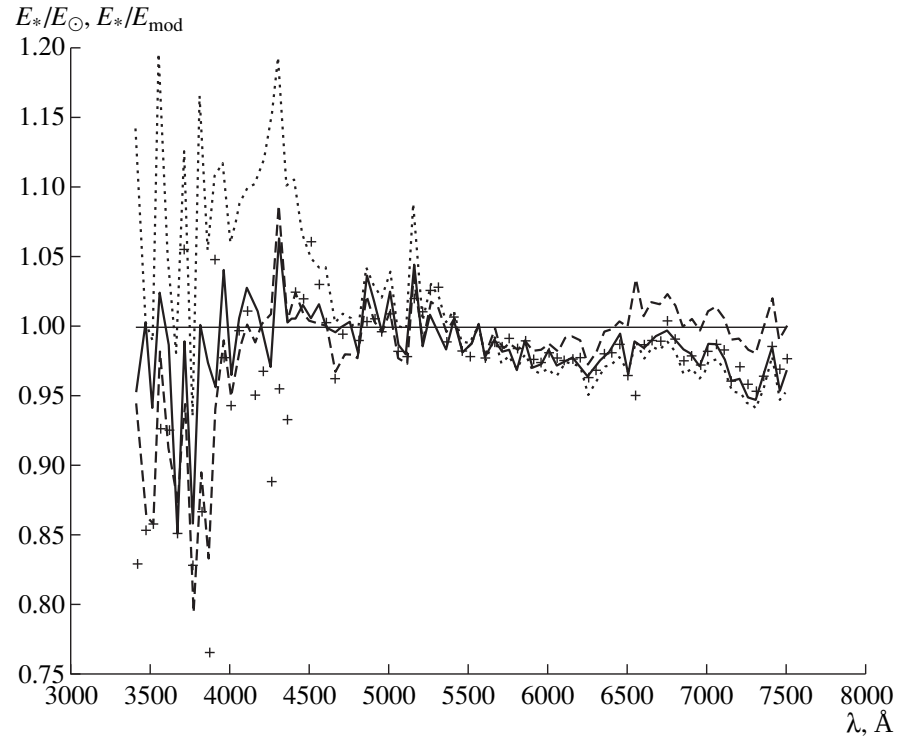

Fig. 3. Same as in Fig. 2 for BS 6060 (18 Sco).

Table 5. Infrared color indices for the program stars and Sun

HD	*V–J*	*J–H*	*H–K*	*K–L*	*K–M*
1835	1.11	0.38	0.07	−0.04	−0.04
10307	1.06	0.32	0.04	0.10	0.02
11131	1.19	0.34	0.07	0.01	
20630	1.14	0.30	0.09	0.05	−0.01
25680	1.13	0.30	0.08	0.02	−0.03
28099	1.19	0.30	0.08	0.02	
76151	1.16	0.31	0.07	0.10	
86728	1.17	0.33	0.07	0.00	−0.02
89010	1.19	0.30	0.06	0.02	−0.04
146233	1.11	0.34	0.05	−0.02	−0.11
186408	1.10	0.32	0.10	0.08	−0.06
186427	1.13	0.34	0.08	0.08	−0.06
187923	1.15	0.34	0.07	0.04	
193664	0.99	0.33	0.07	0.07	−0.11
213575	1.21	0.36	0.06	0.03	
217014	1.08	0.31	0.09	0.03	−0.14
Sun [19]	1.144	0.333	0.043	0.043	0.012
Sun [20]		0.36	−0.03	0.02	0.02
Sun [21]		0.34	0.02		

values. In the interval 3400–4000 Å, the solar spectral energy distribution lies above the distributions for both stars, but the distribution for BS 6060 shows a good agreement with the solar distribution and with the model with T_{eff} = 6000 K beginning at 4000 Å. The observed energy distribution for BS 6060 is in good agreement with the model T_{eff} = 6000 K, $\log g$ = 4.5 in the red part of the spectrum.

For BS 7504, $E_*/E_{\rm mod} > 1$ in the red part of the spectrum for the model T_{eff} = 6000 K, $\log g$ = 4.5; i.e., the observed energy distribution lies above the theoretical distribution. The energy distribution for this star in the red is in better agreement with the model T_{eff} = 5770 K, $\log g$ = 4.44.

Table 5 presents the IR color indices for the program stars and the Sun. We took the solar color indices from Bessel and Brett [19], Kharitonov and Knyazeva [20], and Colina *et al.* [21]. All the color indices were obtained via synthetic photometry; we used the solar spectral energy distributions obtained by Labs and Neckel [22], Makarova *et al.* [23], and Wamsteker [24] for the first, second, and third color indices, respectively.

For most of the stars, *H–K* and *K–L* are 0.05–0.10, while the corresponding values for the Sun obtained in the same three studies [22–24] lie in the range from –0.03 to 0.043. *H–K* for BS 6060 (18 Sco) is close to the solar value indicated by the data of [19].

Table 6. Ratios of the fluxes in the *H*, *K*, *L*, and *M* bands to the *J*-band flux for the program stars, Sun, and theoretical models (T_{eff}/log *g*)

HD	*H*	*K*	*L*	*M*
1835	0.542	0.199	0.0298	0.00992
10307	0.513	0.183	0.0312	0.00962
11131	0.524	0.192	0.0301	
20630	0.504	0.188	0.0306	0.00962
25680	0.504	0.186	0.0294	0.00935
28099	0.503	0.187	0.0296	
76151	0.507	0.186	0.0319	
86728	0.518	0.189	0.0295	0.00860
89010	0.501	0.183	0.0288	0.00909
146233	0.523	0.187	0.0287	0.00877
186408	0.513	0.193	0.0323	0.00945
186427	0.521	0.193	0.0323	0.00944
187923	0.524	0.192	0.0309	
193664	0.518	0.191	0.0316	0.00895
213575	0.532	0.193	0.0309	
217014	0.509	0.189	0.0304	0.00862
model 6000/4.5	0.484	0.177	0.0289	0.00890
model 5750/4.5	0.504	0.184	0.0291	0.00919
model 5500/4.5	0.529	0.192	0.0305	0.00948
model 5770/4.44	0.523	0.201	0.0317	0.00985
Sun [21]	0.506	0.178	0.0299	0.00993
Sun [16]	0.523	0.177	0.0307	0.0102

In the infrared, the emitted fluxes for the model grid of Kurucz are presented in steps of 10 nm, and the effective wavelengths for the *JHKLM* bands lie at the centers of these intervals; i.e., the models specify the emitted fluxes at wavelengths 1245, 1255, etc. Therefore, the emitted flux at 1250 nm (1.25 μm) is the mean of the fluxes at 1245 and 1255 nm. Table 6 presents the ratios of the fluxes in the *H*, *K*, *L*, and *M* bands to the flux in the *J* band for the program stars, Sun, and models. The data in this table provide a basis to judge how well the solar spectral energy distribution agrees with the models T_{eff} = 5750 K, $\log g$ = 4.5 and T_{eff} = 5770 K, $\log g$ = 4.44; which stars have effective temperatures and gravitational accelerations closest to the solar values; and how well the IR-band flux ratios for the models and the Sun agree with those for the program stars, especially the best candidates for solar "twins"—HD 186408 (16 Cyg A), HD 186427 (16 Cyg B), HD 146233 (18 Sco), and HD 217014 (51 Peg).

Below, we present the ratios of the fluxes in the *H*, *K*, *L*, and *M* bands (relative to the *J*-band flux) for these

four stars to the corresponding ratios for the Sun [16] and the model T_{eff} = 5750 K, $\log g$ = 4.5:

	H		*K*		*L*		*M*	
	*/⊙	*/mod	*/⊙	*/mod	*/⊙	*/mod	*/⊙	*/mod
16 Cyg A	0.981	1.02	1.09	1.05	1.05	1.11	0.926	1.03
16 Cyg B	0.996	1.03	1.09	1.05	1.05	1.11	0.925	1.03
18 Sco	1.00	1.04	1.06	1.02	0.935	0.986	0.860	0.954
51 Peg	0.973	1.01	1.07	1.03	0.990	1.04	0.845	0.938
Sun	–	1.04	–	0.962	–	1.05	–	1.11

In the last line, we present the corresponding ratios for the Sun and the model T_{eff} = 5750 K, $\log g$ = 4.5. The same ratios of the relative fluxes of the four program stars and the Sun to the corresponding ratios for the model T_{eff} = 5770 K, $\log g$ = 4.44 are

	H	*K*	*L*	*M*
16 Cyg A	0.981	0.960	1.02	0.959
16 Cyg B	1.00	0.960	1.02	0.958
18 Sco	1.00	0.930	0.905	0.890
51 Peg	0.973	0.940	0.959	0.875
Sun	1.00	0.881	0.968	1.04

In nearly all cases, these IR-band flux ratios for the stars and the Sun are larger than the ratios for the model T_{eff} = 5750 K, $\log g$ = 4.5, by 1–5% in the *H* and *K* bands and by 3–11% in the *L* and *M* bands, where the accuracy is somewhat lower. For the model T_{eff} = 5770 K, $\log g$ = 4.44, the relative fluxes in the *K* and *M* bands exceed the corresponding values for all the stars, and the *H*-band values for 16 Cyg A, 18 Sco, and the Sun are in good agreement. The *L*-band values are lower than the model only for 16 Cyg A and 16 Cyg B 2% and are higher than the model for the remaining stars and the Sun.

A comparison of the fluxes for the candidate solar analogs and the Sun indicates that the *H*- and *M*-band fluxes for the stars are lower than those for the Sun, while the *K*-band fluxes are higher. The *L*-band fluxes for 16 Cyg A and 16 Cyg B are 5% higher, and the *L*-band flux for 18 Sco is 6% lower. The ratio of the fluxes in this band for 51 Peg and the Sun is close to unity.

6. CONCLUSION

The effective temperatures derived from the IR fluxes of the program stars using observations in the *JHKLM* photometric bands and temperatures determined from analyses of hydrogen-line profiles agree to within 1–2%, consistent with the accuracy of the IR-flux method.

The diameters of four stars—16 Cyg A, 16 Gyc B, BS 7783, and 51 Peg—increase with IR wavelength. This could be due to the presence of additional absorption in gas or dust envelopes around these stars. The angular diameter of the Sun does not show such a dependence.

Comparison of the fluxes in various IRs band relative to the *J*-band flux for the program stars and Sun with theoretical Kurucz models shows that, for most of the stars and for the Sun, the observed IR fluxes are higher than the fluxes for models with T_{eff} = 5750 K and $\log g$ = 4.5, by 1–5% in the *H* and *K* bands and by 3–11% in the *L* and *M* bands. The opposite is observed for models with T_{eff} = 5770 K and $\log g$ = 4.44: The observed fluxes in the *K*, *L*, and *M* bands are lower than the theoretical values by 3–11%, while the observed and theoretical fluxes are nearly equal in the *H* band. The *K*-band fluxes for the program stars were higher, and the *H*- and *M*-band fluxes lower than those for the Sun. In the *H* and *K* bands, where the measurement accuracy is higher, the differences between the fluxes for the stars and the Sun, and also for the stars and both models, do not exceed 5%.

High-accuracy measurements of the parallaxes of the program stars using data from the Hipparcos astrometric satellite made it possible to determine the bolometric magnitudes of the stars to high accuracy. Most of the program stars (13 of 16) have higher luminosities than the Sun. These 13 stars include all the best candidates for solar "twins": 16 Cyg A, 16 Cyg B, 18 Sco, and 51 Peg. The bolometric magnitude of 18 Sco is only 0.06 lower than the solar value, which is 4.75. As a consequence of their higher luminosities, 16 Cyg A, 16 Cyg B, ad 51 Peg cannot be considered fully analogous to the Sun.

ACKNOWLEDGMENTS

This work was supported by an "Astronomy" grant from the Ministry of Science and Technology of the Russian Federation (project 1.4.1.3).

REFERENCES

1. G. Cayrel de Strobel, Astron. Astrophys. Rev. **7**, 243 (1996).
2. G. Cayrel de Strobel, *Hipparcos and Tycho Catalogues* ESA SP-1200 (1997).
3. I. B. Voloshina, I. N. Glushneva, V. T. Doroshenko, *et al.*, *Spectrophotometry of Bright Stars*, Ed. by I. N. Glushneva (Nauka, Moscow, 1982).
4. I. N. Glushneva, E. A. Makarova, and A. V. Kharitonov, Highlights Astron. **7**, 853 (1986).
5. V. G. Kornilov, I. M. Volkov, A. I. Zakharov, *et al.*, Tr. Gos. Astron. In-ta im. P.K. Shternberga **63** (1991).
6. I. N. Glushneva, Astron. Zh. **71**, 652 (1994).
7. I. N. Glushneva, G. V. Borisov, V. I. Shenavrin, *et al.*, Astron. Astrophys. Trans. **18**, 633.
8. *Solar Analogs: Characteristics and Optimum Candidates*, Ed. by J. Hall (Lowell Observatory, 1998), p. 182.

9. G. Cayrel de Strobel and E. D. Friel, *Solar Analogs: Characteristics and Optimum Candidates*, Ed. by J. Hall (Lowell Observatory, 1998), p. 93.
10. A. É. Radzhip, V. I. Shenavrin, and V. G. Tikhonov, Tr. Gos. Astron. In-ta im P.K. Shternberga **58**, 119 (1986).
11. H. L. Johnson, R. I. Mitchell, B. Iriarte, *et al.*, Comm. Lunar Planet Lab. **63**, 99 (1996).
12. J. Koornneef, Astron. Astrophys., Suppl. Ser. **51**, 489 (1983).
13. D. E. Blackwell and M. J. Shallis, Mon. Not. R. Astron. Soc. **180**, 177 (1977).
14. R. L. Kurucz, *CD ROM 13* (1993).
15. I. N. Glushneva, Astron. Zh. **60**, 560 (1983).
16. E. A. Makarova, A. V. Kharitonov, T. V. Kazachevskaya, *et al.*, Balt. Astron. **7**, 467 (1998).
17. I. N. Glushneva, A. V. Kharitonov, L. N. Knyazeva, and V. I. Shenavrin, Astron. Astrophys., Suppl. Ser. **92**, 1 (1992).
18. D. S. Hayes, *Calibration of Fundamental Stellar Quantities*, Ed. by D. S. Hayes, L. E. Pasinetti, and A. G. Philip (Reidel, Dordrecht, 1985), p. 225.
19. M. S. Bessel and J. M. Brett, Publ. Astron. Soc. Pac. **100**, 1134 (1988).
20. A. V. Kharitonov and L. N. Knyazeva, Izv. VUZ (Radiofizika) **39** (10), 1234 (1996).
21. L. Colina, R. C. Bohlin, and F. Castelli, Astron. J. **112**, 307 (1996).
22. D. Labs and H. Neckel, Zeits. Astrophys. **69**, 1 (1968).
23. E. A. Makarova, A. V. Kharitonov, and T. V. Kazachevskaya, *Solar Radiation Flux* (Nauka, Moscow, 1991).
24. W. Wamsteker, Astron. Astrophys. **97**, 329 (1981).

Translated by D. Gabuzda

Astronomy Reports, Vol. 44, No. 4, 2000, pp. 255–261. Translated from Astronomicheskiĭ Zhurnal, Vol. 77, No. 4, 2000, pp. 295–302.

Solar Flares with Long Soft X-ray Decays: Energy Balance in Giant Loops

K. V. Getman and M. A. Livshits

Institute of Terrestrial Magnetism, Ionosphere, and Radiowave Propagation, Russian Academy of Sciences, Troitsk, Moscow oblast, 142092 Russia

Received April 24, 1999

Abstract—Solar flares with long X-ray decays (Long-Decay Flars, LDF) are studied. X-ray and radio observations can be used to trace the active phase of an LDF and the subsequent development of a system of giant coronal loops. The energy balance in a giant loop is modeled for the events of January 24, 1992 (an elementary LDF, considered earlier), November 2, 1991, and March 15, 1993; the modeling shows that energy flow into the loop over the entire life time of the LDF is necessary to account for the duration of the events. The total energy of the LDF was confined within rather narrow limits and was comparable to the energy of major impulsive flares. The results are consistent with the concept (developed in connection with *Yohkoh* observations) that an LDF in a posteruptive process results in magnetic reconnection in a vertical current sheet, with the subsequent formation of new loops and their specific evolution. *© 2000 MAIK "Nauka/Interperiodica".*

1. INTRODUCTION

Recent observations and theoretical studies have demanded some revision of our general ideas about the development of the physical processes in solar flares and the classification of such flares. Impulsive flares (or the corresponding phase of complex phenomena) can easily be distinguished; these correspond to processes in very low loops, usually adjacent to sunspots. During any flare, appreciable masses of hot gas fill one or several high coronal loops. In an impulsive flare, the duration of the soft X-ray emission is determined primarily by radiative losses; accordingly, the decay timescale of this emission t_{rad} is $3kT/nL(T)$, where $L(T)$ is the radiative cooling function of an optically thin plasma. Pallavicini *et al.* [1] drew a similar conclusion about the behavior of the X-ray light curves for flares on active red dwarfs, most of which are impulsive. The total duration t_b of a soft X-ray flare from its onset to the decay of the maximum intensity by an order of magnitude is $2.3t_{rad}$; for impulsive flares on the Sun, this is 1–10 min. We are able to derive the physical conditions in coronal flare loops, for example, from the data in the two channels of the GOES satellites. Knowledge of t_{rad} allows us to apply the above formal criterion and resolve the question of whether particular phenomena correspond to impulsive flares.

A rather large number of solar flares have long durations. In many of these events—which, as a rule, develop in the corona—the growth of the X-ray intensity and its subsequent decay proceed slowly. Nonstationary events characterized by a very slow decay of the soft X-ray emission were first identified in 1977 by Kahler [2]. We will term such nonstationary events with a long soft X-ray decay Long-Decay Flares (LDFs). Note that both impulsive and slow flares accompanied by the development of major loop systems in the corona are often homologous; i.e., within the same region, there emerge series of either impulsive or slow flares with similar temporal and spatial characteristics. The homology of nonstationary phenomena is associated with peculiarities of the structure and, in part, with the development of the magnetic fields in the active region hosting the phenomena. As an example, we note here a series of four LDFs that took place in March 1993, in the group NOAA 7440, on March 2 (maximum 21 : 07, X-ray class M 5.1), March 6 (20 : 33, M 7.7), March 12 (18 : 20, M 7.0), and March 15 (20 : 45, M 2.9).

X-ray observations of the large arches that form during solar flares have been carried out on the *Skylab*, *SMM*, and *Yohkoh* spacecraft. These data have been analyzed in many studies, in particular, those carried out by the team headed by Z. Švestka [3–5]. The large interest in these problems that has arisen recently is connected with two circumstances.

First, the *Yohkoh* observations led to a big step forward in our understanding of the physical nature of slow solar flares. Models in which an ejection of plasma results in an open, large-scale dipole-type, magnetic configuration were confirmed observationally. The subsequent return of the configuration to a system of closed loops results in reconnection of magnetic lines in a vertical current sheet. This is the source of the primary energy release in slow flares. The main aspects of these ideas were developed in [6–8].

Second, detailed studies of both the soft and hard X-rays generated during slow flares on active late-type stars (red dwarfs and subgiants) in RS CVn binary sys-

1063-7729/00/4404-0255$20.00 © 2000 MAIK "Nauka/Interperiodica"

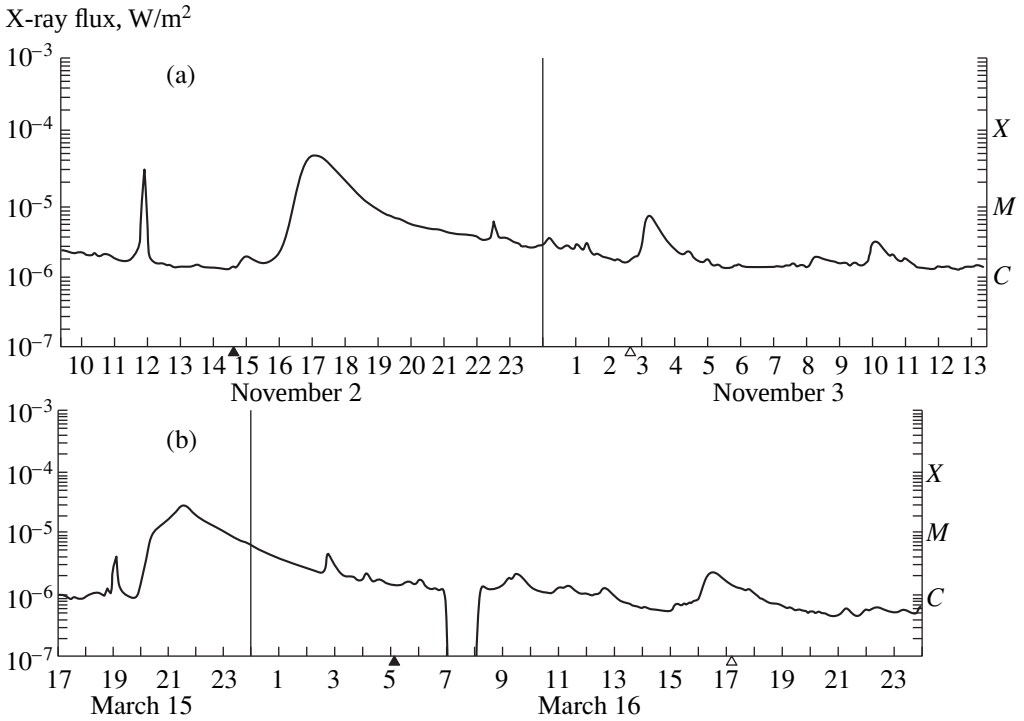

Fig. 1. Variations of the X-ray flux in the 1–8 Å band according to GOES data for the events of (a) November 2, 1991 and (b) March 15, 1993.

tems have recently begun. The *Beppo-SAX* satellite detected X-ray emission with photon energies exceeding 100 keV in such systems [9]. These facts all suggest that the formation of systems of large flare arches in slow flares on both stars and the Sun is responsible for flares of soft X-ray emission lasting from several hours to a day [10].

Below, we will separate out the class of LDFs, consider X-ray observations of LDFs, and numerically simulate the energy balance in the source of the prolonged soft X-ray emission. In conclusion, we discuss the physics of the processes taking place in LDFs.

2. X-RAY OBSERVATIONS OF LDFS

We began our study of the evolution of well developed giant loops using the well-known event of January 24–25, 1992, as an example, treating it as an elementary slow flare [11]. We consider the entire class of LDFs:

(1) elementary phenomena;

(2) events lasting one to two hours: flares with a cusp similar to the well-known event of February 21, 1992, which was observed by *Yohkoh* [12] (this class of event is related to usual two-ribbon flares);

(3) phenomena with the development of typical systems of large arches, such as those observed on November 2, 1991, March 15, 1993, etc. [3];

(4) major flares with complex spatial and temporal structures, in which very large systems of giant loops existing from 0.5–1 day are observed (for example, the white light flare of June 15, 1991, which exhibited powerful impulsive and post-eruptive phases).

To a first approximation, these cases differ in the maximum temperatures at the top of the giant loop, which varies for various LDFs from 6 to 25 million K.

The duration of the soft X-ray emission accompanying a flare seldom exceeds three hours. Several such flares were studied in activity cycle 21, and most of the LDFs that took place in cycle 22 were studied in [3–5]. There are also X-ray observations of about ten weak events, most of which are considered in [5]. Some of these are accompanied by the formation or restoration of small streamer-type structures; we performed numerical simulations of one such event in [11].

Of major interest for our analysis are events accompanied by the formation of systems of giant coronal loops. These X-ray arches frequently ascend at a constant velocity [3]; occasionally, this velocity is very low [4] or changes with time in a complex manner. We chose two well-known events observed by *Yohkoh* for further study and numerical simulations.

The first event is the flare of November 2, 1991, which had magnitude 1N in the optical and M 4.8 in the X-ray, with coordinates S 07 W 69. The impulsive event began at 16 : 19 UT, with the maximum of the gamma-ray burst at 16 : 35 UT. The maximum burst intensity at 6 cm reached 135 sfu [13]. The soft X-ray emission grew slowly (Fig. 1a), and the decay of the emission lasted about half a day. The time run of the temperature

and density in the soft X-ray source could be derived from the ratio of the fluxes in the 0.5–4-Å and 1–8-Å channels of the *GOES* satellite [3, Fig. 1].

The second event took place on March 15, 1993, and is a well-known limb flare S04 W90 with X-ray magnitude M 2.9. A large system of loops was recorded in ground-based and space (*Yohkoh*) data, beginning from approximately 22 h on March 15 to 6 h on March 16, 1993. Figure 1b shows the X-ray burst, with a gradual growth and slow decay of the emission. The times 21 : 20 and 21 : 25 UT, when type III radio outbursts were recorded, have prominent X-ray fluxes (all information from the Solar Geophysical Data [13]; see also [3]). The maximum temperature of the loop top at the burst maximum was close to 2×10^7 K [14]. According to the X-ray and radio data [14, 15], harder emission was observed for approximately 30 minutes in the cusp region. The parameters of the system of giant loops are similar to those for the loop observed on February 21–22, 1992 [12].

The first stage of an LDF probably represents its active phase. In [11], we showed that, in the elementary LDF of January 24–25, 1992, the formation of each new loop was accompanied by a type III radio outburst, providing evidence for particle acceleration in each of the individual acts of energy release. After reconnection in a vertical current sheet and formation of a new loop, the loop is compressed in a very specific manner (the shrinkage effect [8]). In more powerful LDFs, the ejection of a plasmoid from the reconnection region into interplanetary space probably gives rise to type II and IV radio outbursts, as, for example, during the flares of March 6 and 12, 1993, noted above [13].

In specific events, the active phase of an LDF can last from half an hour to several hours. The development of this phase depends on several factors, such as the distance of the main LDF loops from the initial flare site (most frequently, a large sunspot or group of sunspots) where the impulsive processes developed. The character of particle acceleration during the active phase of an LDF depends appreciably on the existence of an impulsive phase and the particle-acceleration mechanism operating in it.

The presence of an impulsive phase and the associated acceleration of charged particles affect the maximum temperature in the soft X-ray source but do not strongly influence the subsequent development of the giant loops. Both the formation of plasma in the form of a giant arch (or arches) and most of its heating occur during the active phase of an LDF.

After the active phase, the gradual development of one or several giant loops begins. These loops radiate X-rays over a very long time and extend this second phase of the LDF to many hours. The origin of the hot plasma and its soft X-ray emission over 3–12 hours remains unknown.

3. NUMERICAL SIMULATIONS OF THE ENERGY BALANCE IN A GIANT LOOP

The prolonged X-ray emission results from the development of giant postflare loops and the specific nature of the energy balance in them. The energy balance in high coronal loops has been investigated analytically in a number of earlier studies. Here, we should mention the first work of Svestka [16] and some other works collected in the review [17]. In addition, an analytical treatment of a prolonged stellar flare that also included transients was recently carried out in [10]. Unfortunately, these analyses have required additional assumptions (for example, only radiative losses or only thermal conduction have been taken into account), and it is not always clear what timescales should be used to describe changes in various parameters of the LDF. High-quality observations of slow flares on the Sun have required new analyses to study the prolonged existence of soft X-ray emission in the events considered.

As in [11], we base our analysis on numerical simulations of the gas–dynamical processes in a coronal loop already generated during the active phase of an LDF. In the elementary slow event we considered in [11], a huge loop emerged after the formation and subsequent evolution of two loops (after 12 h on January 24, 1992). The maximum temperature in the source is usually reached at the time of the giant loop's formation. Therefore, in our simulations, we chose the heating rate so that the time when the maximum temperature was reached in the calculations coincided with the observed time.

We solved the same set of gas–dynamical equations as in [11] for a loop with slowly changing gravity with height

$$\frac{\partial v}{\partial t} = -\frac{\partial p}{\partial s} - g,$$

$$\frac{\partial}{\partial t}\left(\frac{1}{n}\right) = m_p \frac{\partial v}{\partial s},$$

$$\frac{\partial \varepsilon}{\partial t} = -p\frac{\partial v}{\partial s} - \frac{\partial W}{\partial s} - Q_{rad} + H,$$

where s and z are Lagrangian and Euler coordinates, $ds = nm_p dz$, v is the velocity, p is the pressure, m_p is the mass of the proton, $g(s)$ is gravity, $\varepsilon = 3kT/m_p$ is the internal energy density, Q_{rad} and H are the radiative losses and heating per unit mass of plasma, and W is the heat flux.

This calculation differs from that in [11] mainly in the way in which the initial model is chosen. Here, for calculations with a large amount of heating, our initial model was an isothermal loop with a hydrostatic density distribution in which the radiative losses are balanced by some source of heating operating only at the initial time. As in [11], we found a solution for a fixed temperature at the feet of the loop. For the event of

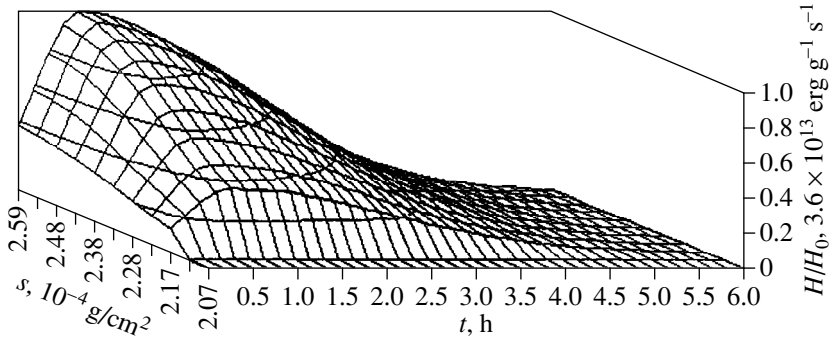

Fig. 2. Heating H/H_0 as a function of the Lagrangian coordinate and time for $t_1 = t_2 = 40$ min for $t < 40$ min and $t_1 = 2.5$ h, $t_2 = 40$ min for $t \geq 40$ min for the event of March 15, 1993. The maximum of the Lagrangian coordinate corresponds to the loop top.

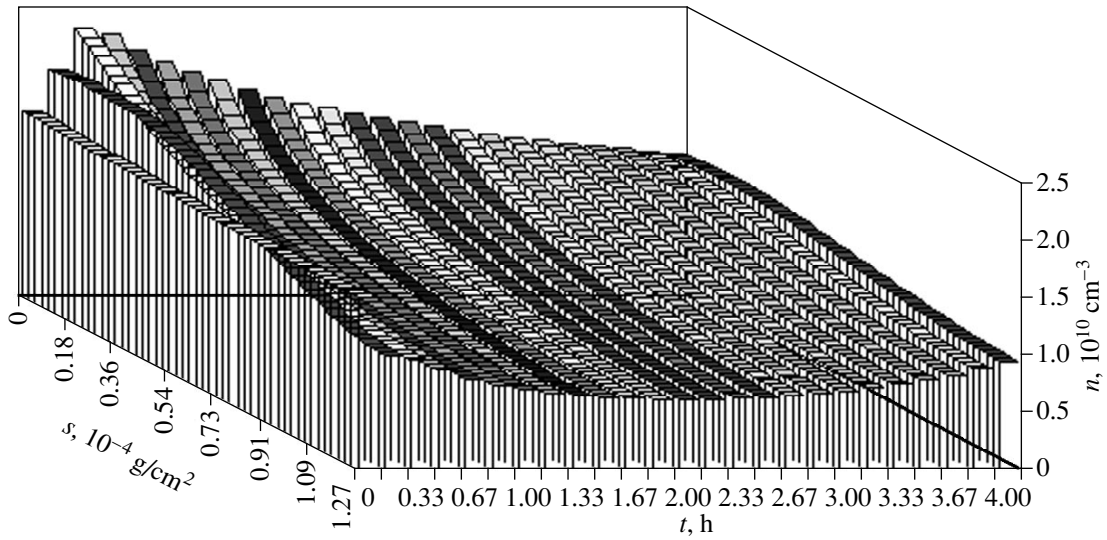

Fig. 3. Density distribution from the loop feet to its top for various times during the event of November 2, 1991. Note the transition from the dynamic to the quasi-stationary regime.

March 15, 1993, when radiative cooling of the plasma at the loop feet resulted in a sharp decrease of the temperature at the very beginning of the process, we introduced a small amount of additional heating to partially compensate the cooling of this region. At subsequent times, the heat flux from the main region of heating at the loop top determined the behavior of the temperature throughout the loop.

Here, we used the same form for the heating function

$$H = H_0 \exp\left(-\left[\frac{s - s_m}{s_1}\right]^2\right)\exp\left(-\left[\frac{t - t_2}{t_1}\right]^2\right),$$

where s_m is the Lagrangian coordinate of the loop top, s_1 is the characteristic heating scale in terms of the mass coordinate, and t_1 is the heating timescale. The timescale t_1 can take on various values, changing when the heating is maximum; i.e., the function H is asymmetric with respect to time. As an example, Figure 2 shows the heating function $H(s, t)$ we used.

For the event of November 2, 1991, we estimated the density from the known emission measure at the burst maximum EM $\approx 8 \times 10^{49}$ cm^{-3}, projected area of the X-ray source, and its length along the line of sight, which we took to be equal to its projected size along the limb. This yielded the estimate $n = (1–3) \times 10^{10}$ cm^{-3}. Further, we varied the density in the calculations, and finally chose for this event $n = 1.5 \times 10^{10}$ cm^{-3} at the loop feet at the initial time. For the event of March 15, 1993, the density was twice this value.

For the event of November 2, 1991, our numerical simulation with a heating-growth period of 20 min and a decay over two hours yielded the evolution of the loop density profile shown in Fig. 3. The heating growth induces motions with velocities of a few km/s in the source (Fig. 4), which redistribute the density in the loop. At subsequent times, the motions are damped, and

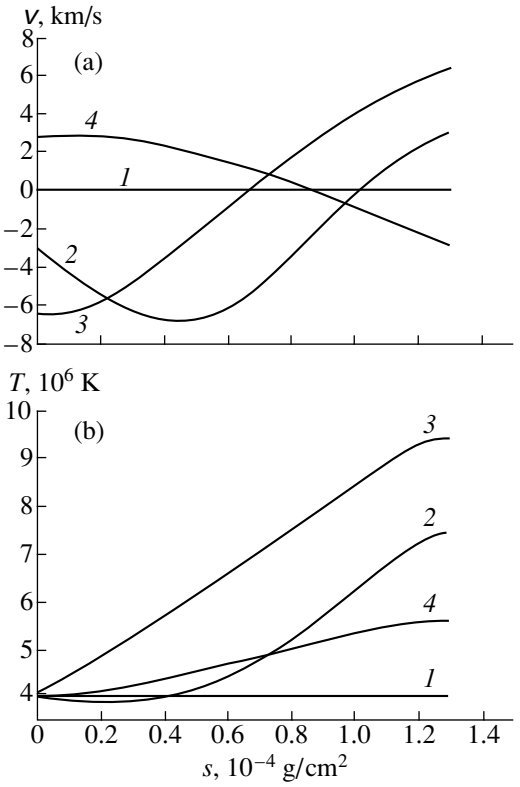

Fig. 4. Distributions of (a) velocity and (b) temperatures for various times during the event of November 2, 1991: (*1*) initial model, (*2*) $t = 10$ min, (*3*) $t = 20$ min, (*4*) $t = 3$ h 40 min from the moment of the heating turn-on.

the density profile varies very slowly (Figs. 3, 4). If we consider, as in [11], much lower densities, the first, dynamic, part of the process and the second, quasi-static, part become more pronounced; in particular, the velocities of motions are virtually zero during the second part of the process.

Figure 4 also shows the temperature distribution along the loop. For the densities considered, radiative losses predominate over dissipation of the heat flux; this determines the corresponding curves and the time when the process terminates as the heating is diminishing. Note that the half-length of the (semicircular) loop reaches a maximum value of 120000 km two hours after the onset of heating.

A comparison of the observed and calculated temperature runs for November 2, 1991, is presented in Fig. 5. We can see that, with the heating rate chosen, the observed loop emission can be maintained for about three hours. The lifetime of the source is limited by the radiative losses. In reality, plasma evaporation from the loop feet, and even weak magnetic forces, begin to accelerate the loop outward, while the temperature is maintained at a level of $(5–6) \times 10^6$ K for several hours.

Our simulation of the event of March 15, 1993, when the temperature at the maximum reached 2×10^7 K, yields similar results. In particular, the time dependence of the temperature (Fig. 6a) shows that the observed loop emission (Fig. 1b) can be explained by a rather weak (typical for such events) change of the emission measure with time. Certainly, for this more

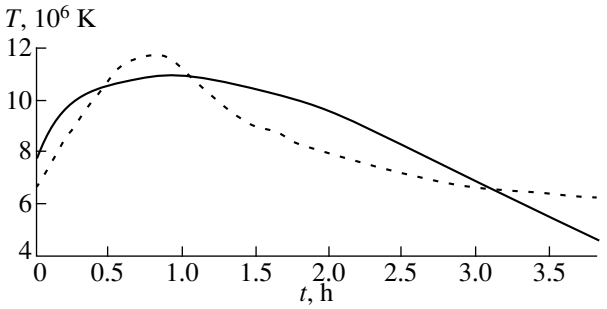

Fig. 5. Comparison of the observed (dashed curve) and calculated (solid curve) temperature runs for the event of November 2, 1991.

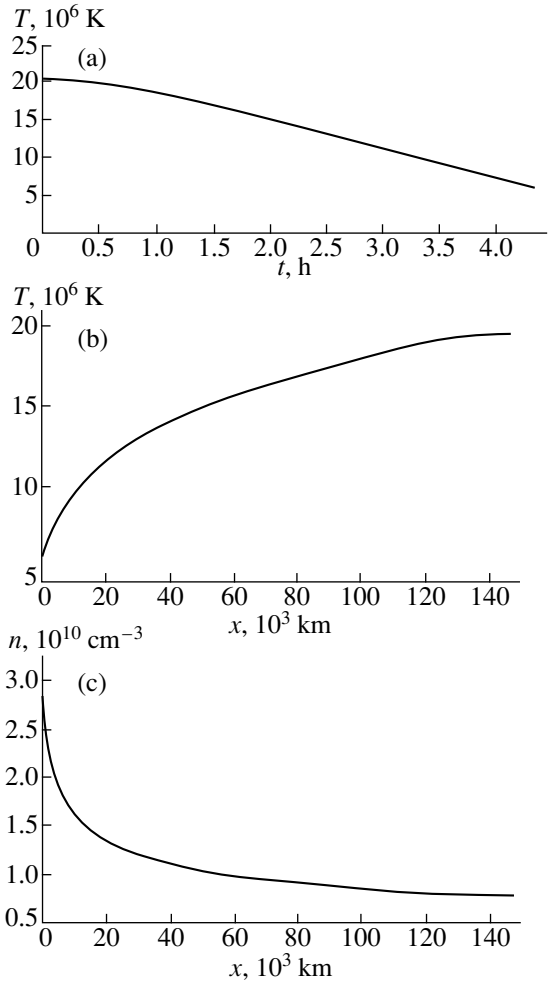

Fig. 6. Calculated time dependence of the (a) temperature and distributions of the (b) temperature and (c) density along the loop at the time of maximum heating for the event of March 15, 1993.

Table

Event	ε, erg cm^{-2} s^{-1}	E, 10^{11} erg cm^{-2}	$\mathscr{E}$, 10^{31} erg
Jan. 24, 1992	4.6×10^7	5	0.25
Nov. 2, 1991	2.1×10^8	75	1.5
Mar. 15, 1993	1.1×10^9	54	2.7
Feb. 16, 1986	1.5×10^9	50	2.5

powerful event, we must choose a different heating function (Fig. 2) than for the weaker events indicated above. The density and temperature distributions along the loop at the time of maximum heating are shown in Figs. 6b and 6c. The densities here are consistent with the observed emission measure at the end of the event. In our simulation, the loop half-length exceeds 180000 km (in the figure, we show only part of the loop, without the top); i.e., the height of the loop top is close to 120000 km. This means that, in the presence of sufficient heating near the loop top, the gas–dynamical equations alone yield solutions corresponding to the loop's rise to such heights.

The energy estimates in cases for which we numerically simulated the energy balance are listed in the table. Note that, in the case of the February 16–17, 1986, event, we consider prolonged emission in the Ca XIX 3.176 Å line (i.e., in a somewhat harder band [18] than the *GOES* data used for other events), so that the heating of plasma by accelerated particles can make a slightly larger contribution to the energy balance. The table contains the dates of the events, energy fluxes ε to the upper part of the loop, energy E that has passed through one cm^2 over the entire LDF, and the energy $\mathscr{E}$ derived assuming a constant area for the upper part of the loop equal to 5×10^{18} cm^2. We can see that the transition from the very tenuous loops observed on January 24, 1992, to dense coronal loops corresponds to a change of the energy flux by a factor of 30 (second column of the table). However, in the third and fourth columns of the table, the corresponding difference decreases to approximately an order of magnitude, since the durations of the processes in denser coronal loops are, on average, shorter than in tenuous loops.

One important result is that the range of the total LDF energy proved to be rather small—much smaller than in impulsive events of various strengths. On the other hand, the total energies for LDFs are large, due to their large sizes and considerable durations.

4. CONCLUSIONS AND DISCUSSION

In [11] and the present paper, we selected flares in which the soft X-ray flux decayed slower than expected in a cloud isolated from the surrounding medium and heat sources. We were able to distinguish the active phase of the LDF, which lasts from 0.5 to 2–3 hours and is characterized by the formation of new loops and their compression. The primary energy release in the active phase does not take place continuously but occurs in separate processes that develop at increasing heights in the corona. At the end of the active phase, a system of giant loops (in an elementary LDF, a single arch) forms and exists from twelve hours to one day.

Our numerical simulations of the gas–dynamical processes in a giant loop formed during an LDF shows that, at the onset of the heating, intense motions develop and redistribute the material inside the loop. This dynamic regime is then replaced by a quasi-static one, with very slow changes of the physical conditions inside the loop. The separation into these two flow regimes is demonstrated most clearly in tenuous loops (elementary LDFs). In such loops, the soft X-rays decay on timescales t_{heat} = one hour; this is connected with the heat propagation rate in the case of negligible radiative losses. This timescale was distinguished in [19].

For more powerful LDFs, the dynamic and quasi-stationary parts of the process are not so clearly separated, and the soft X-ray light curve is determined by the ratio between the rates of heating and radiative cooling. In this case, the timescale for variations of the X-ray flux begins to exceed $t_{\rm rad}$ by a factor of 2 or 3 in modeled events of appreciable intensity. In the final stage in the existence of the giant loops, in both weak and strong LDFs, the downward heat flux near the loop feet is appreciably weakened due to weak rising motions that develop there. The result is that the X-ray emission continues for several hours due to radiative energy release in the loop, in which the plasma has become already dilute by the end of the LDF. The similar total durations of LDFs of various strengths are the result of this effect.

These considerations show that maintaining the X-ray flux for several hours is impossible without a prolonged flow of energy into the loop throughout the lifetime of the LDF. The total LDF energy is 2×10^{30}–3×10^{31} erg, which is comparable to the energy of powerful impulsive flares. Due to the long duration of these flares, the range of LDF energies from weakest to strongest is much smaller than in impulsive flares. The problem of the source of LDF heating after the active phase is key to understanding the physics of these phenomena.

Our solutions taking into account only gas–dynamical effects formally lead to the conclusion that a loop top rises to a height exceeding 100 000 km (in our model, this is connected with expansion of the loop). Strictly speaking, we can only say that there is a clear tendency for the loop to rise due to heating of plasma near the top. The conditions in the giant flare loops considered are such that the ratio of the plasma pressure to the magnetic pressure (the parameter β) in the lower parts of the loop is small and, as the process develops, begins to exceed unity near the top. At some stages of the ascent of giant loops, effects due to magnetic forces become significant. Therefore, though the temporal runs of the plasma temperature and density inside the loop have been determined with a reasonable degree of

certainty, our one-dimensional analysis is insufficient to describe observed changes of the ascent velocity of a giant loop.

Our results support the general picture of the physics of these phenomena developed as a result of *Yohkoh* observations [6, 8–12]. Let us consider a model active-region magnetic field in the form of a "horizontal dipole" [20]. A coronal mass ejection reveals individual internal force lines of this dipole-type field, and the subsequent return of the configuration to its initial state is accompanied by magnetic reconnection in a vertical current sheet. The actual existence of this source of LDF primary energy release has been confirmed by observations of flares with cusps. Gradual reconnection in increasingly higher regions (parts of the vertical current sheet) is each time accompanied by the formation of a new loop and its compression. Observations of the shrinkage effect and its interpretation [8] provide additional confirmation of this scenario. In addition to the downward motion of the perturbation from the reconnection point, which was accompanied by compression of the loop, the outward motion of a plasmoid into interplanetary space was recorded in X-ray observations.

In the active LDF phase (characterized by several reconnection acts, the formation of new loops, and their evolution), the heating of plasma in a forming giant loop seems natural. Our analysis requires that the corresponding process (some analog of the two shock waves of Petschek [21]) should exist in every LDF over a long time. We can formulate this conclusion in another way: Each reconnection process should reach an asymptotic mode corresponding to the solution of Petschek [21]. The small range of the LDF energies may be related to this. It is difficult to imagine how such slow shock waves can coexist with expanding giant loops. The problem of implementing Petschek's solution [21] in the final stages of flares deserves a serious theoretical analysis.

In powerful LDFs on the Sun, there is acceleration of particles, in particular protons, to energies of more than 1–10 GeV [22] (see also the review [23]). Similar prolonged flares on red dwarfs can be accompanied by the generation of gamma rays [9]. Active studies of these urgent questions in LDF physics are now beginning.

ACKNOWLEDGMENTS

This work was supported by the Russian Foundation for Basic Research (project code 99-02-16289) and the National Astronomy Program.

REFERENCES

1. R. Pallavicini, G. Tagliaferri, and L. Stella, Astron. Astrophys. **228**, 403 (1990).
2. S. Kahler, Astrophys. J. **214**, 891 (1977).
3. Z. Svestka, F. Farnik, H. S. Hudson, *et al.*, Solar Phys. **161**, 331 (1995).
4. F. Farnik, Z. Svestka, H. S. Hudson, *et al.*, Solar Phys. **168**, 331 (1996).
5. Z. Svestka, F. Farnik, P. Hick, *et al.*, Solar Phys. **176**, 355 (1997).
6. P. A. Sturrock, Nature **211**, 695 (1966).
7. R. A. Kopp and G. W. Pneuman, Solar Phys. **50**, 85 (1976).
8. T. G. Forbes and L. W. Acton, Astrophys. J. **459**, 330 (1996).
9. R. Pallavicini and G. Tagliaferri, Preprint No. 4, Palermo Astronomy (1998).
10. M. M. Katsova, J. Drake, and M. A. Livshits, Astrophys. J. **510**, 986 (1999).
11. K. V. Getman and M. A. Livshits, Astron. Zh. **76**, 704 (1999).
12. S. Tsuneta, Astrophys. J. **456**, 840 (1996).
13. *Solar-Geophysical Data* (Boulder, 1991–1993).
14. S. Masuda and J. Sato, *Workshop on Solar Flares and Related Disturbances* (Ibaraki, Hiroiso, 1996), p. 52.
15. Y. Hanaoka, *New Look at the Sun with Emphasis on Advanced Observations of Coronal Dynamics and Flares*, Ed. by S.Enome and T. Hirayama (Nobeyama Radio Observatory, Nagano, 1994), p.181.
16. Z. Svestka, Solar Phys. **108**, 411 (1987).
17. M. Varady and P. Heinzel, Harvard Obs. Bull. **21**, 33 (1997).
18. K. Smith, Z. Svestka, K. T. Strong, *et al.*, Solar Phys. **149**, 363 (1994).
19. E. Hiei, *Solar Coronal Structures*, Ed. by V. Rusin, P. Heintzel, and J.-C. Vial (VEDA, Bratislava, 1994), p. 163.
20. J. Lin, T. J. Forbes, E. Priest, *et al.*, Solar Phys. **159**, 275 (1995).
21. H. E. Petschek, *The Physics of Solar Flares*, Ed. by W. N. Hess (NASA, Washington, 1964), p. 453.
22. I. Chertok, J. Moscow Phys. Soc. **7**, 31 (1997).
23. M. M. Katsova and M. A. Livshits, *Flares and Flashes*, Ed. by J. Greiner, H. W. Duerbeck, and R. E. Gershberg (Lecture Notes in Physics, vol. 454) (Springer, Berlin), p. 177.

Translated by G. Rudnitskiĭ

Astronomy Reports, Vol. 44, No. 4, 2000, pp. 262–270. Translated from Astronomicheskiĭ Zhurnal, Vol. 77, No. 4, 2000, pp. 303–312.

Large-Scale Solar Magnetic Field: Latitudinal Dependence

V. N. Obridko and B. D. Shelting

Institute of Terrestrial Magnetism, Ionosphere, and Radiowave Propagation, Russian Academy of Sciences, Troitsk, Moscow oblast, 142092 Russia

Received February 25, 1999

Abstract—Large-scale solar magnetic fields in the latitude range 50° S–50° N are analyzed in detail for a long time interval (1915–1990). We are primarily concerned with the two types of large-scale fields forming the two- and four-sector patterns on the Sun. The rotation parameters of these structures are obtained for all latitudes considered. The contribution of the two-sector structure grows and that of the four-sector structure decreases toward high latitudes. The magnetic field is activated simultaneously over a wide latitude range. Since both magnetic-field systems exhibit quasi-rigid rotation, their current systems must either be concentrated in a narrow latitude range or be situated beneath the convection zone, where rotation is only weakly differential. A period of about three years is manifest in the difference between the rotation periods for the two types of magnetic field. Physically, this may imply that these oscillations are external with respect to any level, and there is some phase delay due to their propagation from one level to another. We can conclude with a fair degree of certainty that as the activity level rises, the rotation speed decreases, and vice versa. *© 2000 MAIK "Nauka/Interperiodica".*

1. INTRODUCTION

We have already described [1–4] our techniques for reconstruction of the large-scale magnetic field over a long time interval (1915–1996). When reconstructing the field from H_α spectroheliograms, we used direct magnetic field measurements [5–8] for the calibration. The resulting data were used to study the cyclic variation and rotation of the two-sector and the four-sector structures of the large-scale solar magnetic field. Throughout this paper, unless otherwise specified, we will deal with synodic rotation periods and sidereal angular speeds.

It is important to note that our calculations of the magnetic field at the source surface essentially correspond to spatial filtering and automatically select the field harmonics that vary most slowly with height. This implies that all subsequent conclusions concerning the characteristics of the structures refer to some depth below the photosphere, which is not known and will be called the generation region for the corresponding structure of the global magnetic field.

2. PROBLEM STATEMENT AND MATHEMATICAL TECHNIQUES

A detailed formulation of the problem and the mathematical techniques applied were presented in our earlier paper [4]. We repeat here only information needed to describe the results of this study.

We broke down the time sequence of daily values of the magnetic field at the source surface for latitudes from 50° S to 50° N and the period from January 1, 1916, to December 16, 1988, into 54-day sliding intervals shifted with respect to one another by 27 days. The following least-squares approximation was used for each of these intervals:

$$\begin{aligned} y_i &= A_1\cos(2\pi i/T) + A_2\sin(2\pi i/T) \\ &+ A_3\cos(4\pi i/T) + A_4\sin(4\pi i/T) + A_5, \\ A_{12} &= \sqrt{(A_1^2 + A_2^2)}, \quad A_{34} = \sqrt{(A_3^2 + A_4^2)}, \\ \tan\varphi_1 &= A_1/A_2,\ \tan\varphi_2 = A_3/A_4,\ T = 27.275 \text{ days}. \end{aligned} \tag{1}$$

We showed in [4] that the resulting phases φ_1 and φ_2 can easily be recalculated to give the true rotation periods T_2 and T_4 for the two-sector and four-sector structures. We represent all amplitudes A_{12} and A_{34} in units of the rms error. All values found using formula (1) were then smoothed using 13 points.

In [4], we studied regularities in the variation of the large-scale field of the equatorial zone. Here, we consider such regularities for all latitudes. We will refer to 30°–50° as middle latitudes. For the sake of brevity, we will use the notation A_2 and A_4 to refer to A_{12} and A_{34}, respectively.

3. CHARACTERISTICS OF THE SECTOR STRUCTURES

3.1. Relative Importance of the Two-Sector and Four-Sector Structures

Figure 1 shows the time dependences of $A_2(t)$, $A_4(t)$, and A_4/A_2 for all latitudes. Although the pattern is rather complex, a cyclic variation in intensity can be distinguished with a fair degree of certainty. Note that the two modes have sharply different behavior. The cyclic

1063-7729/00/4404-0262$20.00 © 2000 MAIK "Nauka/Interperiodica"

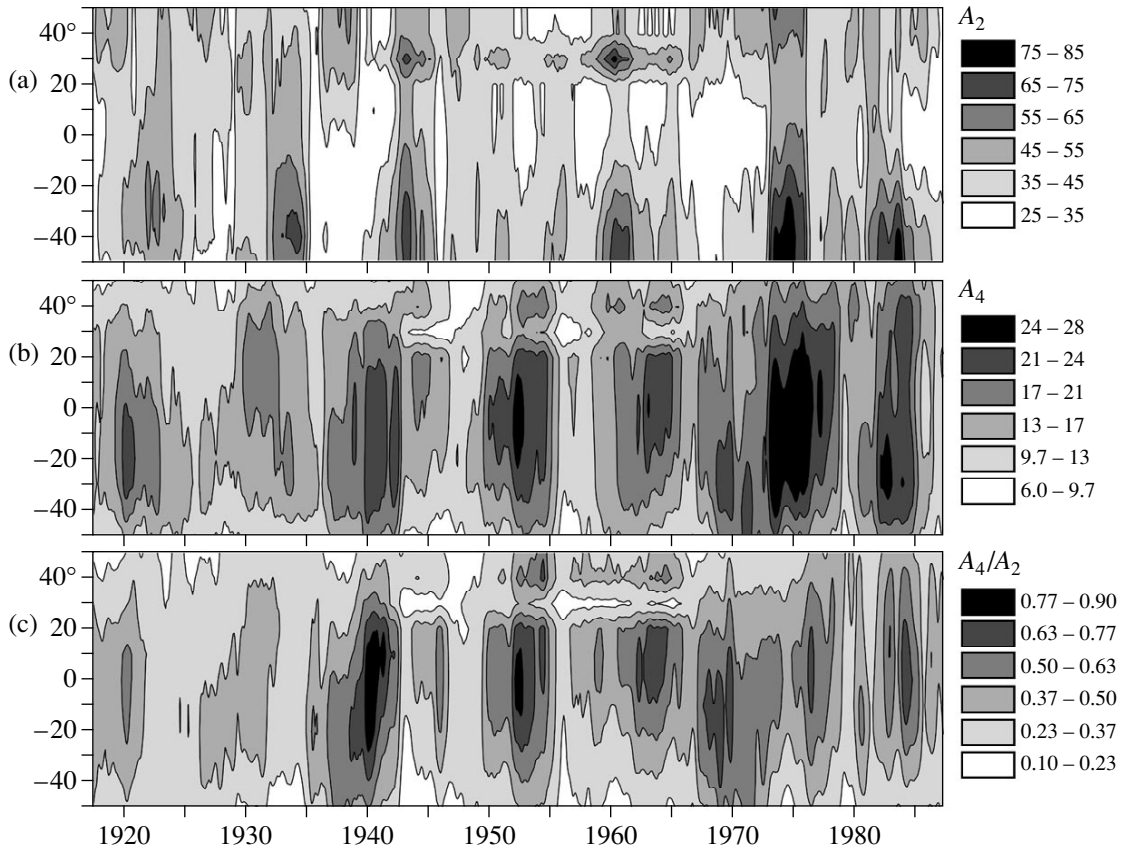

Fig. 1. Time dependences of $A_2(t)$, $A_4(t)$, and A_4/A_2 for the latitude range from 50° S to 50° N.

variations of A_2 and A_4 are more clearly expressed at middle latitudes and equatorial zones, respectively. Almost without exception, A_2 is larger than A_4; the four-sector structure becomes comparable to (or even more significant than) the two-sector structure only in individual, short time intervals. We are, thus, again assured that the four-sector structure is not a merely harmonic of the two-sector structure.

There is a remarkable feature in the behavior of all quantities at a latitude of 30° N during 1940–1965. Throughout this 25-year period, a narrow zone of enhanced two-sector and weakened four-sector structure was present against a background of quasi-periodic patterns elongated in latitude. The nature of this phenomenon remains unclear, although this time interval is unusual in many respects. We have already discussed the peculiarities associated with this interval [1–4] and will revisit this point below.

A gradual increase in A_2 and A_4 is seen from the beginning to the end of the observation period. This is especially apparent for A_2 at southern middle latitudes and for A_4 in the equatorial zone. By and large, the variations in these amplitudes are similar to the secular variations in the Wolf number.

Figure 2 presents the values of A_2, A_4, and A_4/A_2 averaged over the entire observation period as functions of latitude. The difference between the latitudinal variations of A_2 and A_4 is especially clearly visible in the averaged values. The anomaly at latitude 30° N can again be seen in Fig. 2; it obviously stems from the anomaly that was observed in cycles 18 and 19 (Fig. 1).

The cross-correlation coefficients for $A_2(t)$ and $A_4(t)$ (solid line) and $T_2(t)$ and $T_4(t)$ (dashed line) are shown in Fig. 3. These do not exceed 0.4 for the intensities and 0.2 for the periods of the large-scale patterns. An asymmetry between the hemispheres is also apparent: The cross-correlation coefficients are greater in the southern than in the northern hemisphere. All these features provide evidence for the independence (or only very weak dependence) of the two-sector and four-sector structures in the global magnetic fields, both at the source surface and where these structures are generated.

Figure 4 depicts the dependence of the measured values for A_2, A_4, and A_4/A_2 on the phase of the 11-year cycle for all latitudes. Phases 0.0 and 1.0 correspond to Wolf-number minimum and phases 0.35–0.4 to Wolf-number maximum. A pronounced phase dependence is seen in the oscillation intensity of the two-sector and four-sector structures: the A_2 values (Fig. 4a) reach their maximum at the decline phase and near the cycle minimum; the A_4 values (Fig. 4b) are maximum near virtually all reference points (the points t_{MAX}, t_{Dm}, t_{min},

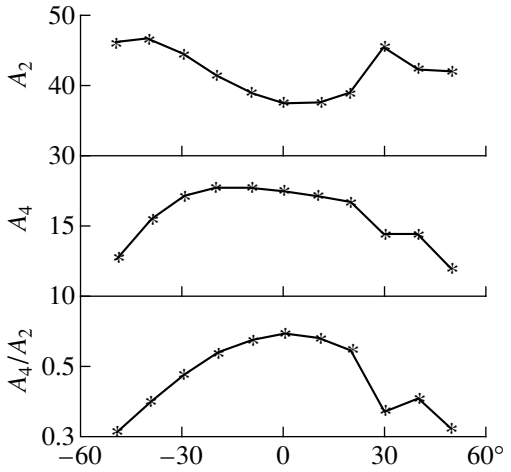

Fig. 2. Latitude dependences of A_2, A_4, and A_4/A_2 averaged over the entire observation period.

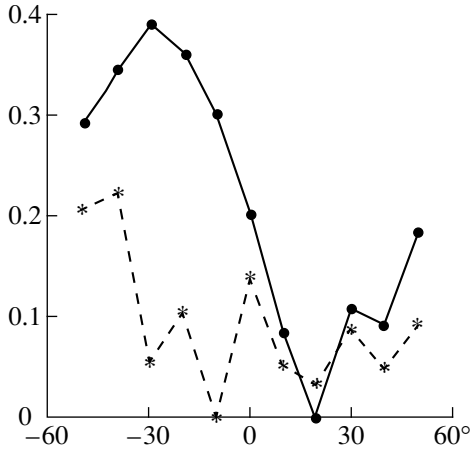

Fig. 3. Cross-correlation coefficients for $A_2(t)$ and $A_4(t)$ (solid line) and for $T_2(t)$ and $T_4(t)$ (dashed line) as functions of latitude.

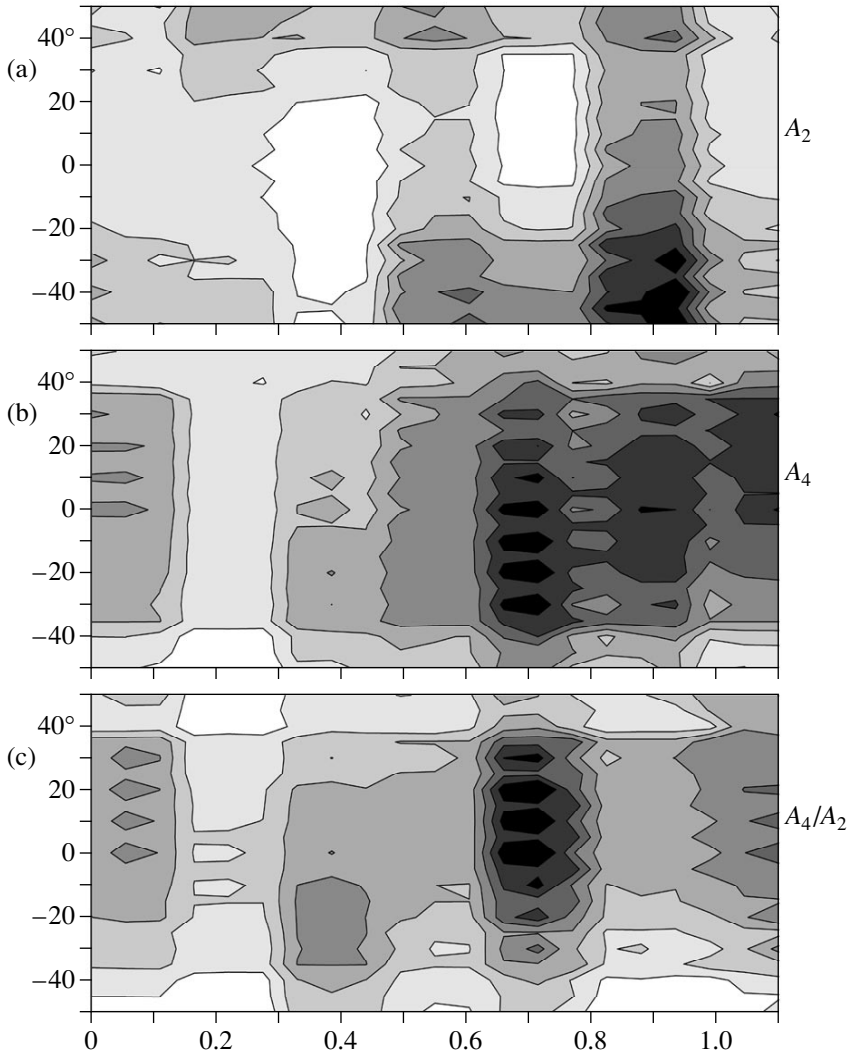

Fig. 4. Dependence of (a) the two-sector structure, (b) the four-sector structure, and (c) their amplitude ratio on the phase of the 11-year cycle.

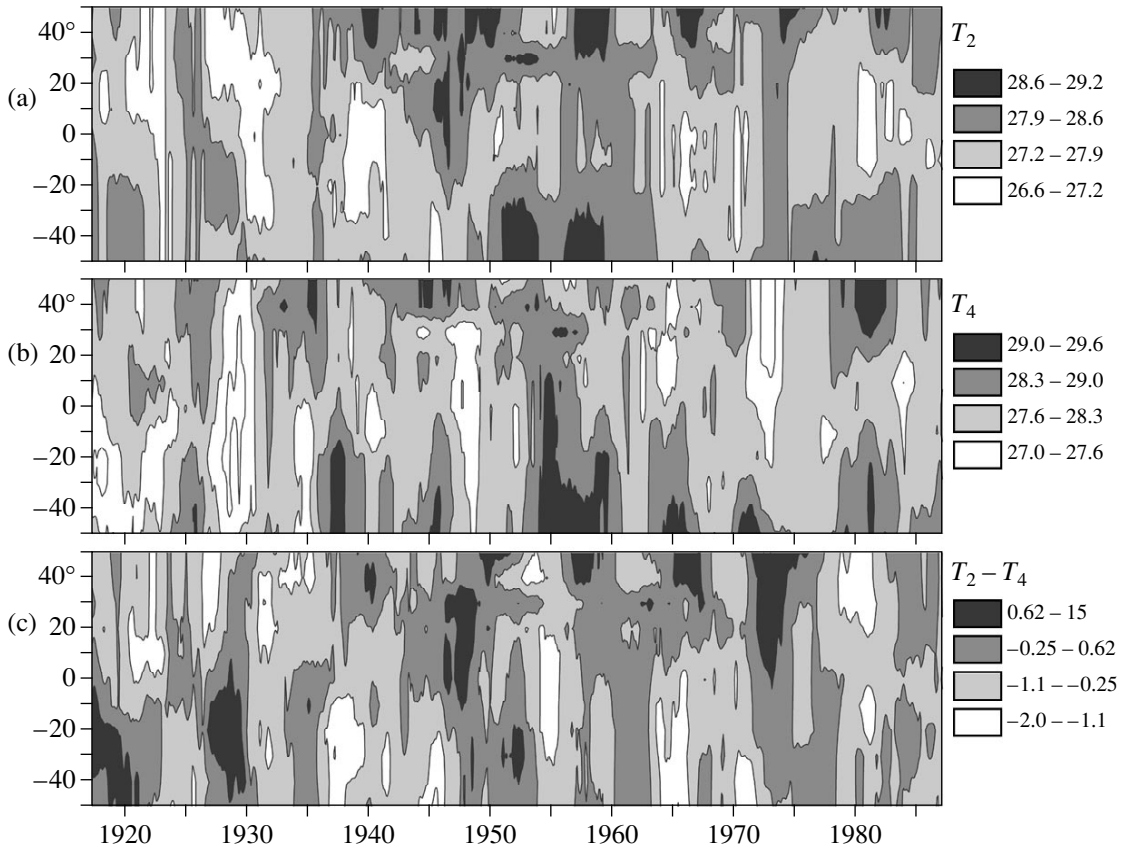

Fig. 5. Latitude dependences for the sidereal rotation periods (a) $T_2(t)$ of the two-sector structure and (b) $T_4(t)$ of the four-sector structure, as well as (c) their difference T_2–T_4.

and t_{mA} introduced by Kuklin *et al.* [9–11]). This draws a sharp distinction between the cyclic dependences for A_4 and A_2.

Figure 4c illustrates the phase variation of the ratio A_4/A_2. This ratio is usually below 0.5 but exceeds 0.7 A_4 near phases 0.1, 0.35, and 0.7; this implies that the four-sector structure becomes very significant. These phases correspond to the basic reference points of the cycle.

3.2. Rotation of the Two- and Four-Sector Structure

We show the latitude dependences of the synodic rotation periods $T_2(t)$ and $T_4(t)$ for the two-sector and the four-sector structure in Fig. 5, together with the latitude dependence of their difference T_2–T_4. A comparison of this figure with Fig. 1 reveals the existence of substantially finer structure in the magnetic-field rotation periods compared to the amplitudes.

During the first half of the interval under study, the cyclic variation $T_2(t)$ of the rotation periods (Fig. 5a) follows a fairly simple pattern. The period gradually increases at the beginning of each cycle and reaches a maximum by the end of the growth phase, or even at the maximum of the cycle, almost simultaneously at all latitudes. Further, disturbances in this pattern arise. In cycle 19, the range of maximum values of the period T_2 becomes very wide (15 years or so); the next maximum-period interval is delayed until the decline phase of cycle 20 and the early stage of cycle 21 (1973–1975). This may be related to the secondary activity maxima that were observed in these cycles two years after the main, tabulated maxima of the cycles. Finally, during cycle 22, there are signs of the emergence of a region of long rotation period at the beginning of the cycle maximum, in 1986.

The regions of long and short rotation periods T_4 (Fig. 5b) are less extended in latitude than the corresponding regions for T_2 and are discontinuous in the equatorial zone. For this reason, we did not see them in [4]. In cycle 19, a disturbance in the time evolution also takes place, after which the regularity referred to above breaks down.

In [4], we considered observations of the sector structures by various authors [12–15]. These results are contradictory, possibly due to instabilities of the rotation pattern during recent cycles.

Figure 5 suggests that the period difference T_2–T_4 exhibits the most regular distribution (Fig. 5c). Our analysis supports this impression and reveals a quasi-period of 2–3 years with a constant amplitude (see Fig. 7

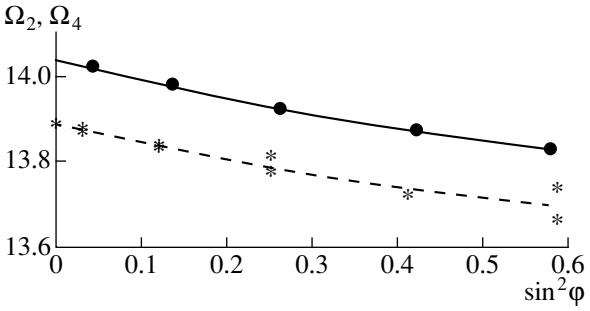

Fig. 6. Mean sidereal angular rotation speeds Ω_2 (solid circles) and Ω_4 (asterisks) as functions of $\sin^2\varphi$.

below). The character of these oscillations does not change with time (as was already found for the equatorial zone in [4]), and they do not exhibit any dependence on the phase of the 11-year cycle.

Figure 6 presents the mean sidereal angular rotation speeds Ω_2 and Ω_4 (in deg/day) as functions of $\sin^2\varphi$. The four-sector structure rotates slower than the two-sector structure at all latitudes. This figure also shows the following third-order polynomial approximations:

$$\Omega_2 = 14.033 - 0.474\sin^2\varphi + 0.299\sin^4\varphi, \quad (2a)$$

$$\Omega_4 = 13.883 - 0.444\sin^2\varphi + 0.230\sin^4\varphi. \quad (2b)$$

Apparently, the rotation of the four-sector structure is, on average, somewhat closer to rigid rotation, although the parameters of (2a) and (2b) differ little.

3.3. Quasi-Periodic Variations in the Sector Structures

To continue our analysis of time variations in the parameters of the sector structures, let us find out whether or not these variations contain any stable quasi-periods. Such quasi-periodic variations can be sought using various techniques. We applied a double-precision Fourier decomposition. Time was measured in units of 27 days, and each sample contained 972 points. The time resolution near a period of two years was 0.02 years.

Figure 7 shows the Fourier spectra for A_2, A_4, and T_2–T_4. The horizontal axes show the frequencies obtained from the quasi-periods in the adopted time units. In addition to the period of about 10 years, we

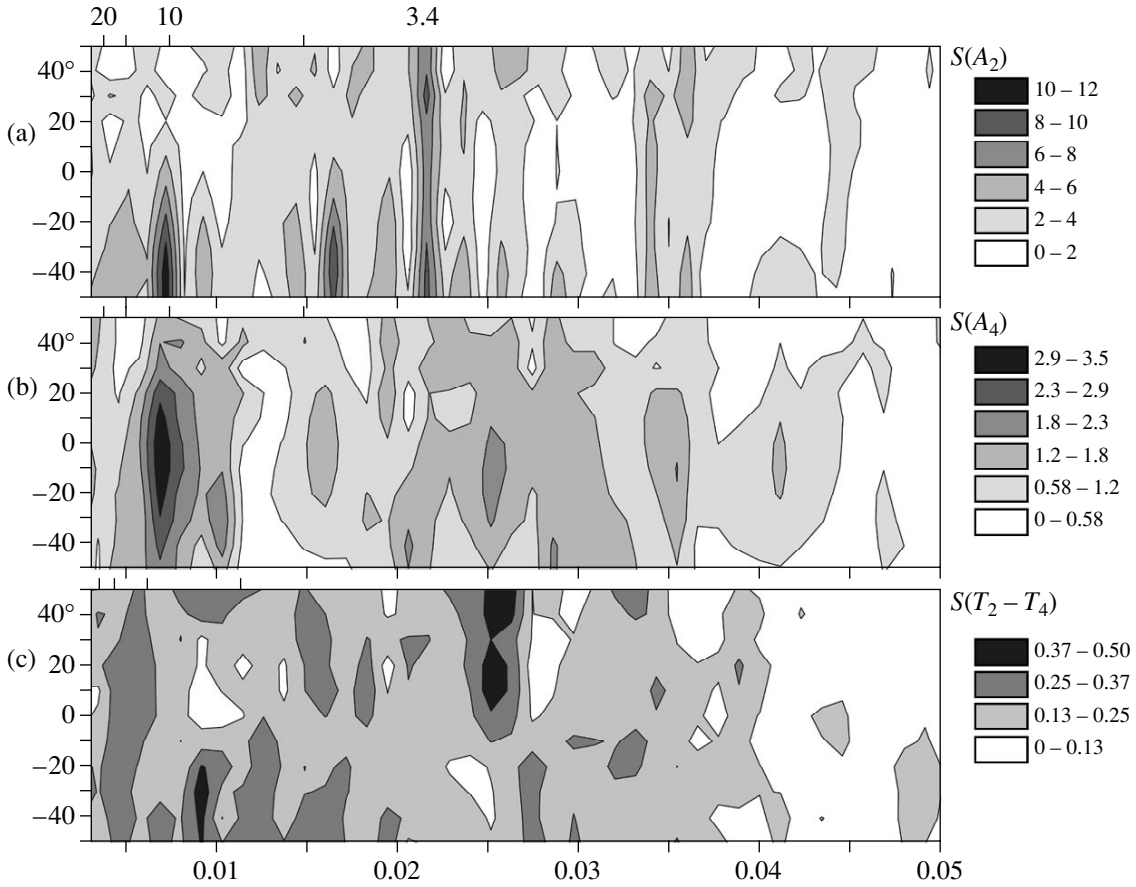

Fig. 7. Amplitude spectra for (a) the two-sector structure, (b) the four-sector structure, and (c) their period difference. The lower horizontal axis plots frequency, the upper horizontal axis plots the corresponding periods for some of the most significant spectral maxima, and the vertical axis plots latitude. Time is measured in units of 27 days.

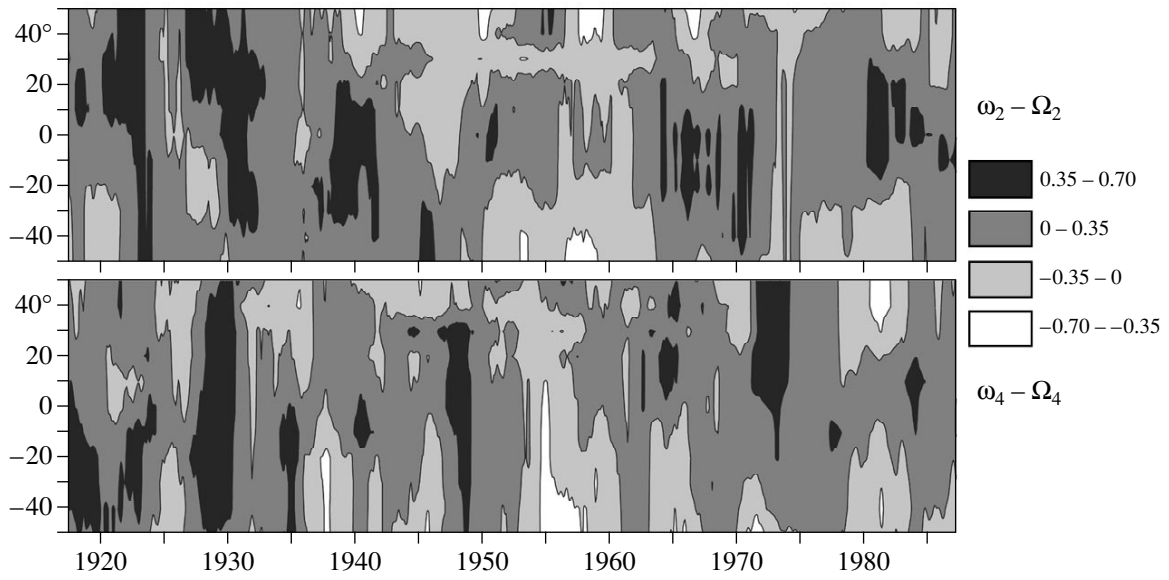

Fig. 8. Spatial–temporal distribution of increased and decreased solar rotation speeds.

can clearly see quasi-periods of several years in the spectra in Fig. 7. The frequency 0.022, which corresponds to a quasi-period of 3.36 years, is most pronounced in the A_2 spectrum. It appears as a very narrow strip covering all latitudes (a frequency range from 0.034–0.036 to 0.042). We will refer to the periods corresponding to this range to as the 2- to 3-year quasi-periodic oscillation (2- to 3-yr QPO). Separate quasi-two-year periods can be observed in the spectrum. In the A_4 spectrum, the 2- to 3-yr QPO is less distinct, while the 11-year period is more pronounced.

Neither the 11-year cycle nor the 2- to 3-yr QPO are clearly visible in the spectrum of the rotation-period variations; on the whole, this spectrum (not presented here) has a noiselike character. This could be expected based on our analysis of Fig. 5. At the same time, as noted above, the frequency 0.026 (a quasi-period of about three years) is clearly expressed in the spectrum of T_2–T_4 (Fig. 7c), and its intensity far exceeds that of the 11-year cycle. Moreover, the 11-year period is virtually absent, but there is a relatively weak 15- to 17-year period.

The sidereal angular speeds minus the mean angular speed obtained according to (2a) and (2b) are shown in Fig. 8. We can see intervals when the solar rotation speed was elevated or reduced compared to the differential-rotation law averaged over the entire observation period. Note that, although the speed differences are small, these results are undoubtedly trustworthy, since regions of a given sign are spatially and temporally extended. This should be kept in mind when considering Fig. 9 below.

Let us discuss in greater detail the spatial–temporal location of the fastest rotation periods. We begin by analyzing the rotation of the two-sector structure (Fig. 8a).

(1) In 1918, a narrow maximum was observed near latitude 20° N during the decline phase of cycle 15. Then, in 1920, a new maximum appeared near 20° N. A year later, this maximum reached middle latitudes in the northern hemisphere and, another year later, it stretched from the northern to the southern hemisphere (still in the decline phase of cycle 15).

(2) At the beginning of the decline phase of cycle 16, in 1926, a maximum appeared at latitudes 10–50° N, where it remained until 1930. Then, the northern boundary of the fast-rotation zone lowered its latitude to 30° N; simultaneously, the southern boundary abruptly migrated to the southern hemisphere and reached 40° S, where it resided until the end of 1932. In the equatorial zone, however, this maximum disappeared somewhat earlier.

(3) In 1937–1942, the fast-rotation zone was in the central region, between 30° N and 30° S, also in the decline phase of cycle 17.

(4) Next is a nearly 20-year-long (1942–1964) wide zone of reduced speed, which exceeded the mean value only slightly and for short times in the equatorial region.

(5) During 1964–1971, isolated bursts of fast rotation were observed in the central zone of the Sun; they gradually drifted southward. Thus, there was some phase discontinuity in the middle of the 20th century, in cycle 19. In contrast to what was observed previously, these narrow maxima occurred in the growth phase of cycle 20.

(6) However, in cycle 21, this regularity recovered, and several maxima in the central region in succession again occurred in the decline phase.

By and large, this regularity also holds for the four-sector structure (Fig. 8b). The first three maxima coin-

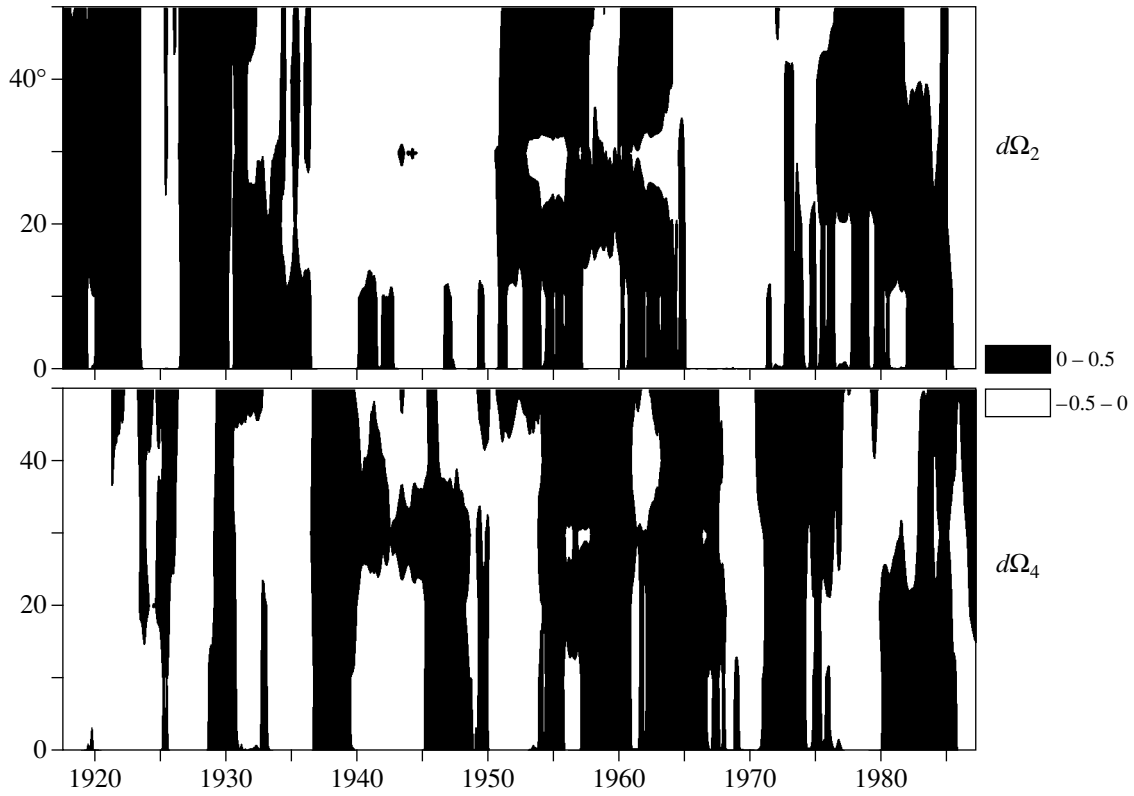

Fig. 9. Asymmetry of sidereal angular rotation speeds.

cide in time with the rotation-speed maxima for the two-sector structure, although they have a different latitude distribution. During the period 1947.5–1949.2, a narrow but very extended maximum was observed between 50° S and 35° N in the decline phase of cycle 18. Then, a peculiar period of strongly reduced speeds occurred during the maximum of cycle 19 and the beginning of its decline phase. Further, there were brief but pronounced periods of increased rotation speed at the minimum following cycle 19 (1964–1965) and during the decline phases of cycles 20 (1971–1974) and 21 (1984).

Thus, periods of accelerated rotation are typical of the decline phases and minima of activity cycles; i.e., they exhibit a cyclic recurrence. This agrees with our conclusion that the magnetic-field configurations are open [16]. Moreover, we again find, as in [4], that the interval between cycles 18 and 19 was peculiar in terms of solar activity.

To check our results, we varied the technique used to analyze the observed rotation speeds, subtracting from them the differential-rotation law smoothed over a three-year interval rather than averaged over the entire observation period. Although the new latitude–time distribution of the rotation-speed differences (not presented here) is somewhat different from that in Fig. 8, it confirms all the basic regularities indicated in our analysis (increases in rotation speed during the decline phases and minima of cycles and an anomalous period in the middle of the 20th century).

Figure 9 illustrates the asymmetry of the sidereal angular rotation speeds between the northern and southern hemispheres separately for the two-sector and four-sector magnetic-field structures. Positive values correspond to accelerated rotation of the northern hemisphere. In the case of the two-sector structures, alternating regions in which the northern hemisphere rotates faster and slower than the southern hemisphere stand out; they are extended in both time (4 to 14 years) and latitude (as a rule, extending from the equator to the pole). Their distribution is not strictly regular; nevertheless, intervals of faster rotation of the northern hemisphere (1917–1923, 1927–1937, 1951–1965, 1975–1986) are normally associated with odd cycles, and intervals of slower rotation (1923–1927, 1937–1951, 1965–1975) with even cycles. As could be expected, the four-sector pattern is somewhat more complex and has a fine structure; the maximum time interval covered by bands of a given sense of rotation does not exceed 6–7 years. Thus, Fig. 9 reveals torsional oscillations in the rotation of the solar sector structures.

3.4. Variations in the Parameters of the Sector Structures over a Long Time Interval

We showed in [4] that the transition from cycle 18 to cycle 19 was accompanied by a substantial change in the character of global solar activity. At that time, the rotation period of the two-sector structure reached a

maximum for both maximum and minimum cycle phases. The rotation-period difference T_2–T_4 also sharply increased. Furthermore, the relative amplitudes of the two-sector and four-sector structures changed in cycles 18–19.

Inspection of Fig. 8 indicates that the peculiarity of the transition from cycle 18 to cycle 19 is also manifest in the character of the solar rotation at all latitudes. This can also be seen in an analysis of the rate of differential rotation of the structures.

Figure 10 illustrates the variation of the differential-rotation rate t (the second coefficient in (2a), (2b), and similar formulas) averaged over 10 years. The solid line corresponds to the two-sector structure and the dashed line to the four-sector structure. Mostly, t is small, no larger than 0.3–0.4. It is interesting that, at some times, t even exceeds zero slightly. For the four-sector structure, this quantity remained relatively small during the entire observation period. For the two-sector structure, the differential-rotation rate increased sharply in 1952. Another substantial enhancement in differential rotation was observed for both structures at the end of the period under study.

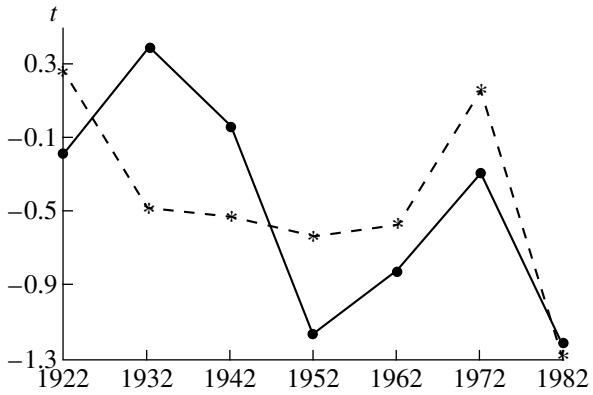

Fig. 10. Variation of the differential-rotation rate averaged over 10 years for the two-sector (solid line) and four-sector structure (dashed line).

4. DISCUSSION OF THE RESULTS

Let us summarize the basic results of our study. We have confirmed the earlier finding [17–21] that the two-sector structure is predominant in the large-scale magnetic fields. The contribution of the two-sector structure increases and that of the four-sector structure decreases toward middle latitudes. The widely accepted view that the four-sector structure is merely a harmonic of the two-sector structure is not correct.

The times of enhancement and weakening of the sector structures form vertical strips in latitude–time diagrams (Fig. 1). This contrasts with the pattern of the often recorded meridional drift of structures. In our case, the time shift is normally smaller than the extent of the corresponding strip in time. This is probably due to the fact that the drift is usually determined from the pattern of the photospheric or chromospheric magnetic fields. In fact, the data were filtered three times in our study. First, H_α observations were converted into measurements of the large-scale field. Second, the resulting data were reduced to the source surface, corresponding to a spatial filtering that retains only two harmonics of the expansion. Finally, we separated the two-sector and four-sector structures.

Thus, the strips in the latitude–time diagram indicate that the magnetic field is simultaneously activated over a wide frequency range and is associated with the same current system within each magnetic-field structure. Since both systems rotate quasi-rigidly, the current system must either be localized in a narrow latitude range or be situated beneath the convection zone, where rotation is only weakly differential.

At the same time, the current systems are not identical. The spatial–temporal distributions for the two-sector and four-sector structures (Figs. 1, 4) are very different, and the cross correlation of their amplitudes and rotation periods is very weak (Fig. 3).

We have already shown in our analysis of the equatorial magnetic field [4] that the 2- to 3-year oscillation (2- to 3-yr QPO) is quite pronounced in the variation spectrum of the contributions of the structures A_2 and A_4. This oscillation is more clearly expressed in the A_4 spectrum than in the A_2 spectrum. The main features described in [4] are also evident in our analysis for all latitudes. However, the three-year oscillation is more pronounced in A_2 (Fig. 7).

Surprising features appeared during our analysis of the spectrum of the period difference T_2–T_4. In the spectra of T_2 and T_4, as in the spectra of A_2 and A_4, the 11-year period is obviously predominant. However, a period of about three years dominates in the spectrum of T_2–T_4, especially in the northern hemisphere. At the same time, the spectrum intensity is much lower near the frequency 0.007 (which corresponds to the 11-year period), where it forms a blurred band between 10 and 15 years (Fig. 7). This seems to be related to the fact that the 11-year cycle reflects the natural frequency of the generation regions for the global magnetic field; they are phased at both the levels where the two-sector and four-sector structures arise. Therefore, the subtraction procedure appreciably weakens both modes at this frequency. In contrast, the 2- to 3-yr QPOs are much less phased. This may be a direct consequence of the shorter period, but may have a less simple physical nature: These oscillations may be external with respect to any level, so that there exists a phase delay due to their propagation. Obviously, the subtraction procedure weakens unphased oscillations much less.

In their studies, Javaraiah *et al.* [22–24] analyzed the solar differential rotation and its asymmetry using Greenwich data for sunspot groups. A number of rotation periods were derived, ranging from 42 to 3 years;

the three-year oscillations were manifest as very high peaks in the power spectra of the equatorial-zone asymmetry (the asymmetry in the parameter *A* of the differential-rotation equation, which was determined independently for the northern and southern hemispheres). Javaraiah *et al.* [22–24] do not regard the large number of peaks in the spectrum as a mathematical artifact, and instead associate it with the behavior of the Sun as a nonlinear force oscillator.

The pattern of the period variations over the long time interval considered is much more definite. One general property of the sector-structure rotation is detected with a fair degree of certainty: Rises of the activity level are accompanied by decreases in the rotation speed; conversely, the rotation speed is higher when the activity is lower. This is the case for both the 11-year cycle and for longer time intervals. During high-activity cycles (18, 19), the rotation speed was minimum. Moreover, within a cycle, a higher rotation speed near the minimum was accompanied by a higher differential-rotation rate. In their study of the relationship between the differential rotation of sunspots and solar activity, Hathaway and Wilson [25] arrived at very similar conclusions: The Sun rotates faster when there are fewer sunspots on its surface; therefore, the fastest rotation occurs at the minima of solar-activity cycles, and rotation is faster during low cycles with lower sunspot numbers and areas. Makarov *et al.* [26] and Makarov and Tlatov [27] also showed that the equatorial rotation speed and differential-rotation rate are higher during cycle minima.

We have also confirmed the presence of a 55- to 60-year cycle, displaying a peculiar period in 1952–1960. This cycle has been described in [4] and also by some other investigators [26–29].

ACKNOWLEDGMENTS

We are grateful to V. I. Makarov for providing us with source material in the form of H_α maps and to G. Gaziev for carrying out the primary digital processing. This work was supported by the Russian Foundation for Basic Research (project code 99-02-18346).

REFERENCES

1. V. N. Obridko and B. D. Shelting, in *Modern Problems of the Solar Cycles*, Ed. by V. I. Makarov and V. N. Obridko (GAO, St. Petersburg, 1997), p. 193.
2. V. N. Obridko and B. D. Shelting, Solar Phys. **184**, 187 (1999).
3. V. N. Obridko and B. D. Shelting, in *New Solar Activity Cycle: Observational and Theoretical Aspects*, Ed. by V. I. Makarov and V. N. Obridko (GAO, St. Petersburg, 1998), p. 137.
4. V. N. Obridko and B. D. Shelting, Astron. Zh. **77**, 124 (2000).
5. J. T. Hoeksama, J. M. Wilcox, and P. H. Sherrer, J. Geophys. Res. **87**, 10331 (1982).
6. J. T. Hoeksama, J. M. Wilcox, and P. H. Sherrer, J. Geophys. Res. **88**, 9910 (1983).
7. J. T. Hoeksama and P. H. Sherrer, *Solar Magnetic Field: 1976 through 1985* (WDCA, Boulder, 1986).
8. J. T. Hoeksama, *Solar Magnetic Field: 1985 through 1990* (WDCA, Boulder, 1991).
9. G. V. Kuklin, V. N. Obridko, and Yu. I. Vitinskiĭ, Soln. Dannye **3**, 56 (1986).
10. G. V. Kuklin, V. N. Obridko, and Yu. I. Vitinskiĭ, in *Solar–Terrestrial Predictions: Proceedings of a Workshop at Leura, Australia, October 1989* (1990), **1**, 474.
11. G. V. Kuklin, V. N. Obridko, and Yu. I. Vitinskiĭ, in *XIII Consultative Meeting on Solar Physics*, Ed. by V. N. Obridko (Nauka, Novosibirsk, 1989), Vol. 1, p. 321.
12. L. Svalgaard, in *Geophys. Papers* (Danish Meteorol. Inst., 1972), R-29.
13. J. M. Wilcox and D. S. Colburn, J. Geophys. Res. **74**, 2388 (1969).
14. J. M. Wilcox and D. S. Colburn, J. Geophys. Res. **75**, 6366 (1970).
15. L. Svalgaard, J. M. Wilcox, and Th. L. Duvall, Solar Phys. **37**, 157 (1974).
16. V. N. Obridko and B. D. Shelting, Solar Phys. **187**, 185 (1999).
17. V. N. Obridko, in *Problems of Cosmic Electrodynamics*, Ed. by É. I. Mogilevskiĭ (Nauka, Moscow, 1981), p. 21.
18. V. N. Obridko and L. I. Starkova, in *Problems of Cosmic Electrodynamics*, Ed. by É. I. Mogilevskiĭ (Nauka, Moscow, 1981), p. 29.
19. G. V. Kuklin and V. N. Obridko, Preprint No. 10, SibIZMIR (Siberian Institute of Terrestrial Magnetism, Ionosphere, and Radiowave Propagation, Irkutsk, Russia) (1982).
20. V. N. Obridko, Soln. Dannye **11**, 54 (1984).
21. G. V. Kuklin and V. N. Obridko, in *Physics of Solar Activity*, Ed. by É. I. Mogilevskiĭ (Nauka, Moscow, 1988), p. 146.
22. J. Javaraiah and M. H. Gokhale, Solar Phys. **158**, 173 (1995).
23. J. Javaraiah and M. H. Gokhale, Solar Phys. **170**, 389 (1997).
24. J. Javaraiah and R. W. Komm, Solar Phys. **184**, 41 (1999).
25. D. H. Hathaway and R. M. Wilson, Astrophys. J. **357**, 271 (1990).
26. V. I. Makarov, A. G. Tlatov, and D. K. Callebaut, Solar Phys. **170**, 373 (1997).
27. V. I. Makarov and A. G. Tlatov, Astron. Zh. **74**, 474 (1997).
28. H. Yoshimura and M. A. Kambry, Solar Phys. **148**, 11 (1993).
29. H. Yoshimura and M. A. Kambry, Astron. Nachr. **314**, 9 (1993).

Translated by A. Getling

Astronomy Reports, Vol. 44, No. 4, 2000, pp. 271–277. Translated from Astronomicheskiĭ Zhurnal, Vol. 77, No. 4, 2000, pp. 313–320.

Detection of a Cyclotron Line in the Radio Spectrum of a Solar Active Region and Its Interpretation

V. M. Bogod[1], V. I. Garaimov[1], V. V. Zheleznyakov[2], and E. Ya. Zlotnik[2]

[1]*Special Astrophysical Observatory, St. Petersburg Branch, St. Petersburg, Russia*

[2]*Institute of Applied Physics, Nizhniĭ Novgorod, Russia*

Received March 15, 1999

Abstract—Observations of the active region AR 7962 obtained at 2–32 cm on the RATAN-600 radio telescope on May 10–12, 1996, are presented. The high-resolution measurements detected a narrow feature near 8.5 cm against the background of the smooth spectrum of the local source associated with sunspots. This narrow-band emission is identified with a bright, pointlike, high-frequency source at 1.7 cm recorded on maps made using the Nobeyama radio telescope. The characteristics of the observed line (lifetime 3 days, brightness temperature of the order of several million Kelvin, relative width of about 10%) suggest that it can be explained as thermal cyclotron radiation at the third harmonic of the electron gyrofrequency from a compact source containing a dense, hot plasma; the corresponding higher frequency emission could be due to thermal Bremsstrahlung. Analysis of the RATAN-600 and Nobeyama data can be used to probe the magnetic field, kinetic temperature, and electron density in the radiation source in the corona. *© 2000 MAIK "Nauka/Interperiodica".*

1. INTRODUCTION

The existence of narrow-band cyclotron features in the radio spectra of solar active regions was predicted in [1, 2], and has been expected for a rather long time. Theoretical analyses indicated the possibility of detecting individual cyclotron lines at harmonics of the electron gyrofrequency. Cyclotron features can form in sources with various types of coronal kinetic-temperature and magnetic-field distributions: in neutral current sheets, in regions where the magnetic field along the line of sight reaches a maximum at some point, in magnetic flux tubes filled with "hot" electrons, and in the hot X-ray cores responsible for so-called elementary flare outbursts [3]. The frequency spectrum and polarization of the radiation for each type of distribution are characteristic; this makes it possible to probe the activity center using the fine structure of the spectra.

However, observations of cyclotron lines encounter substantial difficulties: detection of cyclotron features and investigation of the regions of line formation require antennas with high directivity and spectrographic apparatus with high frequency resolution. The first report of a possible detection of a cyclotron line using the VLA was made by Wilson [4]. Some indirect evidence for the present of cyclotron lines in active-region spectra was obtained by Schmahl *et al.* [5]. The detection of a cyclotron line at 18 cm using a ten-channel radio spectrograph mounted at the VLA was reported by Wilson [6] and then Lang *et al.* [7]. Zheleznyakov and Zlotnik [8, 9] interpreted this line as cyclotron radiation from a hot coronal loop and used the observed line characteristics as a diagnostic of the magnetic field and other parameters of the coronal plasma.

In order to use the RATAN-600 radio telescope for the detection and investigation of fine structure in the frequency spectra of solar radio sources and reconstruction of the physical conditions in the emitting coronal plasma, a panoramic spectral analyzer with a frequency resolution up to 5% was developed and put into use at the Special Astrophysical Observatory. Using this equipment, a narrow-band line at 8.5 cm was detected in May 1996. A brief description of the results of the observations and a preliminary interpretation are given in [10]. In the present paper, we conduct a more detailed analysis of the observations and of models of the source line emission.

2. OBSERVATIONS

We conducted spectral polarization observations of the active region AR 7962 on May 10–20, 1996, on the RATAN-600 telescope using the southern sector of the main reflector, a periscopic mirror, and an asymmetric parabolic cylinder at the center of the system [11]. A receiving complex with a modern feed [12] covering wavelengths from 2 cm to 32 cm was placed at the focus. The radio-telescope antenna beam is determined by the dimensions of the periscope and is equal to

$$\begin{aligned} \theta_{\text{horizontal(arcsec)}} &= 0.85\lambda(\text{mm}), \\ \theta_{\text{vertical(arcmin)}} &= 0.75\lambda(\text{mm}). \end{aligned} \quad (1)$$

During the measurements, we used a panoramic spectral analyzer [13, 14] and recorded in the subintervals 18–12, 12–8, 8–5.5, 5.5–3.5, 3.5–2.5. 2.5–1.5, 1.2–0.9 GHz. Each of these intervals was subdivided using eight filters, with frequency resolution to 5%.

1063-7729/00/4404-0271$20.00 © 2000 MAIK "Nauka/Interperiodica"

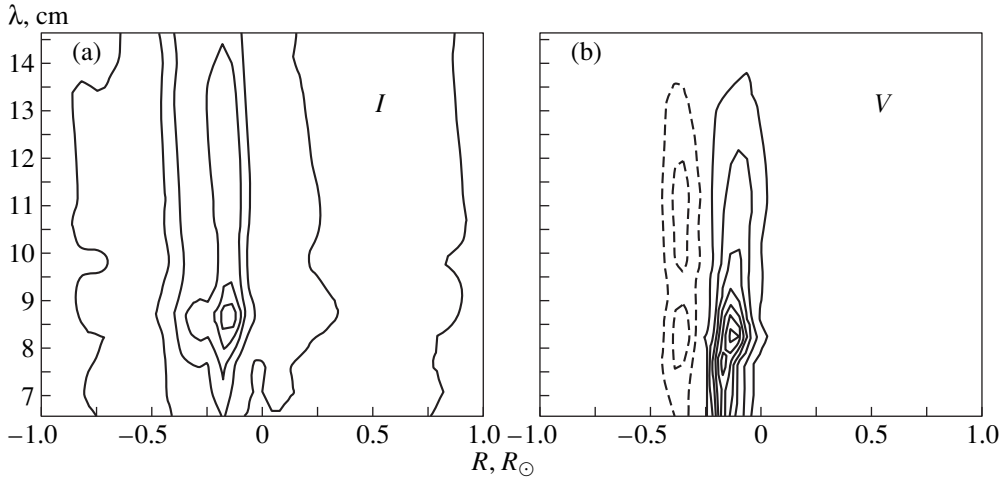

Fig. 1. Multifrequency, one-dimensional scan of the source AR 7962 recorded by RATAN-600 on May 12, 1996 (lines of equal intensity in the "distance R from the plane of the central meridian—wavelength λ" plane); (a) Stokes parameter I, (b) Stokes parameter V.

The radio source was associated with the complex sunspot group AR 7962, which was roughly at the center of the solar disk on May 11–12, 1996. Data from Mount Wilson Observatory indicate that this group consisted of a large bipolar formation with spot sizes ~3′ and a smaller bipolar formation toward the west with spot sizes ~1′. There were patches of southern magnetic field interspersed with northern magnetic field in the eastern part of AR 7962.

The radio source in this active region detected by RATAN-600 had a well-defined bipolar structure made up of two circularly polarized components. The sign of the polarization relative to the magnetic field at the photospheric level corresponds to an extraordinary wave. One distinguishing feature of the source was the presence of narrow-band line features superimposed on the characteristically smooth radio spectrum for the active region. The multifrequency, one-dimensional scan presented in Fig. 1a shows a concentration of lines with equal intensity I near 8.5 cm. The recording of the Stokes parameter V (Fig. 1b) indicates that this feature was present only in the western component of the bipolar source.

The fine line structure is clearly visible in Fig. 2, which presents the frequency dependence for the total flux of the entire group (Fig. 2a) and the fluxes for the two oppositely polarized components (Fig. 2b). The integrated intensity in the line exceeds the background by roughly 50%; the relative line width is 10–20%.

Comparison of the RATAN-600 observations and Nobeyama radio images at 1.7 cm for May 11–12, 1996 (Fig. 2c), shows that the line source coincides with a small, bright high-frequency source. The brightness temperature of this source, which was about 10″ in size, was approximately 20000 K over the two days indicated. The connection between this source and the 8.5 cm line source is also supported by observations on May 13–14 (Fig. 2): The line disappeared from the RATAN-600 spectra (and the spectrum itself changed its shape), while the Nobeyama point source was transformed into an extended, diffuse region with a brightness temperature substantially lower than that on May 11–12. This all suggests that there was a compact source in this active region that contained dense, hot plasma and gave rise to the observed properties of the radio source.

Comparison of our radio measurements and a magnetic-field map shows that the coordinates of the RATAN-600 and Nobeyama source coincide with a line separating regions of different magnetic polarity. Analysis of YOHKOH soft X-ray solar images shows that AR 7962 contained a rich loop structure over the entire observation period of May 10–20, 1996. However, we were not able to identify the bright radio point source with any small-scale features visible at soft X-ray wavelengths. In addition, the loop structure did not display any drastic time variations during the period when the point source ceased to exist.

The RATAN-600 data do not allow us to reliably estimate the source dimensions. However, the identification of the 8.5-cm line source and the 1.7-cm source visible in the high-resolution Nobeyama images suggests that the line source is also roughly 10″ in size. In this case, we can estimate to an order of magnitude the brightness temperature for the emission near 8.5 cm. Assuming that the line flux is made up of two components—a bright, small source (10″ in size, in agreement with the Nobeyama measurements) and a weaker extended source (having a size of the order of 80″), due to background emission with a brightness temperature of the order of 10^6 K—we obtain a maximum brightness temperature in the line of $T_b \sim 10^7$ K, with a relative line width of about 20% and a degree of polarization of the order of 10%.

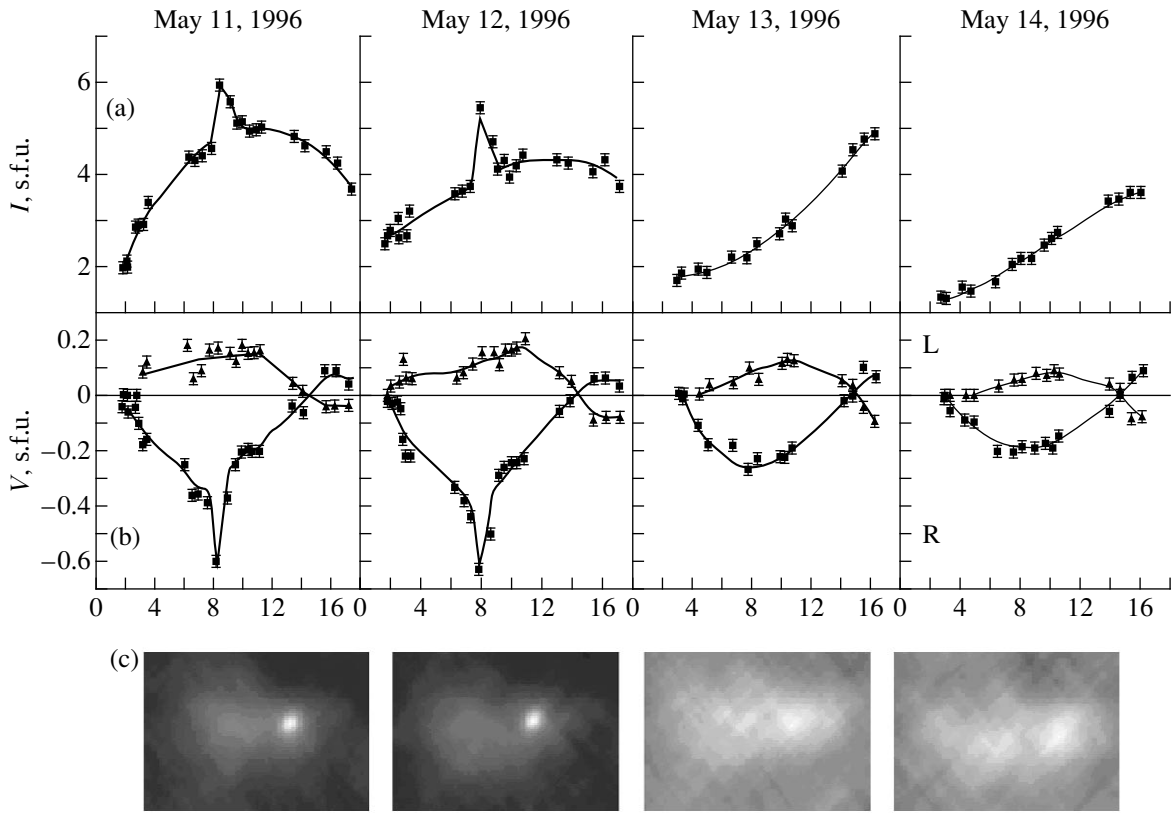

Fig. 2. Dependence of the (a) total flux of the entire source and (b) the fluxes of the two oppositely polarized components of the group on wavelength, derived from the RATAN-600 data and (c) from the Nobeyama radio maps at 1.7 cm on May 11–14, 1996. I and V are expressed in solar flux units (1 s.f.u. = 10^{-26} W m^{-2} Hz^{-1}).

3. MODEL FOR THE SOURCE AND EMISSION MECHANISM

A desirable model for the source and emission mechanism should simultaneously explain the sources detected by both the RATAN-600 and Nobeyama telescopes. Since the source existed over a fairly extended period (more than two days), it is reasonable to suppose that the emission was thermal and was not the result of nonthermal or coherent mechanisms. This means that the contrast between the compact source and the background emission for the entire active region is due to the specific values of the kinetic temperature, electron density, and magnetic field and their distributions. We assume that, somewhere inside a coronal loop, there was a small region containing hot, dense plasma. The maximum brightness temperature $T_b \sim 10^7$ K implies allowed values for the kinetic temperature in the line source of that same order of magnitude, while the temperature of the surrounding plasma is likely to be somewhat lower. With regard to the electron density and magnetic field, we consider two possible origins for the observed radiation: (1) The narrow-band feature at 8.5 cm is due to cyclotron radiation, while the Nobeyama source emission is bremsstrahlung, and (2) the sources at both frequencies are due to bremsstrahlung. Our analysis shows that the former scheme can better explain the fine structure of the spectrum in AR 7962 on May 11–12, 1996.

3.1. A Cyclotron Origin for the Line

Let us suppose that, at the height of the compact source, the magnetic field B is sufficiently strong that the frequency f corresponding to a wavelength of 8.5 cm could be a low harmonic of the electron gyrofrequency, $f = sf_B = seB/2\pi mc$ (e and m are the charge and mass of the electron, c is the speed of light, and s is the number of the harmonic). When analyzing various magnetic-field configurations in which cyclotron lines could form, we should allow for the fact that the width of a cyclotron line is determined by the Doppler effect and/or inhomogeneity in the magnetic field [1, 2]. If the line source is a neutral current or a magnetic field containing a maximum at some frequency, the line width is determined by Doppler broadening, and will not exceed $\Delta\lambda/\sqrt{\lambda} \sim 2\sqrt{2}\,\beta_T\cos\alpha$ [where $\beta_T = (kT/mc^2)^{1/2}$, T is the kinetic temperature of the plasma, k is the Boltzmann constant, and α is the angle between the magnetic field and line of sight]. Below, we take into account both effects broadening the cyclotron line and will consider the formation of the observed line in a source with uni-

form magnetic field, analogous to the treatment in [8, 9] used to interpret the observations of Wilson [6].

In addition, given the important observational fact that there is only one line in the spectrum (and not a series of lines at multiple frequencies), we can conclude with certainty that the line emission must occur only at the frequency corresponding to the third harmonic of the gyrofrequency ($s = 3$). This follows from the widely known properties of gyroresonance layers under the conditions typical for coronal plasma: Harmonics with numbers $s \geq 4$ are optically thin, while layers with $s = 2$, 3 are optically thick, for variations of the coronal parameters within reasonable limits. Consequently, if the observed line were due to the second-harmonic emission from a hot source, the emission would be absorbed in the $s = 3$ layer, located in the weaker magnetic field higher up, in the main part of the corona. Further, if the hot source corresponded to the $s = 4$ harmonic at 8.5 cm, it would be impossible to explain the absence of line emission at 11.3 cm, corresponding to the third harmonic of the gyrofrequency, since the optical depth of the $s = 3$ layer substantially exceeds that of the $s = 4$ layer. Therefore, if the hot source had a significant emission at the fourth harmonic, there should have also been a line with $s = 3$ at 11.3 cm. Thus, the observed line emission must be due to the third harmonic of the gyrofrequency, and we can estimate the magnetic field in the source:

$$B = \frac{2\pi mc^2}{3e\lambda} \sim 400 \text{ G}. \quad (2)$$

According to *Solar Geophysical Data*, the magnetic field in this spot group at the photospheric level was $B_{\text{ph}} \simeq 2000$ G, and the size of the main spot was $d \sim 10^9$ cm. If we assume that the magnetic field can be approximated by a vertical dipole immersed below the photosphere at a depth equal to the spot radius, we can use (2) to estimate the height at which the compact source is located: $h \sim 8 \times 10^8$ cm. The observed line width is determined by inhomogeneities in the magnetic field along the line of sight. In the same approximation, we can estimate the geometrically thick source as follows:

$$\frac{\Delta h}{h + d} = \frac{1}{3}\frac{\Delta\lambda}{\lambda} \simeq 0.07 \quad (3)$$

or $\Delta h \sim 10^8$ cm, in agreement with data on the thickness of coronal loops. Note that this exceeds the geometrical thickness of the gyroresonance layer $L_3 \simeq 2\sqrt{2}\beta_T \cos\alpha L_B \sim 3 \times 10^7$ cm (for $T \sim 10^7$ K and $L_B \sim 10^9$ cm), confirming the importance of the Doppler effect in the formation of the line profile.

To estimate the optical depth of the gyroresonance layer in the line source, we must know the angle α between the magnetic field and the line of sight. The weak polarization of the observed radio emission requires rather large optical depths τ_{3_o} and τ_{3_x} for the $s = 3$ layer, for both ordinary and extraordinary waves. This imposes some restriction on the angle α: The waves must propagate at a fairly large angle to the magnetic field; otherwise, the $s = 3$ layer would be transparent for the ordinary mode, which would lead to substantial polarization of the emission. However, in a hot source with the parameters indicated above, $\tau_{3_{o,x}} > 1$ is easily satisfied for a wide range of angles α. Below, we adopt the value $\alpha \sim 45°$ for our estimations.

The next step in our qualitative modeling is finding the electron density and dimensions of the source. In a hot plasma ($T \sim 10^7$ K), the condition $\tau_{3_{o,x}} > 1$ is satisfied even for usual coronal densities N_e and typical scales for variation of the magnetic field L_B. There is an upper limit to the number density imposed by the absence of the fourth harmonic in the observed spectrum (which would be at 6.4 cm). A lower limit is imposed by the necessity to provide a sufficiently high level of bremsstrahlung at 1.7 cm.

We will begin with the observed size of the Nobeyama source, $l \simeq 7 \times 10^8$ cm (which corresponds to an angular size of 10″) and find the electron density that would provide the observed brightness at 1.7 cm. Assuming that the source is spherically symmetric, its size along the line of sight is equal to the observed transverse size, $l \sim 7 \times 10^8$ cm. We can estimate the optical depth of the radiating layer using the known formulas for bremsstrahlung (see, for example, [15–17]):

$$\tau_b \sim 10^{-4}\frac{N_e^2\lambda^2 l}{T^{3/2}}. \quad (4)$$

Here and in all following formulas, N_e is expressed in units of 10^9 cm^{-3}, T in units of 10^6 K, l in units of 10^8 cm, and λ in cm. For a temperature $T \sim 10^7$ K, the measured values for the brightness temperature at 1.7 cm imply that the required optical depth is

$$\tau_b \simeq 2 \times 10^{-3}. \quad (5)$$

Assuming that the source size along the line of sight is equal to the observed size, $l \sim 7 \times 10^8$ cm, we find that (5) is fulfilled for an electron density $N_e \sim 6 \times 10^9$ cm^{-3}.

At a temperature of $T \sim 10^7$ K, electron density $N_e \sim 6 \times 10^9$ cm^{-3}, and characteristic magnetic-field scale $L_B \sim 10^9$ cm, the optical depth in the third harmonic is rather large. Using the known relations for the optical depth of a gyroresonance layer in a quasi-dipole approximation [15–16]

$$\tau_{3_{o,x}} \simeq 0.04 N_e T^2 \lambda L_B \frac{\sin^4\alpha}{\cos\alpha}(1 \mp \cos\alpha)^2, \quad (6)$$

we obtain $\tau_{3_o} \sim 60$ and $\tau_{3_e} \sim 2 \times 10^3$ for $\alpha = 45°$ for the ordinary and extraordinary waves, respectively. How-

ever, the emission at the $s = 4$ harmonic is not negligibly small in such a source; according to the relation

$$\tau_{4_{o,x}} \simeq 0.7 \times 10^{-4} N_e T^3 \lambda L_B \frac{\sin^6\alpha}{\cos\alpha}(1 \mp \cos\alpha)^2, \quad (7)$$

the optical depths to the extraordinary and ordinary waves are $\tau_{4_e} \sim 8$ and $\tau_{4_o} \sim 0.3$, respectively. This means that the radio spectrum of a source with these parameters should have a polarized line at 6.4 cm, in contradiction with the observations. Consequently, the parameters of the compact source must be such that they suppress the radiation at the fourth harmonic.

However, we cannot vary these parameters arbitrarily: The kinetic temperature cannot be lower than the observed brightness temperature, and the electron density must also be appreciably lowered (otherwise, it would not be possible to explain the Nobeyama data). The optical depth $\tau_{4_{o,x}}$ (7) can be reduced via two free parameters—the scale for magnetic-field variations L_B and the angle α. In our estimations above, we assumed that the magnetic field in the coronal loop (and in the compact source) does not differ from the dipole field in the surrounding atmosphere above the spot. We adopted this assumption to obtain a first crude estimate, but it is unlikely that it adequately describes the magnetic field of the complex spot group, especially since the region studied contains a rich loop structure. Bearing in mind the necessity of suppressing the fourth harmonic, it could be that the characteristic scale for magnetic-field variations in the coronal loop is appreciably smaller than the value we adopted above, $L_B \sim 10^9$.

It is possible that the overall magnetic field consists of two components: a longitudinal component (along the loop axis), associated with the feet of the loop in the photosphere, and an azimuthal component, due to the current along the loop. In this case, the field scale variations could coincide (or be smaller than) the transverse size of the loop. If $L_B \sim 10^8$ cm, we find that $\tau_{4_e} \simeq 1$ and $\tau_{4_o} \ll 1$. Here, we must allow for the fact that values of the optical depth obtained using the formulas presented above will be somewhat overestimated. Relations (6) and (7) are valid when the kinetic temperature and electron density vary only slightly within the region in the gyroresonance layer where the emission coefficient for magnetobremsstrahlung is not exponentially small. Under typical conditions for radio sources in active regions, where the parameters vary fairly smoothly, this condition is satisfied with a large margin. However, in coronal loops, when the gradients for parameter variations can be rather large, the geometrical thickness of the gyroresonance layer can be comparable to the scales for variations in the kinetic temperature and electron density along the line of sight (for example, when $L_B \sim 10^9$ cm, the size of the gyroresonance layer, $L_s \sim 2\sqrt{2}\, L_B \beta_T \sim 8 \times 10^7$ cm, is comparable with the thickness of the loop). If we take into account the inhomogeneity of the parameter distributions in the layer and integrate to obtain a more accurate description of the optical depth (as is done, for example, in [3, 18]), the resulting values τ_s are somewhat lower than those derived using (6) and (7). As before, the $s = 3$ layer remains optically thick, but the fourth harmonic at 6.4 cm can be optically thin and indistinguishable against the background emission of the entire active region.

At first glance, another means to choose parameters satisfying the requirements of the observations is to select a suitable angle α. We can see from (6) and (7) the well-known effect of the "transparency" of gyroresonance layers along the magnetic field ($\tau_s \longrightarrow 0$ when $\alpha \longrightarrow 0$): At reasonably small values of the angle α, it is possible to simultaneously satisfy both inequalities required to suppress the fourth-harmonic emission and to preserve sufficient optical depth of the $s = 3$ layer to ordinary waves, $\tau_{3_o} > 1$ and $\tau_{4_e} < 1$ (precisely this combination is required to provide a single, weakly polarized line in the spectrum corresponding to the third harmonic). However, the ratio of the corresponding optical depths

$$\frac{\tau_{4_e}}{\tau_{3_0}} \simeq 2.5 T \sin^2\alpha \frac{(1 + \cos\alpha)^2}{(1 - \cos\alpha)^2} \quad (8)$$

increases as the angle α decreases (recall that the temperature in (8) is in units of 10^6 K). In particular, this ratio exceeds unity at a temperature of $T \sim 10^7$ K and angles $\alpha \leq 30°$; i.e., when the fourth harmonic is suppressed to the background level, the ordinary emission of the third harmonic is also appreciably reduced. This means that attempts to explain the observed spectrum by varying the angle between the magnetic field and the direction of propagation of the radiation cannot yield the desired results. Note that the very existence of a line with virtually constant parameters over two days of observations, during which the observation angle varied by 15°, indicates that the propagation conditions do not play the defining role in forming the spectral features.

Thus, our analysis suggests that the line structure detected on the RATAN-600 telescope at 8.5 cm and the bright point source visible on the 1.7-cm Nobeyama map can be explained as a thermal emission from a compact source, probably located in a coronal loop. The kinetic temperature and electron density in this source are enhanced compared to the surrounding loop plasma. In this picture, the line observed at 8.5 cm has a cyclotron origin and corresponds to radiation at the third harmonic of the electron gyrofrequency. The high-frequency emission at 1.7 cm from the same source is due to bremsstrahlung.

3.2. A Bremsstrahlung Origin for the Line

Fine structure in the form of a line could also form via bremsstrahlung, in the case of certain specific distributions of the electron density and kinetic tempera-

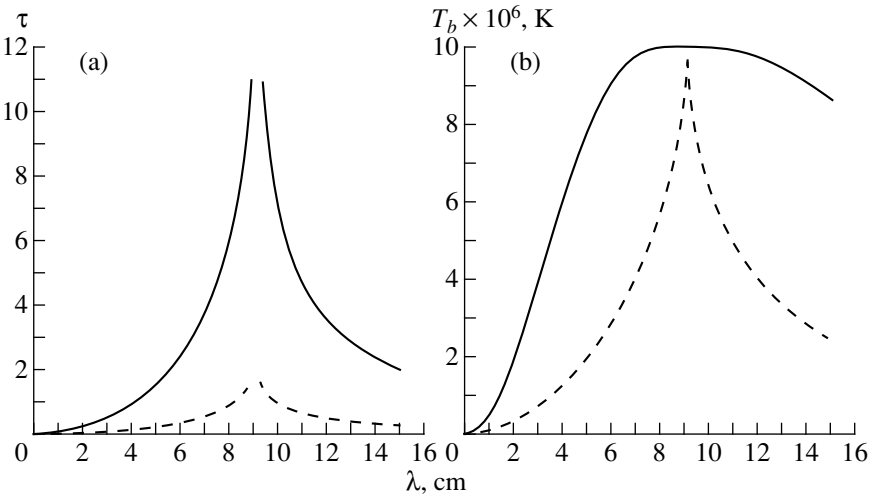

Fig. 3. Dependence of the (a) optical depth and (b) brightness temperature of bremsstrahlung from a plasma layer with temperature $T = 10^7$ K, maximum electron density $N_0 = 1.5 \times 10^{11}$ cm^{-3}, and geometrical depth $l = 7 \times 10^8$ cm (solid curve) and $l = 10^8$ cm (dashed curve).

ture along the line of sight [3, 8, 19]. For the values of N_e and T adopted above, the bremsstrahlung from a layer with thickness $l \sim 10^8$–10^9 cm will be negligibly small compared to cyclotron radiation at 8.5 cm. However, if the plasma density is appreciably higher than the indicated values or the magnetic field in the source is not sufficiently strong to give rise to radiation at low gyrofrequency harmonics, bremsstrahlung could play a more substantial role.

There can be a maximum in the bremsstrahlung spectrum from an inhomogeneous layer if the electron density along the line of sight reaches a maximum N_0 at some point; the maximum appears at wavelength $\lambda_p = c/f_p$, corresponding to the plasma frequency $f_p = \sqrt{e^2 N_0/\pi m}$. The optical depth of an isothermal uniform layer with temperature T, geometrical thickness l, and electron density that varies with height as $N_e = N_0 \cosh^{-2}[(h - h_0)/l]$ (h_0 is the height of the source in the corona) can be described by the formula

$$\tau_b = 1.6 \times 10^{-5} \frac{N_0^2 l \lambda^2}{T^{3/2}} f(\nu_0), \qquad (9)$$

where

$$\nu_0 = \frac{\lambda^2}{\lambda_p^2}, \quad f(\nu_0) = \frac{1+\nu_0}{4\nu_0^{3/2}} \ln\frac{1+\sqrt{\nu_0}}{1-\sqrt{\nu_0}} - \frac{1}{2\nu_0}. \qquad (10)$$

When $\nu_0 \ll 1$, the function $f(\nu_0) \simeq 2/3$. When $\nu_0 \gg 1$, the function $f(\nu_0)$ falls off as $2/(3\nu_0^2)$. When $\nu_0 \simeq 1$, $f(\nu_0)$ grows without limit as ν_0 approaches unity. A rough estimate of the maximum absorption at wavelengths $\lambda \sim \lambda_p$ can be derived from the exact solution of the problem of the passage of a wave through a parabolic plasma layer [20]. Such an estimate is presented by Zhelenyakov and Zlotnik [17],

$$f_{\max}(\nu_0 \simeq 1) \simeq \frac{1}{2} \ln\frac{8\pi^2 l}{\lambda} - \frac{1}{2}, \qquad (11)$$

which is $f_{\max} \sim 10$ for $\lambda \sim 8.5$ cm and $l \sim 7 \times 10^8$ cm. Taking into account this restriction and substituting the values $N_0 \simeq 1.5 \times 10^{11}$ cm^{-3} (chosen so that the maximum of the spectrum will be at 8.5 cm), $T \sim 10^7$ K, and $l \sim 7 \times 10^8$ cm (which follow from the RATAN-600 observations) into τ_b, we obtain the frequency dependence for the optical depth and the brightness temperature depicted by the solid curves in Fig. 3. It is obvious that the emission expected for a region with these parameters does not agree with the observations: The optical depth of the layer is too large at centimeter wavelengths. The formation of a bremsstrahlung line spectrum requires that the maximum optical depth be less than or of the order of unity. The dashed curve in Fig. 3 illustrates the corresponding relations for a smaller layer thickness $l \sim 10^8$ cm and can, in principle, be brought into agreement with the RATAN-600 data.

However, the optical depth and brightness temperature of this same source at 1.7 cm are (for $\nu_0 = 0.04 \ll 1$, $f(0.04) \approx 2/3$) $\tau_b \sim 0.02$ and $T_b \sim 2 \times 10^5$ K, an order of magnitude larger than the values recorded at Nobeyama. If we decrease the extent of the source along the line of sight to an implausibly small size $l \sim 10^7$ cm, we can obtain the 1.7-cm values $\tau_b \sim 2 \times 10^{-3}$ and $T_b \sim 2 \times 10^4$ K, close to those observed at Nobeyama. However, in this case, the maximum optical depth at 8.5 cm will be less than unity, so that the brightness temperature is lower than the kinetic temperature and is much lower than that observed on RATAN-600. Note also that the shape of the bremsstrahlung line is a "cusp" with a sharp maximum, which is also not in agreement with the observa-

tions: The expected brightness temperature in an optically thin bremsstrahlung line decreases by a factor of three at a relative distance from the line center of 0.01, while the actual relative line half-width is 0.1.

Thus, the line observed on RATAN-600 and shorter wavelength source detected at Nobeyama cannot be simultaneously explained as a result of bremsstrahlung from a single region.

4. CONCLUSION

We have shown that the RATAN-600 radio telescope detected a line in the radio spectrum of an active region. The RATAN-600 archives contain many other recordings with narrow-band features in the spectra of local sources. These data are currently being checked to exclude the influence of calibration effects in different frequency channels. We consider the data presented here to be trustworthy, first, because of the comparatively high contrast of the line relative to the background and second, because of the simultaneous detection of a bright point source in the Nobeyama image. The positions of the two sources on the disk coincide, and they ceased to exist at the same time.

Our analysis indicates that the observed line near 8.5 cm can be explained as cyclotron radiation at the third harmonic of the electron gyrofrequency from a dense, hot, small source in a coronal loop, while the emission at 1.7 cm from this same source is due to bremsstrahlung. The observed parameters can be used to estimate the physical conditions in the compact source: magnetic field $B \simeq 400$ G, kinetic temperature $T \simeq 10^7$ K, electron density $N_e \simeq 6 \times 10^9$ cm^{-3}, transverse size of the loop $l \sim 10^8$, and characteristic scale for magnetic-field variations $L_B \sim 10^8$ cm. Our study indicates that the observed line cannot be the result of bremsstrahlung.

It is important to note that, in the present paper, we have not considered the mechanism responsible for the background emission; interpretation of the frequency spectrum and polarization of the emission of the entire active region AR 7962 on May 10–12, 1996, at 2–32 cm is discussed in another paper. However, since the line source is expected to be in the corona, higher than the background source, and is optically thick, the specific mechanism for the background emission is not important for interpretation of the line emission.

ACKNOWLEDGMENTS

This work was supported by the Russian Foundation for Basic Research (project codes 98-02-16238 and 99-02-16403). The authors thank the Nobeyama Radio Observatory for the possibility of using their 1.7-cm solar maps, obtained via the Internet.

REFERENCES

1. V. V. Zheleznyakov and E. Ya. Zlotnik, Astron. Zh. **57**, 778 (1980).
2. V. V. Zheleznyakov and E. Ya. Zlotnik, *IAU Symp. 86: Radio Physics of the Sun*, Ed. by M. Kundu and T. Gergely (Reidel, Dordrecht, 1980), p. 87.
3. V. V. Zheleznyakov and Yu. V. Tikhomirov, Solar Phys. **81**, 121 (1982).
4. R. F. Wilson, Solar Phys. **89**, 103 (1983).
5. E. J. Schmahl, R. K. Shevgaonkar, M. R. Kundu, *et al.*, Solar Phys. **93**, 305 (1984).
6. R. F. Wilson, Astrophys. J. **298**, 911 (1985).
7. K. R. Lang, R. F. Wilson, K. L. Smith, *et al.*, Astrophys. J. **322**, 1044 (1987).
8. V. V. Zheleznyakov and E. Ya. Zlotnik, Pis'ma Astron. Zh. **14**, 461 (1988).
9. V. V. Zheleznyakov and E. Ya. Zlotnik, Solar Phys. **121**, 449 (1989).
10. V. M. Bogod, V. I. Garaimov, V. V. Zheleznyakov, *et al.*, *Proc. of 1998 Nobeyama Symp.*, NRO Report (1999).
11. D. V. Korol'kov and Yu. N. Parijskiĭ, Sky Telesc. **57**, 4 (1979).
12. V. N. Dikiĭ, *IEEE Asia–Pacific Workshop on Mobile Telecommunication* (Hyon Son, Korea Institute of Communication Sciences, Kyongju, 1995), p. 173.
13. V. M. Bogod, S. M. Vatrushin, V. E. Abramov-Maximov, *et al.*, ASP Conf. Ser. **46**, 306 (1993).
14. K. R. Lang, R. F. Willson, J. N. Kile, *et al.*, Astrophys. J. **419**, 398 (1993).
15. V. V. Zheleznyakov, *Radio Emission of the Sun and Planets* (Nauka, Moscow, 1964).
16. E. Ya. Zlotnik, Astron. Zh. **45**, 310, 585 (1968).
17. V. V. Zheleznyakov and E. Ya. Zlotnik, Astron. Zh. **57**, 1038 (1980).
18. V. V. Zheleznyakov and E. Ya. Zlotnik, Solar Phys. **68**, 317 (1980).
19. S. I. Syrovatskiĭ and V. D. Kuznetsov, *IAU Symp. 86: Radio Physics of the Sun*, Ed. by M. Kundu and T. Gergely (Reidel, Dordrecht, 1980), p. 445.
20. V. L. Ginzburg, *The Propagation of Electromagnetic Waves in Plasma* (Nauka, Moscow, 1967).

Translated by D. Gabuzda